# Isotropic Sources and Attenuation Structure: Nuclear Tests, Mine Collapses, and *Q*

by

Sean Ricardo Ford

B.A. (University of California, Berkeley) 1999
M.S. (Arizona State University) 2005

A dissertation submitted in partial satisfaction of the

requirements for the degree of

Doctor of Philosophy

in

Earth and Planetary Science

in the

Graduate Division

of the

University of California, Berkeley

Committee in charge:

Professor Douglas Dreger, Chair
Professor Barbara Romanowicz
Professor David Brillinger

Fall 2008

The dissertation of Sean Ricardo Ford is approved:

Chair _____ Date _____

_____ Date _____

_____ Date _____

University of California, Berkeley

Fall 2008

Isotropic Sources and Attenuation Structure:
Nuclear Tests, Mine Collapses, and *Q*



by Sean Ricardo Ford

Abstract

Isotropic Sources and Attenuation Structure:
Nuclear Tests, Mine Collapses, and *Q*

by

Sean Ricardo Ford

Doctor of Philosophy in Geophysics

University of California, Berkeley

Professor Douglas Dreger, Chair

This dissertation investigates two different, but related, topics: isotropic sources and attenuation structure. The first section reports the analysis of explosions, earthquakes, and collapses in the western US using a regional time-domain full waveform inversion for the complete moment tensor. The events separate into specific populations according to their deviation from a pure double-couple and ratio of isotropic to deviatoric energy. We find that in the band of interest (0.02-0.10 Hz) the source-type is insensitive to small velocity model perturbations and several kilometers of incorrect depth when the signal-to-noise ratio (SNR) is greater than 5. However, error in the isotropic moment grows from 50% to 200% as the source depth decreases from 1 km to 200 m. We add an analysis of the Crandall Canyon Mine collapse that occurred on 6 August 2007 in Utah to our dataset. The results show that most of the recorded seismic wave energy is consistent with an underground collapse in the mine. We contrast the waveforms and moment tensor results of the Crandall Canyon Mine seismic event to a similar sized tectonic earthquake about 200 km away near Tremonton, Utah, that occurred on September 1, 2007 demonstrating the low

frequency regional waveforms carry sufficient information to distinguish the source-type. Finally, confidence in the regional full moment tensor inversion solution is described via the introduction of the network sensitivity solution (NSS), which takes into account the unique station distribution, frequency band, and signal-to-noise ratio of a given event scenario. The method is tested for the well-recorded nuclear test, JUNCTION, at the Nevada Test Site and the October 2006 North Korea test, where the station coverage is poor and the event magnitude is small. Both events contain large isotropic components that are 60% of the total moment, though the NTS event is much better constrained than the North Korea test. The network solutions illustrate the effect of station coverage on the ability to recover the seismic moment tensor, and to distinguish events of different source types, Importantly, the network solutions may also be used in synthetic cases to evaluate where stations are needed in order to improve moment tensor based source type identification.

The attenuation (parameterized as $Q$) structure section begins with an analysis of five one-dimensional (1-D) attenuation measurement methods methodologies to a Northern California dataset. The methods are: (1) coda normalization (CN), (2) two-station (TS), (3) reverse two-station (RTS), (4) source-pair/receiver-pair (SPRP), and (5) coda-source normalization (CS). The methods are used to measure $Q$ of the regional phase, Lg ($Q_{Lg}$), and its power-law dependence on frequency of the form $Q_0 f^{\eta}$. All methods return similar power-law parameters, though the range of the joint 95% confidence regions is large ($Q_0 = 85 \pm 40$; $\eta = 0.65 \pm 0.35$). The RTS and TS methods differ the most from the other methods and from each other. We also test the sensitivity of each method to changes in geometrical spreading, Lg frequency

bandwidth, the distance range of data, and the Lg measurement window. For a given method, there are significant differences in the power-law parameters, $Q_0$ and $\eta$. We conclude that when presenting results for a given method we suggest calculating $Q_0 f^{\eta}$ for multiple parameterizations using some a priori distribution. The analysis is extended for lateral variation in crustal attenuation of California by inverting 25,330 synthetic Wood-Anderson amplitudes from the California Integrated Seismic Network (CISN) for site, source, and path effects. *Q* ranges from 66 to 1000 (high to low attenuation) with an average of 143. The average *Q* is consistent with an amplitude decay function ($\log A_0$) for California when combined with a simple geometrical spreading rate. Attenuation in California is consistent with the tectonic structure of California, with low attenuation in the Sierra batholith and high attenuation at The Geysers, at Long Valley, and in the Salton Trough possibly due to geothermal effects. Finally, we perform inversions for regional attenuation of the crustal phase in the Yellow Sea / Korean Peninsula (YSKP) using a new method that attempts to solve the path/source amplitude trade-off by correcting the Lg spectral amplitude for the source using the stable, coda-derived source spectra. We compare the site, source and path terms produced to traditional methods and find good agreement. Regions of low *Q* correlate well with increased sediment thickness in the basins, particularly Bohai Basin located in the northern Yellow Sea. Regions of increased *Q* occur along topographic highs in the YSKP.

To my wife.

## Table of Contents

# Acknowledgments

This dissertation would not have been possible without the aid and guidance of my advisor Douglas Dreger and supervisor at Lawrence Livermore National Laboratory (LLNL), Bill Walter. Their knowledge of observational seismology is without limit, and I am fortunate to call them advisor, mentor, and friend. Thanks to the staff of the Berkeley Seismological Laboratory (BSL), especially Peggy Hellweg, Bob Uhrhammer, Kevin Mayeda, Pete Lombard, Doug Neuhauser, and Charley Paffenberger. As well as students and post-docs of the BSL including Fabio Cammarano, Vedran Lekic, Ahyi Kim, Junkee Rhie, and Aurelie Guilhem. Their technical, educational, and emotional support made this work fun and problem-free. More thanks to the seismology group at LLNL, especially Mike Pasyanos, Rengin Gok, Nathan Simmons, Steve Myers, Eric Matzel, Artie Rodgers, Megan Flanagan, Terri Hauk, and Flori Ryall. And even more thanks to Scott Phillips at Los Alamos National Laboratory. I also thank David Brillinger for being a member of my dissertation committee and for reading the manuscripts. Finally, I thank George Brimhall for an enlightening semester as his GSI and for being a member of my exam committee.

Part of this work was performed under the auspices of the Lawrence Scholar Program and the U.S. Department of Energy by Lawrence Livermore National Laboratory under Contract DE-AC52-07NA27344 as well as by the National Nuclear Security Administration under Contracts DE-FC52-06NA27324 and DE-FC52-06NA26605. I am also grateful for the Louderback Award.

# Chapter 1

## Introduction

This dissertation investigates two different, but related, topics: isotropic sources and attenuation structure. In this chapter I specifically introduce the results of each chapter. A more general introduction and review for each topic can be found at the beginning of each chapter.

The isotropic sources section begins in the second chapter where we calculate the deviatoric and isotropic source components for 17 explosions at the Nevada Test Site, as well as 12 earthquakes and 3 collapses in the surrounding region of the western US, using a regional time-domain full waveform inversion for the complete moment tensor. The events separate into specific populations according to their deviation from a pure double-couple and ratio of isotropic to deviatoric energy. The separation allows for anomalous event identification and discrimination between explosions, earthquakes, and collapses. Confidence regions of the model parameters are estimated from the data misfit by assuming normally distributed parameter values. We investigate the sensitivity of the resolved parameters of an explosion to imperfect Earth models, inaccurate event depths, and data with low signal-to-noise ratio (SNR) assuming a reasonable azimuthal distribution of stations. In the band of interest (0.02-0.10 Hz) the source-type calculated from complete moment tensor inversion is insensitive to velocity models perturbations that cause less than a half-cycle shift (<5 sec) in arrival time error if shifting of the waveforms is allowed. The explosion

source-type is insensitive to an incorrect depth assumption (for a true depth of 1 km), and the goodness-of-fit of the inversion result cannot be used to resolve the true depth of the explosion. Noise degrades the explosive character of the result, and a good fit and accurate result are obtained when the signal-to-noise ratio (SNR) is greater than 5. We assess the depth and frequency dependence upon the resolved explosive moment. As the depth decreases from 1 km to 200 m, the isotropic moment is no longer accurately resolved and is in error between 50-200%. However, even at the most shallow depth the resultant moment tensor is dominated by the explosive component when the data have a good SNR.

In the third chapter, we perform a moment tensor analysis with complete, three-component seismic recordings from stations operated by the USGS, the University of Utah, and EarthScope for the 6 August 2007 event in central Utah. The epicenter is within the boundaries of the Crandall Canyon coal mine. The analysis method inverts the seismic records to retrieve the full seismic moment tensor, which allows for interpretation of both shearing (e.g., earthquakes) and volume-changing (e.g., explosions and collapses) seismic events. The results show that most of the recorded seismic wave energy is consistent with an underground collapse in the mine. We contrast the waveforms and moment tensor results of the Crandall Canyon Mine seismic event to a similar sized tectonic earthquake about 200 km away near Tremonton, Utah, that occurred on September 1, 2007. Our study does not address the actual cause of the mine collapse.

In the fourth chapter, confidence in the regional full moment tensor inversion solution is described via the introduction of the network sensitivity solution (NSS),

which takes into account the unique station distribution, frequency band, and signal-to-noise ratio of a given event scenario. The NSS compares both data from a model event (either an explosion or earthquake) or the actual data with several thousands sets of synthetic data from a uniform distribution of all possible sources. The comparison with a model event provides the theoretically best-constrained source-type region and with it one can determine whether further analysis with the data is warranted. The NSS that employs the actual data gives a direct comparison of all other source-types with the best-fit source. In this way, one can choose a threshold level of fit where the solution is comfortably constrained. The method is tested for the well-recorded nuclear test, JUNCTION, at the Nevada Test Site. Sources that fit comparably well to a model explosion recorded with no noise have a large volumetric component and are not described well by a double-couple (DC) source, though the shallow –CLVD / explosion trade-off is evident. The network sensitivity solution using the real data from JUNCTION is even more tightly constrained to an explosion since the data contains some energy that precludes fitting with any type of deviatoric source. We also calculate the NSS for the October 2006 North Korea test, where the station coverage is poor and the event magnitude is small, and compare it with a nearby earthquake. The earthquake is well-constrained as a DC by three stations within 600 km of the source. However, in order to theoretically constrain the explosion, a fourth station is required (BJT) that is 1100 km from the source and recorded relatively high amplitudes for an isotropic source. When using real data to produce the NSS, the best-fit model has a very large isotropic component (60%) indicative of an explosion, however a model with only a slightly worse fit to the data has an isotropic component

that is 20% of the total moment and considerable DC energy. We show that the explosive component is better constrained with the addition of just one more station. We also introduce another method to analyze error in the solution caused by the velocity model. A suite of suitable 1-D models obtained from a prior probabilistic study is used to produce hundreds of solutions. The best-fitting solutions cluster around the explosion source.

The attenuation structure section begins in the fifth chapter with an analysis of regional attenuation $Q^{-1}$, where we try to reconcile discrepancies between measurement methods that are due to differing parameterizations (e.g., geometrical spreading rates), employed datasets (e.g., choice of path lengths and sources), and the nature of the methodologies themselves (e.g., measurement in the frequency or time domain). Here we apply five different attenuation methodologies to a Northern California dataset. The methods are: (1) coda normalization (CN), (2) two-station (TS), (3) reverse two-station (RTS), (4) source-pair/receiver-pair (SPRP), and (5) coda-source normalization (CS). The methods are used to measure $Q$ of the regional phase, Lg ($Q_{\mathrm{Lg}}$), and its power-law dependence on frequency of the form $Q_0 f^{\eta}$ with controlled parameterization in the well-studied region of Northern California using a high-quality dataset from the Berkeley Digital Seismic Network. We investigate the difference in power-law $Q$ calculated among the methods by focusing on the San Francisco Bay Area, where knowledge of attenuation is an important part of seismic hazard mitigation. All methods return similar power-law parameters, though the range of the joint 95% confidence regions is large ($Q_0 = 85 \pm 40$; $\eta = 0.65 \pm 0.35$). The RTS and TS methods differ the most from the other methods and from each other. This may

be due to the removal of the site term in the RTS method, which is shown to be significant in the San Francisco Bay Area. In order to completely understand the range of power-law $Q$ in a region, we advise the use of several methods to calculate the model. We also test the sensitivity of each method to changes in geometrical spreading, Lg frequency bandwidth, the distance range of data, and the Lg measurement window. For a given method, there are significant differences in the power-law parameters, $Q_0$ and $\eta$, due to perturbations in the parameterization when evaluated using a conservative pairwise comparison. The CN method is affected most by changes in the distance range, which is most likely due to its fixed coda measurement window. Since the CS method is best used to calculate the total path attenuation, it is very sensitive to the geometrical spreading assumption. The TS method is most sensitive to the frequency bandwidth, which may be due to its incomplete extraction of the site term. The RTS method is insensitive to parameterization choice, whereas the SPRP method as implemented here in the time-domain for a single path has great error in the power-law model parameters and $\eta$ is strongly affected by changes in the method parameterization. When presenting results for a given method we suggest calculating $Q_0 f^{\eta}$ for multiple parameterizations using some a priori distribution.

In the sixth chapter, we extend the analysis to two dimensions and calculate lateral variation in crustal attenuation of California by inverting 25,330 synthetic Wood-Anderson amplitudes from the California Integrated Seismic Network (CISN) for site, source, and path effects. Two-dimensional attenuation (q or $1/Q$) is derived from the path term, which is calculated via an iterative least-squares inversion that

also solves for perturbations to the site and source terms. Source terms agree well with initial CISN $M_L$s and site terms agree well with a prior regression analysis. q ranges from low attenuation at 0.001 ($Q$ = 1000) to high attenuation at 0.015 ($Q$ = 66) with an average of 0.07 ($Q$ = 143). The average q is consistent with an amplitude decay function ($\log A_0$) for California when q is combined with a simple geometrical spreading rate. Attenuation in California is consistent with the tectonic structure of California, with low attenuation in the Sierra batholith and high attenuation at The Geysers, at Long Valley, and in the Salton Trough possibly due to geothermal effects. Also, path terms are an order of magnitude smaller than site and source terms, suggesting that they are not as important in correcting for $M_L$.

Finally in the seventh chapter we perform inversions for regional attenuation ($1/Q$) of the crustal phase Lg in the Yellow Sea / Korean Peninsula (YSKP) using the amplitude attenuation tomography method (Amp) of Phillips and Stead (2008), which solves for source, site, and path attenuation, as well as two new variants of this method. The first method (CS) is a tomographic implementation of the method of Walter et al. (2007), which attempts to solve the path/source amplitude trade-off by correcting the Lg spectral amplitude for the source using the stable, coda-derived source spectra produced via the method of Mayeda et al. (2003). The second method (SI), developed by Pasyanos et al. (2009), uses a physical relationship for the source described by Walter and Taylor (2001) to set the initial source amplitude and interpret the source term after inversion. We compare the site, source and path terms produced by each method and comment on $Q$ in the YSKP, which correlates well with tectonic and topographic features in the region. Magnitude (and therefore the CS event term)

correlates well with the event term of the Amp and SI methods, which as expected correlate well with one another except for an absolute shift. The site term of the Amp and CS methods correlate with each other except for an absolute shift that is related to the shift between the Amp and CS method event term. The SI site term is similar to the other methods, except for stations INCN and TJN. The location of these stations mark the greatest difference in the SI path term (and therefore *Q*) from the other methods as well, which demonstrates the site/path trade-off. Another region of path term difference between the CS and other methods is in a region of few crossing paths, where the CS method may perform more accurately since it is not as susceptible to the source/path trade-off. Regions of low *Q* correlate well with increased sediment thickness in the basins, particularly Bohai Basin. Regions of increased *Q* occur along topographic highs in the YSKP.

# Chapter 2

## Identifying isotropic events using a regional moment tensor inversion

Published as: Ford, S. R., D. S. Dreger, and W. R. Walter (2009), Identifying isotropic events using a regional moment tensor inversion, *J. Geophys. Res.*

### 2.1 Introduction

The full seismic moment tensor (2nd rank tensor, $M_{ij}$) is a general representation of any seismic point source in terms of force-couples (Gilbert, 1971), and is used in tectonic studies to describe the double-couple (DC) nature of shear-faulting. However, $M_{ij}$ is sufficiently general to represent non-DC seismic sources (for an outstanding review of non-DC earthquakes, see Julian et al., 1998). The isotropic component of the moment tensor ($M_{ij}^{\mathrm{ISO}} = \delta_{ij} (M_{11}+M_{22}+M_{33})/3$) is related to the volume change associated with a source (Müller, 1973), and is significant in the case of an explosion. The deviatoric component of $M_{ij}$ ($M_{ij}^{\mathrm{DEV}} = M_{ij} - \delta_{ij} (M_{11}+M_{22}+M_{33})/3$) is most often employed to define the DC source, but can also describe the volume-compensated linear vector dipole (CLVD), which has been used to explain deep seismicity (e.g., Knopoff and Randall, 1970; Kawakatsu, 1990), and has also been shown to result from complex faulting events (Kuge and Lay, 1994). Complex sources like a tensile crack require a combination of deviatoric and isotropic components, and the opening-crack has been suggested as a source for some volcanic events (e.g.,

Foulger et al., 2004; Templeton and Dreger, 2006) and the closing-crack for mine collapses (e.g. Pechmann et al., 1995; Bowers and Walter, 2002).

The inversion of seismic data to calculate the deviatoric moment tensor has been done for over 30 years in both the time-domain (e.g., Stump and Johnson, 1977) and frequency domain (e.g., Gilbert and Dziewonski, 1975). The inversion of full-waveform data from regional events is now routine practice at several institutions including the Berkeley Seismological Laboratory since 1993 (Romanowicz et al., 1993), where the results are housed at the Northern California Earthquake Data Center (NCEDC; www.ncedc.org/ncedc/mt.html). Recently, Minson and Dreger (2008) have extended the full-waveform inversion to calculate all six independent elements of the symmetric moment tensor, which allows for estimation of the isotropic component of the source.

The concept of using intermediate period waveforms, particularly surface wave radiation patterns, to identify explosions goes back more than 40 years. Early results were disappointing due to the presence of unexpected Love waves and occasional reversed Rayleigh waves from tectonic release (e.g. Press and Archambeau, 1962; Brune and Pommery, 1963). However despite these complexities, the well-established ratio of surface wave magnitude ($M_S$) to body wave magnitude ($m_b$) separates earthquakes from explosions even when there is significant tectonic release, indicating there are differences in the waveforms, even if the explosion signals do not always conform to the simple isotropic model. Identification of events with demonstrably significant isotropic components can aid in yield determination (e.g., Stevens and Murphy, 2001; Patton, 1991) and possibly nuclear test discrimination (e.g., Woods et

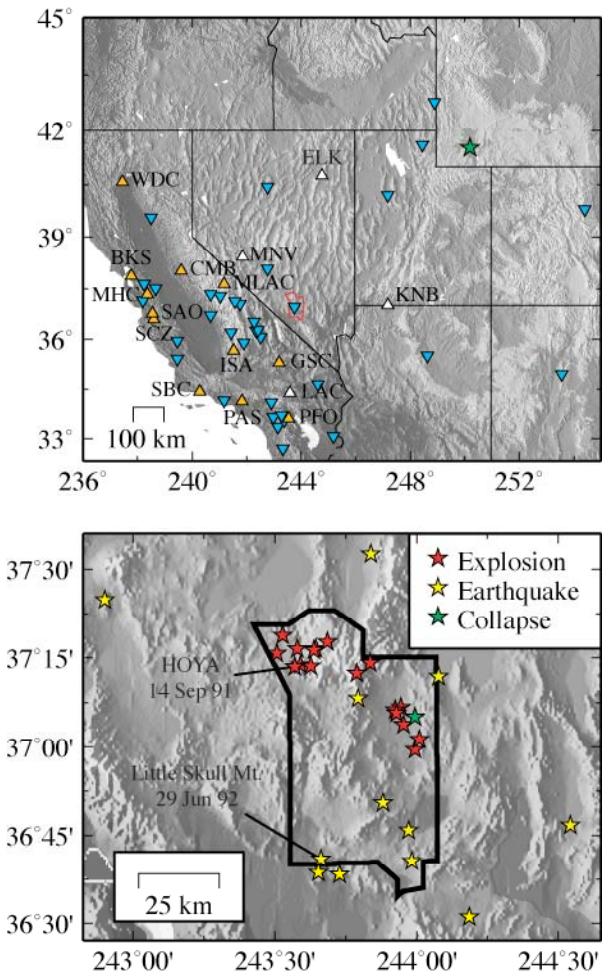


Figure 2.1 Map of the Western US with stations (blue inverted triangles), earthquakes (yellow stars), explosions (red stars), and collapses (green stars) used in this study. The bottom panel is a blow-up of the Nevada Test Site (NTS) region with the NTS outlined in black and in the top panel in red. The top panel also shows the LLNL network (white triangles) and stations used in the explosion analysis (orange triangles). The location of the HOYA test explosion (Figure 3) and Little Skull Mt. earthquake (Figure 2.2) are also given.

al., 1993). Given and Mellman (1986) inverted teleseismic long-period fundamental mode surface waves from 18 large ($m_b \geq 5.5$) nuclear test explosions at the Nevada Test Site (NTS) to calculate a three-parameter source model. The model was used to estimate the isotropic moment ($M_I$), along with the strike and moment of an assumed vertical strike-slip component, and they found no improvement in yield estimation

Table 2.1 Event list[1]

| Name[2] | Date[3] | Time[3] | Latitude[3] | Longitude[3] | Depth (m)[4] | Magnitude[6] |
|---|---|---|---|---|---|---|
| KERNVILLE[P] | 1988/02/15 | 18:10:00.09 | 37.314 | -116.472 | 542 | $5.30_L^{NCSN}$ |
| AMARILLO[P] | 1989/06/27 | 15:30:00.02 | 37.275 | -116.354 | 640 | $4.90_L^{NCSN}$ |
| DISKO ELM[R] | 1989/09/14 | 15:00:00.10 | 37.236 | -116.164 | 261 | $4.40_L^{NCSN}$ |
| HORNITOS[P] | 1989/10/31 | 15:30:00.09 | 37.263 | -116.492 | 564 | $5.40_L^{NCSN}$ |
| BARNWELL[P] | 1989/12/08 | 15:00:00.09 | 37.231 | -116.410 | 601 | $5.30_L^{NCSN}$ |
| METROPOLIS[Y] | 1990/03/10 | 16:00:00.08 | 37.112 | -116.056 | 469 | $4.94_d^{NCSN}$ |
| BULLION[P] | 1990/06/13 | 16:00:00.09 | 37.262 | -116.421 | 674 | $5.34_d^{NCSN}$ |
| AUSTIN[Y] | 1990/06/21 | 18:15:00.00 | 36.993 | -116.005 | 350 | $4.11_d^{NCSN}$ |
| HOUSTON[N] | 1990/11/14 | 19:17:00.07 | 37.227 | -116.372 | 594 | $4.86_d^{NCSN}$ |
| COSO[Y] | 1991/03/08 | 21:02:45.08 | 37.104 | -116.075 | 417[5] | $4.50_L^{NCSN}$ |
| BEXAR[P] | 1991/04/04 | 19:00:00.00 | 37.296 | -116.314 | 629 | $5.08_d^{NCSN}$ |
| HOYA[P] | 1991/09/14 | 19:00:00.08 | 37.226 | -116.429 | 658 | $5.40_L^{NCSN}$ |
| LUBBOCK[Y] | 1991/10/18 | 19:12:00.00 | 37.063 | -116.046 | 457 | $4.75_d^{NCSN}$ |
| BRISTOL[Y] | 1991/11/26 | 18:35:00.07 | 37.096 | -116.070 | 457 | $4.80_L^{NCSN}$ |
| JUNCTION[P] | 1992/03/26 | 16:30:00.00 | 37.272 | -116.361 | 622 | $4.82_{Lg}^{NCSN}$ |
| HUNTERS TROPHY[R] | 1992/09/18 | 17:00:00.08 | 37.207 | -116.211 | 385 | $3.87_d^{NCSN}$ |
| DIVIDER[Y] | 1992/09/23 | 15:04:00.00 | 37.021 | -115.989 | 340 | $4.13_d^{NCSN}$ |
| Little Skull Main | 1992/06/29 | 10:14:21.89 | 36.6385 | -116.2722 | 4530 | $5.31_d^{NCSN}$ |
| Little Skull Aftershock | 1992/07/05 | 06:54:10.72 | 36.6767 | -116.0178 | 6590 | $4.19_d^{NCSN}$ |
| Timber Mountain | 1995/07/31 | 12:34:45.03 | 37.1363 | -116.2057 | 7010 | $3.58_d^{NCSN}$ |
| Amargosa | 1996/09/05 | 08:16:56.09 | 36.6827 | -116.3378 | 5000 | $3.38_d^{NCSN}$ |
| Groom Pass | 1997/04/26 | 01:49:35.58 | 37.1987 | -115.9220 | 6040 | $3.72_d^{NCSN}$ |
| Indian Springs | 1997/06/14 | 19:48:19.93 | 36.5172 | -115.8133 | 7020 | $3.39_d^{NCSN}$ |
| Calico Fan | 1997/09/12 | 13:36:54.20 | 36.8422 | -116.1182 | 16560 | $3.70_d^{NCSN}$ |
| Warm Springs | 1998/12/12 | 01:41:30.33 | 37.5437 | -116.1605 | 2870 | $4.27_d^{NCSN}$ |
| Frenchman Flat 1 | 1999/01/23 | 03:00:34.82 | 36.7640 | -116.0277 | 7410 | $3.45_d^{NCSN}$ |
| Frenchman Flat 2 | 1999/01/27 | 10:44:17.80 | 36.7790 | -115.4578 | 8850 | $4.18_d^{NCSN}$ |
| Little Skull | 2002/06/14 | 12:40:45.82 | 36.6438 | -116.3448 | 8750 | $4.32_d^{NCSN}$ |
| Ralston | 2007/01/24 | 11:30:16.10 | 37.4133 | -117.0986 | 6090 | $4.09_d^{UNR}$ |
| ATRISCO Hole | 1982/08/05 | 14:21:00 | 37.0842 | -116.0065 | 640 | $3.50_S^{LNLL}$ |
| Trona Mine 1 | 1995/02/03 | 15:26:10.69 | 41.53 | -109.64 | 1000 | $5.30_b^{NEIC}$ |
| Trona Mine 2 | 2000/01/30 | 14:46:51.31 | 41.46 | -109.68 | 1000 | $4.40_b^{NEIC}$ |

[1] Names in caps are NTS explosions, last three events are collapses, and all others are earthquakes.
[2] Superscript refers to NTS region where P = Pahute Mesa; R = Rainier Mesa; Y = Yucca
[3] Explosion data from Springer et al. (2002)
[4] Explosion depth of burial from Springer et al. (2002)
[5] This is the average depth of the 3 COSO shots (BRONZE, GRAY, and SILVER)
[6] Subscript refers to magnitude type and superscript refers to magnitude source

when using $M_I$ as opposed to $M_S$. Patton (1988) added higher mode Rayleigh wave data from stations at regional distances and performed an inversion for the full moment tensor with an additional directed force component to represent spall for the

Table 2.2 Velocity model (Song et al., 1996)

| Thick (km) | $V_\alpha$ (km/s) | $V_\beta$ (km/s) | $\rho$ (g/cc) | $Q_\alpha$ | $Q_\beta$ |
|---|---|---|---|---|---|
| 2.5 | 3.6 | 2.05 | 2.2 | 100.0 | 40.0 |
| 32.5 | 6.1 | 3.57 | 2.8 | 286.0 | 172.0 |
| ∞ | 7.85 | 4.53 | 3.3 | 600.0 | 300.0 |

HARZER explosion ($m_b$5.6) at NTS. The study was later extended to 16 nearby explosions and the relationship between total seismic moment ($M_0$) and yield agreed well with previous results using $M_S$ (Patton, 1991). Dreger and Woods (2002) examined three NTS nuclear tests using data from three TERRAscope stations in southern California (180° < azimuth < 230°). The work presented here amends and extends their study to 14 more nuclear tests at the NTS, three collapses (two mine collapses and one explosion cavity collapse), and 12 earthquakes near the NTS (Figure 2.1; Table 2.1).

## 2.2 Data and Method

We implement the time-domain full-waveform inversion of regional data for the complete moment tensor devised by Minson and Dreger (2008) after Herrmann and Hutcheson (1993) based on the work of Langston (1981). In general, synthetic seismograms are represented as the linear combination of fundamental Green's functions where the weights on these Green's functions are the individual moment tensor elements. The Green's functions for a one-dimensional (1-D) velocity model of eastern California and western Nevada (Table 2.2; Song et al., 1996) are calculated as synthetic displacement seismograms using a frequency-wavenumber integration

method (Saikia, 1994). The synthetic data are filtered with a 4-pole acausal Butterworth filter with a low-corner of 0.02 Hz and a high-corner of 0.05 Hz and 0.1 Hz for events with $M_W \geq 4$ and $M_W < 4$, respectively. At these frequencies, where dominant wavelengths are tens of kilometers, we assume a point source for the low-magnitude regional events investigated in this study. The point source assumption allows for linearization in the time-domain, which is where we carry out the least-squares inversion.

We analyzed events that were digitally recorded with a high signal-to-noise ratio by more than two regional broadband stations. Three-component data were collected from a total of 52 stations from the US National Seismic Network, IRIS/USGS, Berkeley Digital Seismic Network, Trinet, and the Lawrence Livermore National Laboratory (LLNL) network (Figure 2.1). All data are freely available from IRIS via the internet except the LLNL historic network data, which is available on compact disk (Walter et al., 2004). Not all stations recorded all events, and a total of 16 stations were used in the inversion of the explosion data, which are shown in Figure 2.1. We remove the instrument response, rotate to the great-circle frame, integrate to obtain displacement, and use the same filter as for the synthetic seismograms. The LLNL network (white triangles in Figure 2.1) was composed of Sprengnether instruments with limited long-period response, and for those data we used a passband of 10 - 30 seconds for both the data and synthetics.

We calibrated the algorithm by calculating the full moment tensor for the 1992 Little Skull Mountain event (Figure 2.1). We find a solution at all depths within 5 km of the reported depth. The depth that produces Green's functions that best fit the data

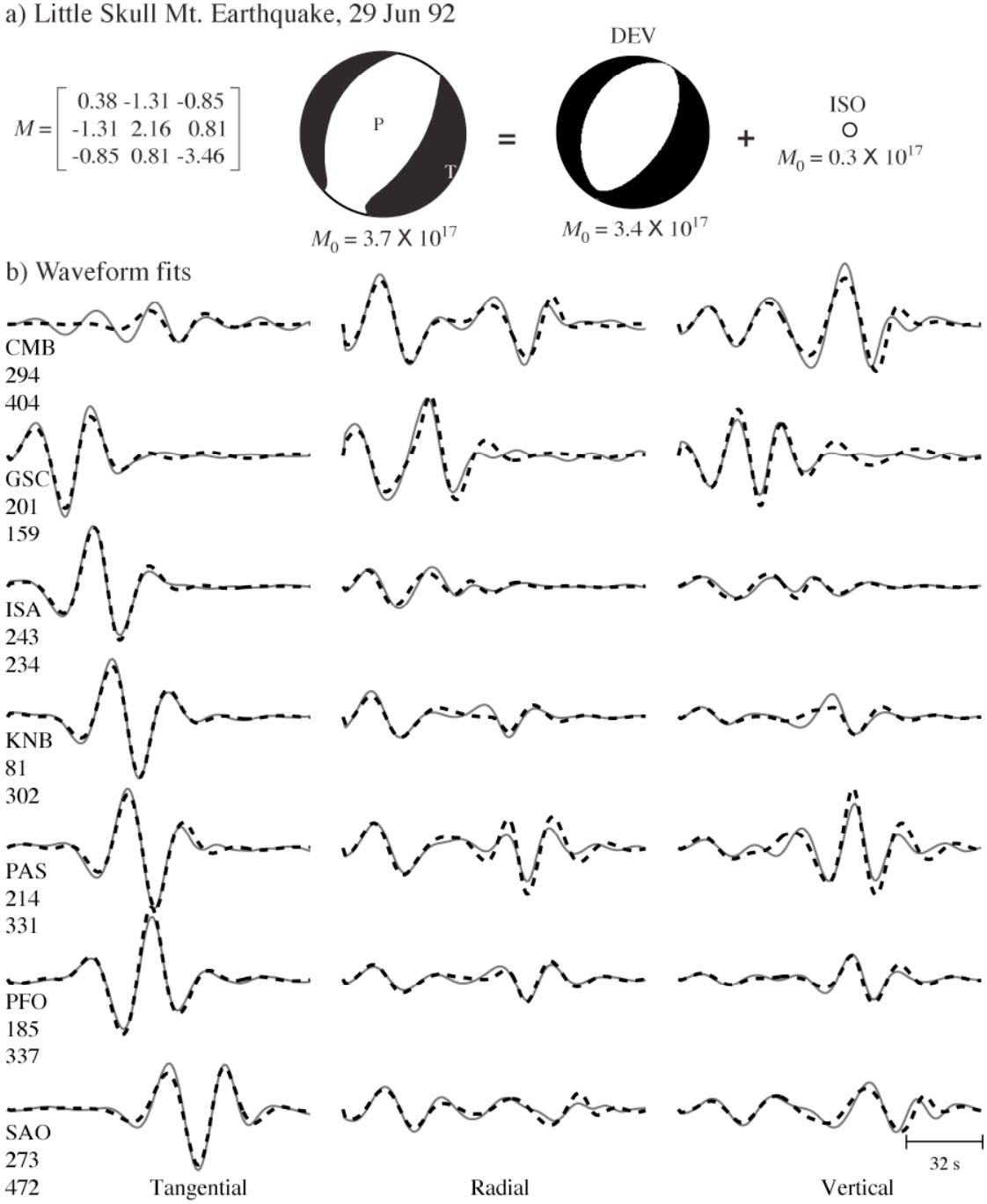


Figure 2.2 Moment tensor analysis of the 1992 Little Skull Mt. earthquake. a) The full moment tensor elements (in $10^{17}$ N-m) and mechanism are shown along with the deviatoric (DEV) and isotropic (ISO) component. The diameter of the mechanism is related to its relative moment, which is given below the mechanism in N-m. b) Data (solid grey) compared with synthetic waveforms (dashed black) produced by the full mechanism shown in (a) in 20-50 sec passband. The station name with azimuth and distance are to the left of the data.

is used in the final solution. Fit is quantified by the variance reduction (VR), which is a normalized variance given by

$$\mathrm{VR} = \left[1 - \frac{\sum_i (d_i - s_i)^2}{\sum_i d_i^2}\right] \times 100\,, \qquad (2.1)$$

where $i$ are the displacements at all times for all components at all stations, and $d$, and $s$ are the data and synthetic respectively..

We also allow the Green's functions calculated at a given distance to shift relative to the data to address small hypocentral errors and uncertainty in the velocity model used to compute the Green's functions. The shift that produces the best fit is used in the final solution. We limit the shift to less than 5 and 3 sec for high-pass corners of 0.05 and 0.10 Hz, respectively. The allowed time shift is large enough to make up for small hypocentral errors, but small enough to disallow cycle-skipping that could produce erroneous mechanisms. The sensitivity of the time shift relative to the assumed velocity model will be discussed later in the paper. The full moment tensor solution is decomposed to an isotropic and deviatoric component in Figure 2.2a. We calculate the total scalar moment ($M_0$) as defined by Bowers and Hudson (1999), where $M_0$ is equal to the sum of the isotropic moment ($M_{\mathrm{ISO}} = (M_{11}+M_{22}+M_{33})/3$) and deviatoric moment ($M_{\mathrm{DEV}}$), which is the largest deviatoric eigenvalue. For the Little Skull Mountain event we find $M_0 = 3.7 \times 10^{17}$ N-m ($M_{\mathrm{W}} = 5.6$), and the solution has a negligible isotropic moment ($M_{\mathrm{ISO}} = -0.31 \times 10^{17}$ N-m) so there is little change between the full and deviatoric solutions. The solution fits the data very well (Figure

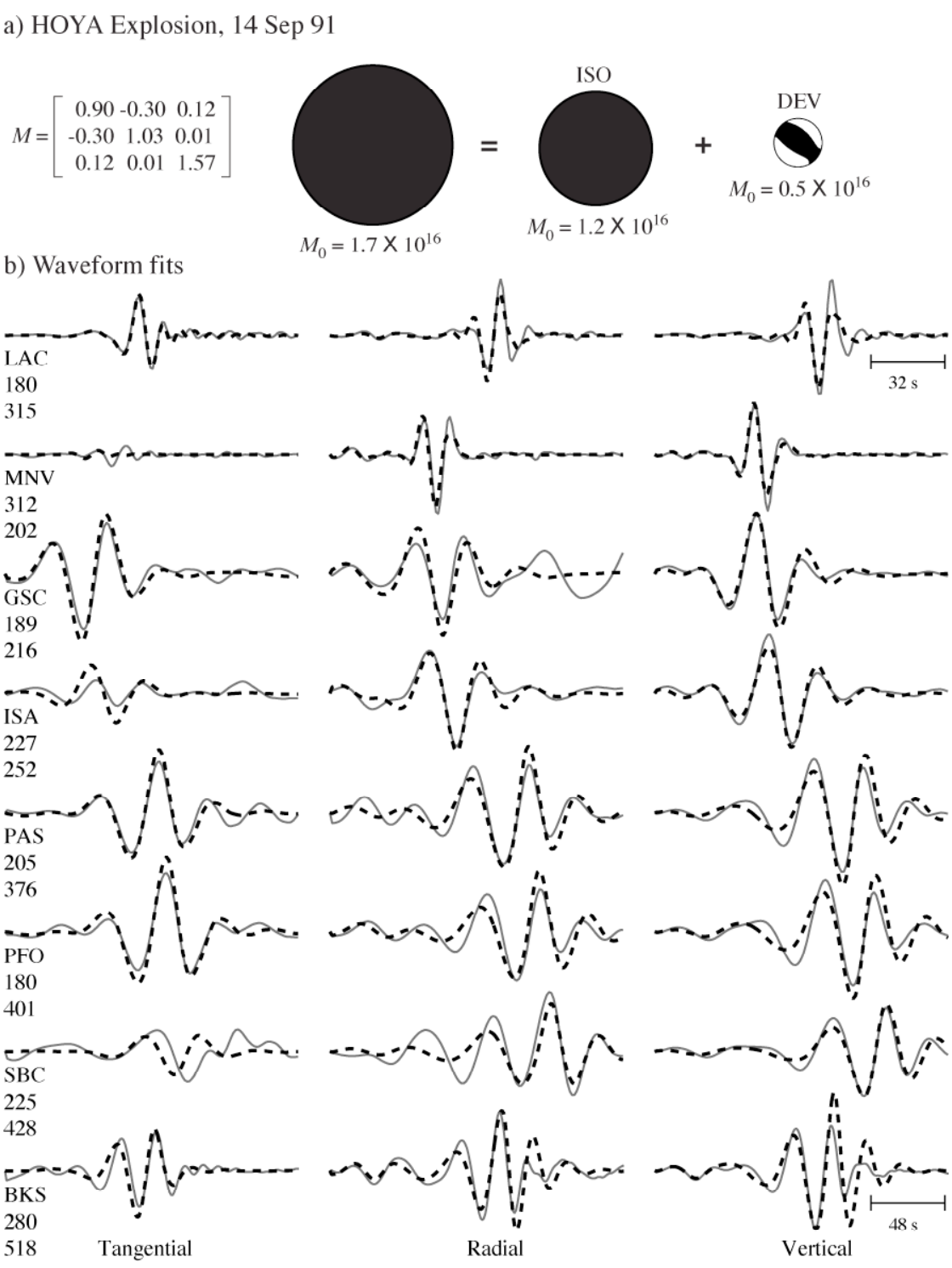


Figure 2.3 Moment tensor analysis of the 1991 HOYA nuclear test explosion similar to that given in Figure 2.2 where the moment tensor elements are in $10^{16}$ N-m. b) Data is bandpassed between 20-50 sec except LAC and MNV (LLNL network) which are bandpassed between 10-30 sec and note that BKS is on a different time scale.

2.2b) and is similar to the double-couple solution of Walter (1993), the deviatoric solution of Ichinose et al. (2003), and the full solution of Dreger and Woods (2002).

With the same algorithm we calculate the full moment tensors of 17 nuclear test explosions at the NTS (Figure 2.1). In the case of explosions and collapses we calculate Green's functions at a depth of 1 km. The sensitivity of this assumption will be investigated later in the paper. An example of the analysis is given by the solution for the 1991 HOYA test in Figure 2.3, where both the full and deviatoric moment tensors are given. The largest component in the decomposition is isotropic and it contributes 70% of the total scalar moment.

## 2.3 Results

It is difficult to grasp the source-type from the standard focal mechanism plot for events with a large non-DC component. For example, one cannot discern the relative contributions of the isotropic and deviatoric components from the full focal mechanism in Figure 2.3 for the HOYA explosion. In order to get at the tectonic contribution to the explosion, one could separate the deviatoric component into a DC and a CLVD that share the orientation of the major axis, but decompositions of this type are non-unique, where for example the DC and CLVD decomposition could be replaced by two DCs (see Julian et al. (1998) for further decompositions). In an attempt to better characterize mechanisms we follow the source-type analysis described in Hudson et al. (1989) and calculate $-2\varepsilon$ and $k$, which are given by

$$\varepsilon = \frac{-m'_1}{|m'_3|}, \tag{2.2}$$

and

$$k = \frac{M_{\mathrm{ISO}}}{|M_{\mathrm{ISO}}| + |m'_3|}, \tag{2.3}$$

where $m'_1$, $m'_2$ and $m'_3$ are the deviatoric principal moments for the N, P, and T axes, respectively, and $|m'_1| \leq |m'_2| \leq |m'_3|$. $\varepsilon$ is a measure of the departure of the deviatoric component from a pure DC mechanism, and is 0 for a pure double-couple (where [$m'_1$, $m'_2$, $m'_3$] = [0, -1, 1]) and ±0.5 for a pure CLVD (where [$m'_1$, $m'_2$, $m'_3$] = [1/2, 1/2, -1]). $k$ is a measure of the volume change, where +1 would be a full explosion and –1 a full implosion. $-2\varepsilon$ and $k$ for the Little Skull Mountain earthquake and NTS explosion, HOYA, are given in Figure 2.4a. The earthquake is almost at the origin, which defines a pure DC, whereas the nuclear test is near where a theoretical explosion would plot. In order to estimate formal error in the fit, we create moment tensor populations by bootstrapping the residuals of the fit *n*times with replacement and then use those populations of size $n$ to calculate $-2\varepsilon$ and $k$, resulting in their own populations to which we fit normal distributions. Figure 2.4a shows the population of $n$ = 1000 along with the 95% confidence region for the DIVIDER explosion. Increasing $n$ resulted in no change to the confidence regions.

Hudson et al. (1989) transform the parameters $-2\varepsilon$ and $k$ so that the displayed plot will have equal normal probability areas based on the assumption that the smallest principal moments can take any value between ± the largest absolute principal moment (Julian et al., 1998). The plot derived this way is the source-type plot and it is

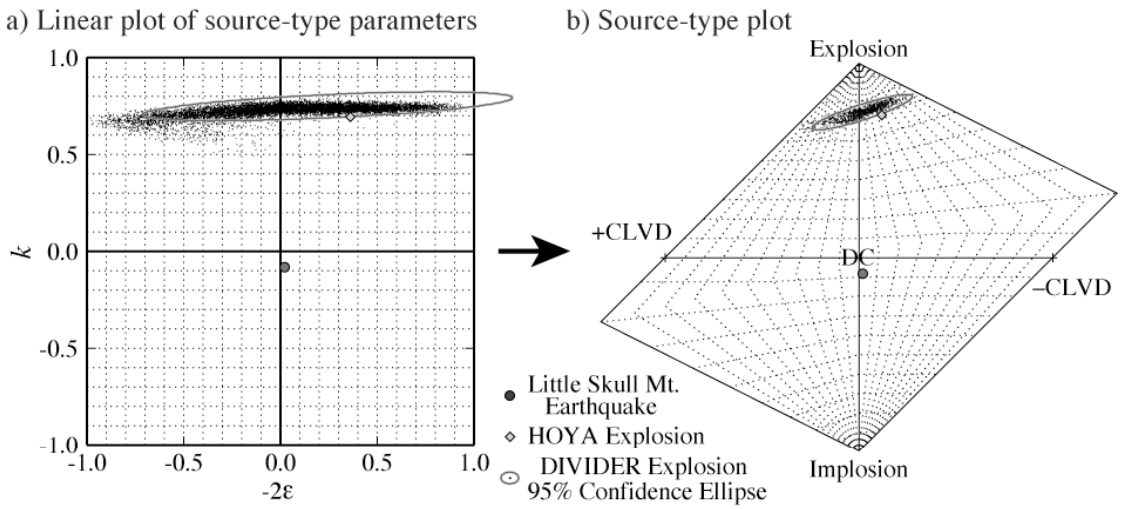


Figure 2.4. Source-type plot for the Little Skull Mt. earthquake (dark grey circle), NTS test HOYA (light grey diamond), and bootstrap population of the NTS test DIVIDER (black dots) along with its 95% confidence region (grey ellipse). a) The source-type parameters (k, −2ε) given on a linear plot. b) The source-type plot of Hudson et al. (1989) with theoretical mechanisms plotted as well.

shown in Figure 2.4b for the parameters from the Little Skull Mt. earthquake and HOYA explosion. Figure 2.4b also shows the transformed bootstrap population for the DIVIDER explosion and its associated 95% confidence region. The transformation makes the assumption of normality in the error distribution valid as can be seen by the improved fit of an error ellipse to the bootstrap population between Figure 2.4a and b. The Hudson et al. (1989) plot is a superior way to display source-type and analyze error in the parameters. The error ellipses are not shown for the Little Skull Mt. earthquake or HOYA explosion examples because the error regions are too small to notice a difference due to the transformation.

We carry out similar analyses for 11 more earthquakes and three collapses (one cavity and two mine) and produce the source-type plot in Figure 2.5 along with the 95% confidence regions. The nuclear tests occupy the region where $k > 0.5$, the

Table 2.3 Event parameters ($\times 10^{20}$ dyne-cm)[1]

| Name | $M_W$ | $M_{11}$ | $M_{12}$ | $M_{13}$ | $M_{22}$ | $M_{23}$ | $M_{33}$ | $k$ | $-2\varepsilon$ |
|---|---|---|---|---|---|---|---|---|---|
| KERNVILLE | 4.75 | 755.6 | 15.3 | -32.6 | 707.1 | 83.4 | 1696.9 | 0.62 | -0.90 |
| AMARILLO | 4.16 | 77.9 | -21.4 | 29.6 | 156.8 | 28.2 | 191.6 | 0.64 | 0.31 |
| DISKO ELM | 3.53 | 9.6 | -4.4 | -2.8 | 10.2 | 2.1 | 24.2 | 0.58 | -0.27 |
| HORNITOS | 4.72 | 835.1 | -22.3 | 79.9 | 756.3 | 21.6 | 1516.1 | 0.68 | -0.83 |
| BARNWELL | 4.73 | 548.1 | -264.2 | 91.4 | 711.8 | 210.3 | 1496.6 | 0.59 | -0.10 |
| METROPOLIS | 4.07 | 118.2 | -3.2 | 0.8 | 139.8 | -29.9 | 95.9 | 0.74 | -0.08 |
| BULLION | 5.05 | 2043.2 | -481.6 | 172.7 | 2430.5 | 574.9 | 4568.2 | 0.64 | -0.38 |
| AUSTIN | 3.60 | 17.6 | -6.2 | 0.9 | 15.9 | 4.8 | 28.9 | 0.65 | 0.26 |
| HOUSTON | 4.67 | 520.0 | -72.2 | -14.3 | 555.5 | 10.1 | 1269.2 | 0.62 | -0.70 |
| COSO | 3.64 | 18.2 | -2.8 | 5.9 | 26.9 | -0.5 | 33.4 | 0.71 | 0.21 |
| BEXAR | 4.62 | 591.6 | -139.8 | 43.5 | 792.7 | -95.7 | 994.9 | 0.74 | 0.09 |
| HOYA | 4.75 | 898.1 | -301.5 | 118.0 | 1034.9 | 9.5 | 1572.4 | 0.69 | 0.36 |
| LUBBOCK | 3.99 | 79.3 | -6.3 | 8.7 | 90.1 | -3.0 | 119.5 | 0.79 | -0.36 |
| BRISTOL | 4.06 | 56.1 | -21.3 | 19.9 | 101.5 | -3.6 | 138.3 | 0.65 | 0.30 |
| JUNCTION | 4.71 | 592.6 | -24.2 | -374.2 | 658.7 | 30.8 | 1294.5 | 0.58 | -0.63 |
| HUNTERS TROPHY | 3.62 | 14.6 | -0.7 | -2.8 | 14.9 | 1.8 | 33.4 | 0.62 | -0.92 |
| DIVIDER | 3.65 | 22.5 | -6.2 | -0.1 | 30.3 | 3.9 | 31.9 | 0.75 | 0.24 |
| Little Skull Main | 5.64 | 3802.5 | -13035.1 | -8533.9 | 21603.9 | 8079.6 | -34594.9 | -0.08 | 0.02 |
| Little Skull Aftershock | 4.17 | 36.9 | -205.6 | 7.5 | -4.8 | -3.3 | 9.6 | 0.06 | -0.04 |
| Timber Mountain | 3.73 | 9.2 | -42.9 | 4.0 | 2.6 | 6.9 | -11.1 | 0.00 | -0.38 |
| Amargosa | 3.69 | -9.4 | -2.7 | -9.3 | 8.2 | 19.2 | -34.7 | -0.27 | 0.19 |
| Groom Pass | 3.76 | 16.2 | -46.0 | 7.5 | -3.6 | -0.9 | -1.5 | 0.07 | -0.22 |
| Indian Springs | 3.57 | -4.6 | -24.2 | 0.1 | -1.6 | 2.0 | -4.6 | -0.13 | -0.08 |
| Calico Fan | 3.74 | -8.5 | -35.0 | -10.5 | 29.6 | -9.9 | -5.5 | 0.10 | -0.19 |
| Warm Springs | 4.27 | -19.7 | -192.6 | 66.7 | 208.8 | 23.1 | -22.6 | 0.17 | -0.34 |
| Frenchman Flat 1 | 3.74 | 23.1 | -21.3 | -10.2 | 33.8 | 2.4 | -28.3 | 0.19 | -0.09 |
| Frenchman Flat 2 | 4.65 | 418.0 | -468.8 | -154.6 | 893.7 | 47.8 | -247.8 | 0.30 | -0.47 |
| Little Skull | 4.66 | 50.1 | -313.1 | -186.6 | 329.9 | 327.6 | -1145.3 | -0.21 | 0.21 |
| Ralston | 3.85 | -0.5 | -66.7 | 16.5 | 13.8 | 13.9 | -10.4 | 0.01 | -0.09 |
| ATRISCO Hole | 4.52 | -340.5 | 11.6 | 7.5 | -347.3 | 60.2 | -744.9 | -0.63 | 0.91 |
| Trona Mine 1 | 4.75 | -559.1 | 5.8 | -90.7 | -548.9 | -47.3 | -1689.6 | -0.55 | 0.97 |
| Trona Mine 2 | 4.15 | -85.0 | 6.7 | 0.9 | -96.3 | -6.5 | -241.9 | -0.60 | 0.80 |

[1] Names in caps are NTS explosions, last three events are collapses, and all others are earthquakes.
1 = North; 2 = East; 3 = Down (Aki & Richards cartesian convention).

earthquakes cluster near the origin, and the collapses plot almost exactly at (1,-5/9), which is the location for a closing crack in a Poisson solid (where $[m'_1, m'_2, m'_3] = [1, 1, 3]$). Deviations from these trends will be discussed later. Moment tensor elements and source-type parameters for all events are given in Table 2.3.

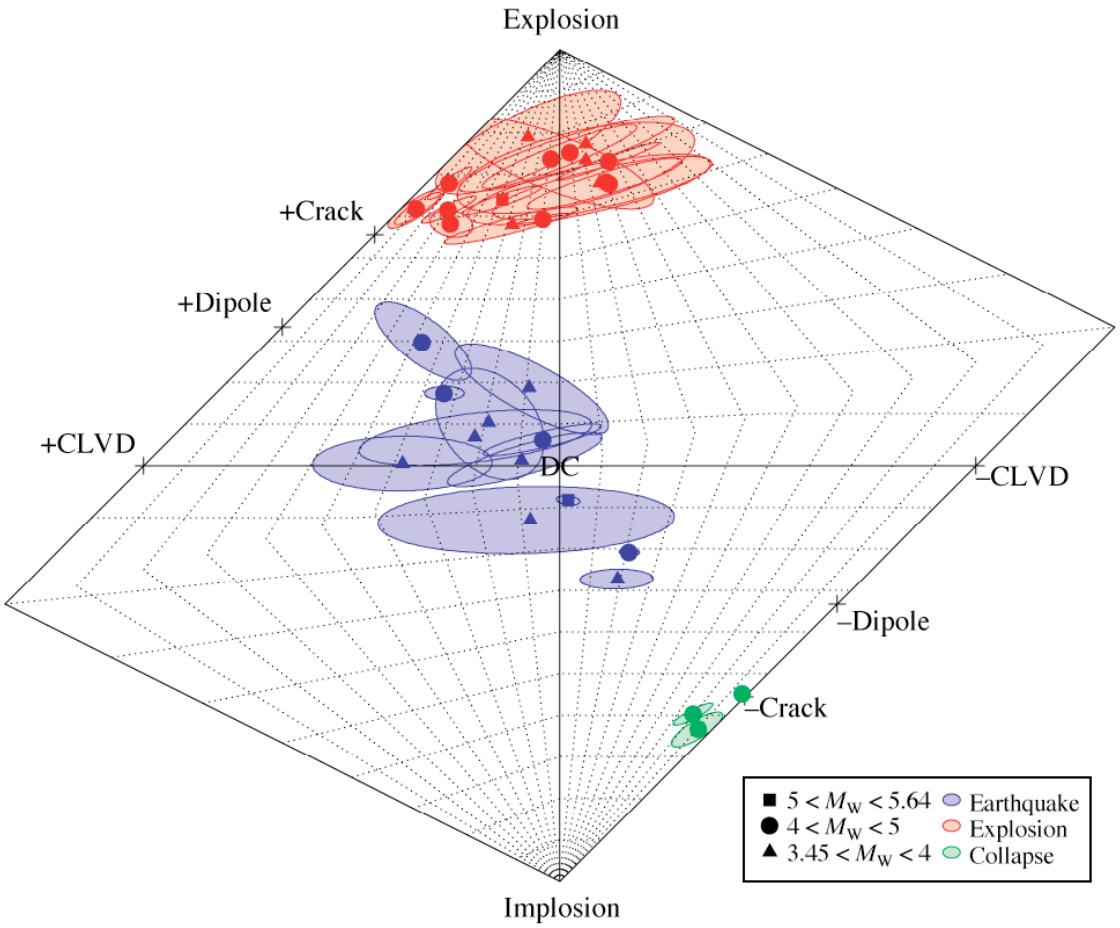


Figure 2.5. Source-type plot of the 12 earthquakes (blue), 17 explosions (red), 3 collapses (green), and their associated 95% confidence regions (shaded) analyzed in this study. The magnitude of the event is given by the symbol. The abscissa measures the amount of volume change for the source and the ordinate measures the departure from pure DC. Theoretical mechanisms (crosses) are plotted for comparison.

## 2.4 Sensitivity Analysis

The relatively small area of the confidence regions given in Figure 2.5 and the excellent synthetic seismogram fit to the data (quantified by VR) gives us great confidence that the assumed velocity model and depth are correct and the estimated moment tensor solutions are robust. However, these measures of goodness-of-fit

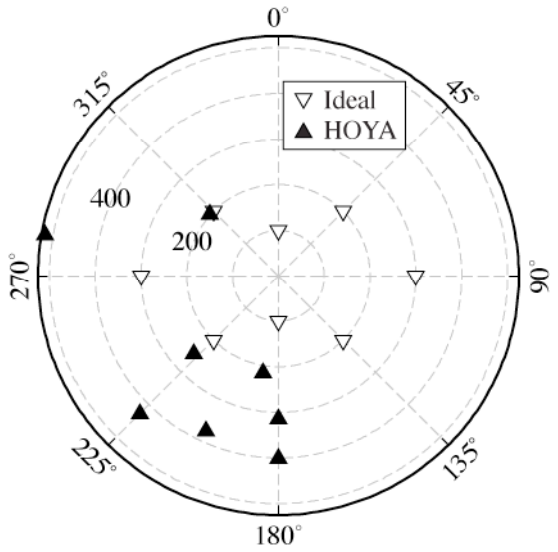


Figure 2.6. Sensitivity analysis geometry for the HOYA (black triangle) and Ideal (white inverted triangle) station configuration.

assume the underlying model used to invert the data is correct. In the following section we will test these assumptions with synthetic data from a theoretical explosion ($-2\varepsilon$=0, $k$=1) created for two experimental geometries. The first geometry, referred to as 'Ideal', is eight stations at distance increments between 100 and 300 km each separated by 45° in azimuth. The second station geometry mirrors the analysis for the HOYA explosion. The station distributions are given in Figure 2.6. The synthetic data are filtered in the same two bands (20-50s and 10-50s) used in the analysis and when combined with the two geometries results in 4 scenarios.

### 2.4.1 Noise

The error analysis presented above is due to misfit of the data by the least-squares inversion. Part of the misfit may be due to nonstationary noise and we test the sensitivity of the inversion to different signal-to-noise ratios (SNR). In order to best approximate real-world noise conditions, we derive the noise signal from data prior to the first arrival from the nuclear test METROPOLIS (10 Mar 90) at station ANMO for all three components. The amplitude of this noise signal is bandpassed to match the synthetic data and multiplied by a factor so as to create a final synthetic signal with the desired SNR (ratio of synthetic data root-mean-square amplitude to noise root-mean-square amplitude).

The noise analysis has very little frequency dependence so for clarity we only show results from the analysis in the 20 - 50 sec frequency band in Figure 2.7a. The Ideal configuration produces the best scenario where a large $k$ is retrieved (>0.3) when the SNR is greater than 2. For all scenarios $k > 0.5$ when SNR > 5. Typically, we use data with an SNR greater than 10, however there are a few cases where the SNR is close to 3. An example of this type of data is given in Figure 2.8 for the DIVIDER explosion, which produced signal that was right on the limit of acceptable SNR (see stations ELK and MHC) but still produced a well-fit solution.

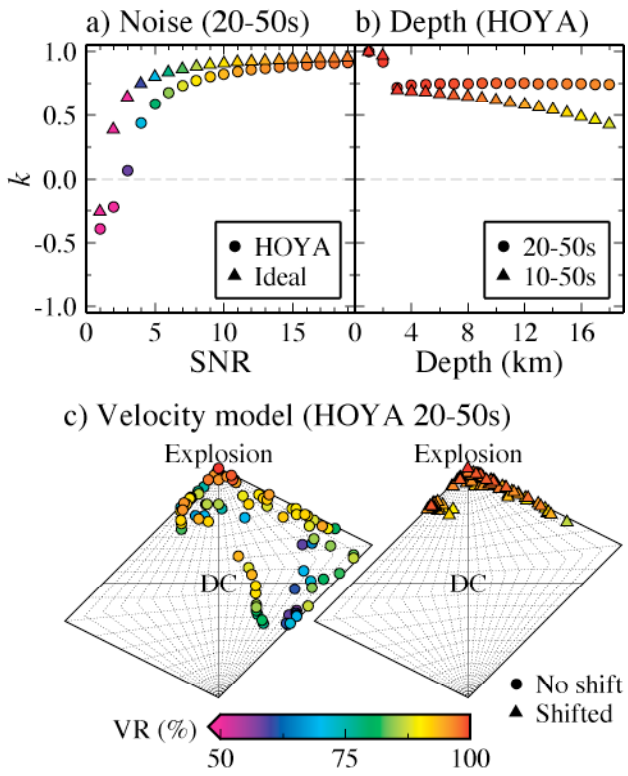


Figure 2.7. Sensitivity analysis. a) Noise is added to the inversion of 20-50 sec synthetic data while velocity model and depth (1 km) are kept fixed for the HOYA (circle) and Ideal (triangle) scenarios. b) The inversion using the HOYA configuration is carried out assuming an incorrect depth while velocity model is kept fixed for data in the 20-50 sec (circle) and 10-50 sec (triangle) band. c) The inversion using the HOYA configuration for 20-50 sec synthetic data is carried out for different three-layer velocity models where the data are not shifted relative to the Green's functions (left panel, circles) and allowed to shift less than 5 sec (right panel, triangles). The symbols are colored as a function of variance reduction (VR).

### 2.4.2 Incorrect Depth

Another source of error not incorporated into the formal error analysis is incorrectly calculated Green's functions due to ignorance of the true event depth. The method that produces the results presented above attempts to find an optimal depth for the earthquakes by perturbing the reported depth a few kilometers, performing the

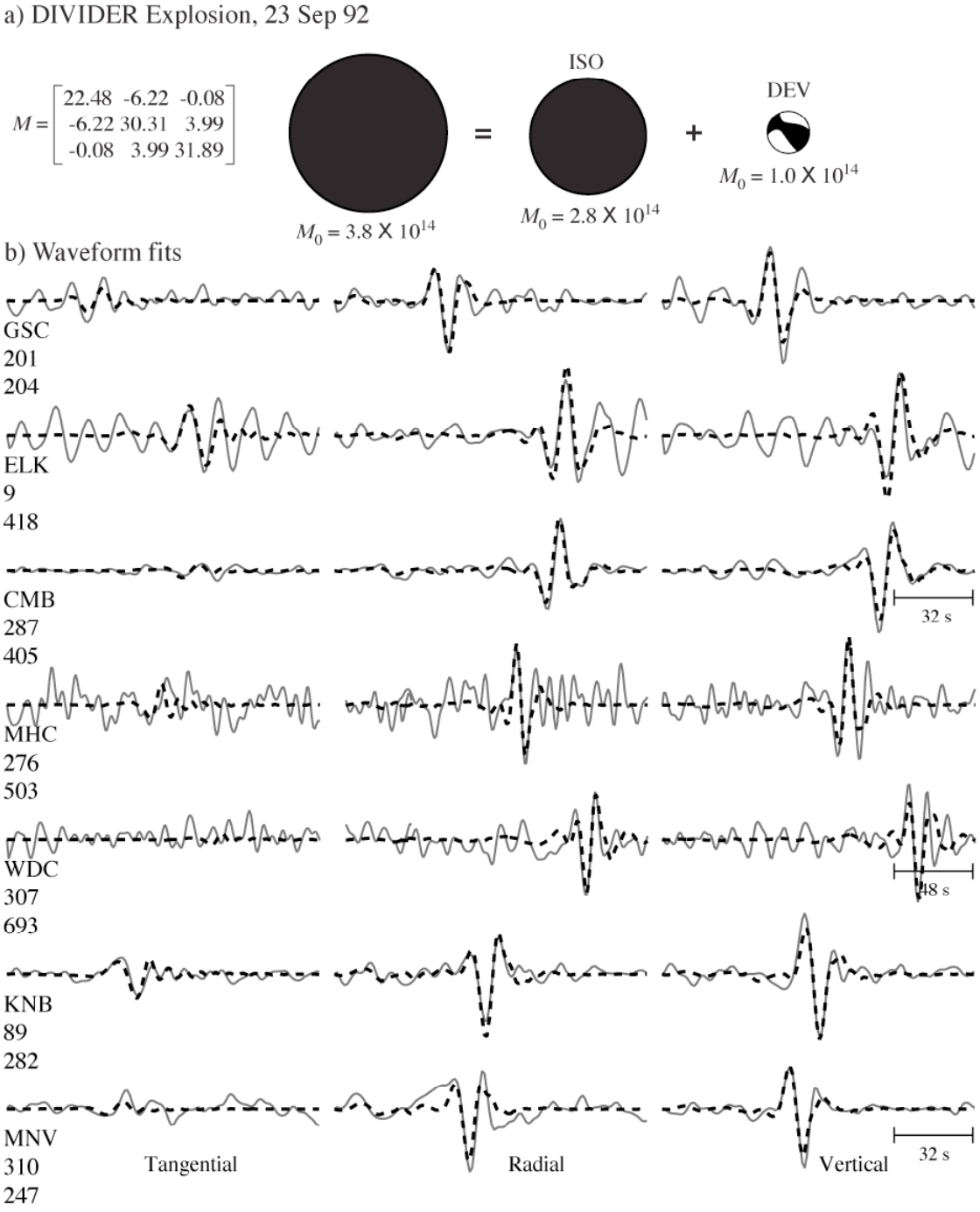


Figure 2.8. Moment tensor analysis of the 1992 DIVIDER nuclear test explosion similar to that given in Figure 2.2 where the moment tensor elements are in $10^{13}$ N-m. b) Data are bandpassed between 10-50 sec except KNB and MNV (LLNL network) which are bandpassed between 10-30 sec and note that MHC and WDC are on a different time scale.

inversion, and finding the best-fit solution. For all explosions and collapses the depth is fixed at 1 km. If this method were to be used for an event with an unknown source type, the depth could be an important source of error, as well as an important parameter for identification. We perform another synthetic test in which an explosion at 1 km is inverted with Green's functions calculated at varying depths.

The source depth analysis is not greatly affected by the two station configurations considered here, therefore we only show results for the HOYA configuration in Figure 2.7b. The result at an incorrect depth of 2 km is virtually indistinguishable from the true answer. When the source is moved to 3 km depth there is a small step decrease in $k$ due to a layer in the velocity model that begins at 2.5 km depth. However, $k > 0.5$ for incorrect depths < 17 km with slightly more sensitivity in $k$ and worse fit in the high frequency band (10 - 50 sec) compared to the low frequency band (20 - 50 sec). The relative insensitivity of the solution to mislocated depth for an explosion is different than is observed for DC events. Dreger and Woods (2002) show that the VR of the Little Skull Mountain earthquake solution is definitively maximized at the assumed true event depth. Thus while the depth sensitivity of explosions is poor, the method is able to determine depth of non-explosion sources, which also provides an important level of event screening.

### 2.4.3 Velocity Model

Finally, we test how error in the assumed Earth structure is mapped through the Green's functions to error in the solution. We start with the well-calibrated Song et

Table 2.4 Velocity model perturbations

| Parameter | Value |
|---|---|
| Sediment Thickness (km) | 1 2.5* 4 |
| Moho depth[1] (km) | 31 35* 40 |
| Sediment $V_\alpha$ (km/s) | 3.3 3.6* 5 |
| Crustal $V_\alpha$ (km/s) | 6.1* 6.202 6.485 |
| Mantle $V_\alpha$ (km/s) | 7.6 7.85* 8.15 |

* Value from Song et al. (1996)

[1] The combination of sediment thicknesses and Moho depths results in crustal thicknesses of 27, 28.5, 30, 31, 32.5*, 34, 36, 37.5, and 39 km.

al. (1996) velocity model (Table 2.2) and perturb the velocities and depths of the layers using averaged parameters from another plausible velocity model (WestUS; Ammon, 1999) and a model from Southern California (SoCal; Dreger and Helmberger, 1990). Perturbed values are given in Table 2.4, which result in a population of 243 models.

In order to produce a sensitivity test that best mimics our analysis, we use the time shift rule to filter the models. This means that we only allow velocity models that produce Green's functions where the time shift between data and synthetics that produces the best-fit solution is less than or equal to 5 or 3 sec from the theoretical arrival time for high-pass corners of 0.05 or 0.10 Hz, respectively. Primarily due to the velocity model filtering there is little difference among the scenarios so we only show source-type plots for the HOYA configuration in the 20 - 50 sec frequency band in Figure 2.7c. For this scenario the number of acceptable models is reduced to 88, and although not all possible combinations of model parameters are used, each parameter perturbation given in Table 2.4 is employed at least once.

Without shifting there are a few velocity models that produce well-fit solutions (VR>90%) with mechanisms that are almost purely DC. However, when shifting is allowed all velocity models produce good fits with highly explosive sources ($k$~>0.4).

### 2.4.4 Free-surface effects

Another consideration is the ability to resolve displacements for explosions near the surface. Since tractions normal to the vertical vanish at the free surface, the excitation coefficients associated with those tractions must vanish (Julian et al., 1998). Therefore at the free surface the moments of $M_{13}$, $M_{23}$, and the isotropic part of the $M_{ij}$ cannot be resolved. Given and Mellman (1986) showed that at a source depth of 1 km the fundamental mode excitation functions associated with the moments listed previously effectively go to zero. We investigate the potential problems associated with vanishing traction at the free surface by inverting noisy data from a synthetic explosion source at depths between 200 and 1000 m in a three-layer 1D velocity model using Green's functions calculated at those same depths.

The ability to resolve an explosive component is dependent on the station distribution, frequency and SNR of the analysis, therefore Figure 2.9 shows all 4 scenarios. An explosive component ($k$>0.5) can be resolved under favorable noise conditions at a depth greater than 300 m for all scenarios, though with error in $M_{ISO}$ between 50-150% (Figure 2.9a-d). The error is inversely proportional to the depth. For all scenarios, but the HOYA configuration at 20-50 sec (Figure 2.9a), favorable noise means SNR $\geq$ 6. The change in $M_{ISO}$ is due to a change in $M_{33}$ relative to the other

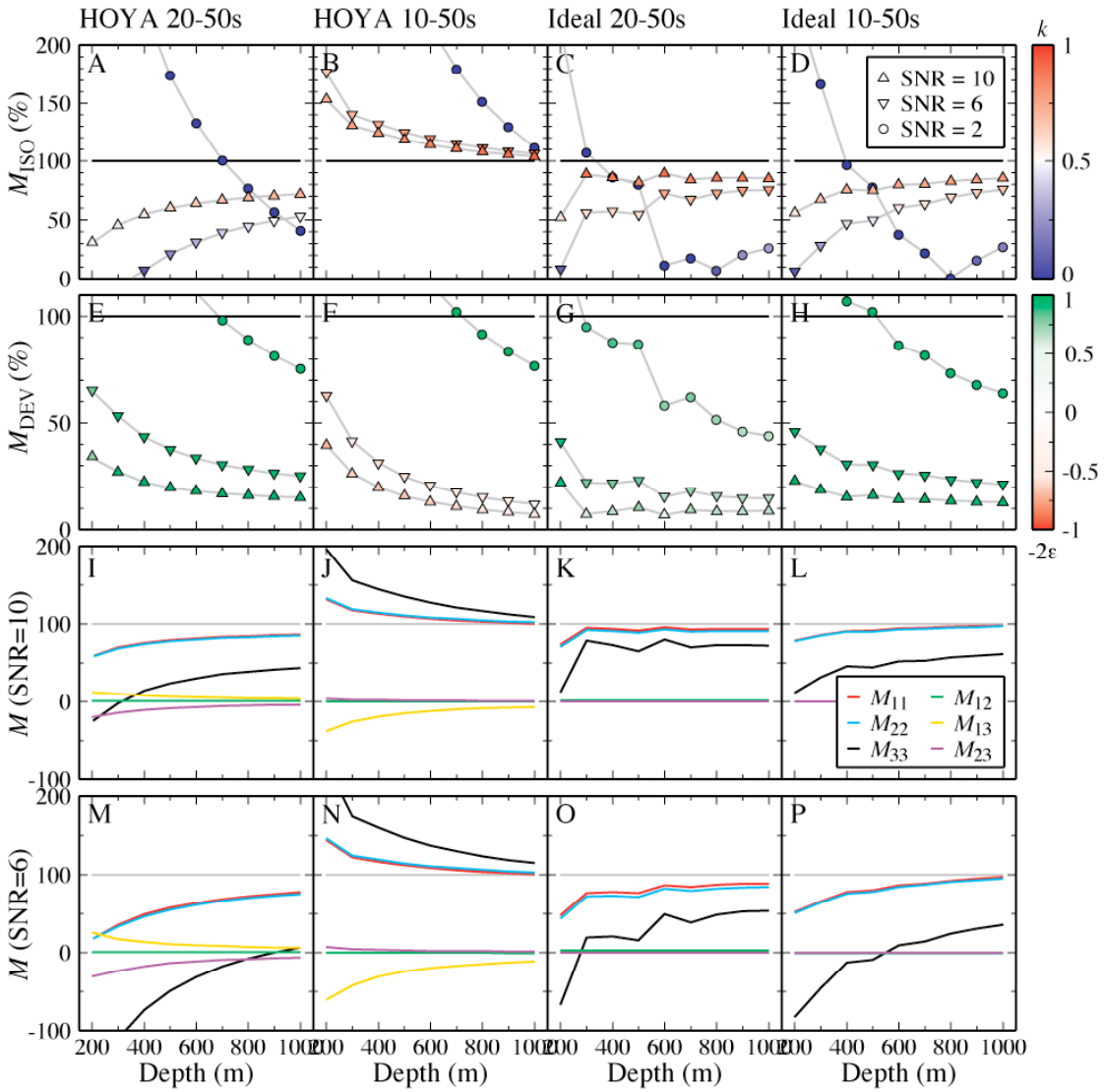


Figure 2.9. Vanishing traction sensitivity. Synthetic data for a pure explosion ($k$=1) is inverted at depths less than 1 km for varying SNR and the four scenarios discussed in the text. a-d) Resolved MISO for SNR values of 2 (circle) 6 (inverted triangle) and 10 (triangle) where the value for an inversion without noise (SNR=∞) is given by the black line (100%). $k$ is given by the color. e-h) Resolved MDEV for SNR values of 2 (circle) 6 (inverted triangle) and 10 (triangle) where the total scalar moment for an inversion without noise (SNR=∞) is given by the black line (100%), and MDEV should be 0. -2εis given by the color. i -l) Moment tensor elements for data with an SNR=10. m-p) Moment tensor elements for data with an SNR=6.

dipole components (Figure 2.9i-p), and this produces an erroneous deviatoric component. The moment of deviatoric component can be up to 50% of the theoretical isotropic moment (Figure 2.9e-h) and since it is related to the error in $M_{ISO}$ it is inversely proportional to the depth. At less than 200 m depth, the synthetic displacements become too small and the solution using these particular Green's functions is unreliable.

## 2.5 Discussion

The populations of earthquakes, explosions, and collapses separate in the source-type plot. These initial results are very encouraging and suggest a discriminant that employs the source-type plot parameters $(-2\varepsilon, k)$. Another advantage of the source-type plot is its display of 2-D error regions. In this way one can test a hypothesis that an event has a non-DC component. For example, the earthquake that is furthest to the top-left in Figure 2.5 is the Frenchman Flat earthquake. The least-squares error analysis allows one to state that the event is significantly non-DC at the 95% confidence level and it plots near the theoretical opening crack. The Frenchman Flat event was also analyzed by Ichinose et al. (2003) and found to be non-DC as well.

The source-type analysis can also be utilized to estimate model-based error as well. The error introduced by ignorance of the event location and Earth structure can be calculated with a Monte Carlo approach, where several solutions are computed for a priori distributions of the hypocentral location and Earth model obtained from independent analyses. For example, confidence regions for a given hypocentral

location as published by the NEIC can act as the a priori location distribution and the hundreds of 1-D velocity models for a given region produced from a Markov Chain Monte Carlo method as in Pasyanos et al. (2006) can act as the velocity model distribution. Each of the moment tensor solutions could then be plotted producing a scatter density, which would aid in the understanding of how parameterization choice nonlinearly affects the moment tensor solutions, and help map the solution space of best-fit moment tensors.

We try to give some insight to the depth sensitivity of the method with Figure 2.7b. In previous analyses of crustal earthquakes, the goodness-of-fit (VR) peaks at the correct depth (Dreger and Woods, 2002). If the same behavior is true of explosions, then the method could act as a discriminant if the best depth is very shallow which is atypical of earthquakes. Of course the alternative is also helpful, if an event solution shows the event to be in the typical range of earthquakes, greater than several km then the estimate provides a level of screening if not discrimination. Figure 2.7b shows that the use of this method as a precise depth discriminant is not plausible for the frequencies used here, though sensitivity does increase for the higher frequency band.

These results are a demonstration of the fact that an isotropic radiation pattern has no sensitivity to takeoff angle, which depends on depth. As shown by Dreger and Woods (2002) there is limited resolution of the shallow depth of explosions using regional distance data. Although an explosive radiation pattern alone does not have depth sensitivity, the relative excitation of low frequency body waves (Pnl) and Rayleigh waves does enable the method to discern the relatively shallower depths of explosions compared to earthquakes.

The velocity model analysis shown in Figure 2.7c suggests that the maximum shift rule used in the analysis is a good proxy for evaluating the appropriateness of the velocity model. The level of departure of a given velocity model from the true model is station distribution, frequency, and SNR dependent. Therefore, it is a good idea to perform this style of sensitivity test to evaluate the amount of deviation a certain experimental setup will allow, because if the velocity model is poorly calibrated then a good fit to the data can be obtained but the solution may be inaccurate.

Sileny (2004) investigated the sensitivities of the deviatoric solution and found that velocity perturbations of more than 30% and event depths mislocated by two times the actual depth still return an accurate solution. A further consideration is the assumption of an isotropic Earth structure in the presence of anisotropic data, which may produce a spurious CLVD component (Sileny and Vavrycuk, 2002). Fortunately, the 1-D velocity model seems to be a good approximation in the presence of smoothly varying 3-D heterogeneity (Panning et al., 2001) for the frequency band and regional distances employed here.

The change in moment due to the loss of traction at the free surface affects yield estimation, though event discrimination is still reliable at high SNR. A result of this change in moment is that the deviatoric moment becomes non-zero and could be significant at very shallow depths (Z<500 m) and low SNR (SNR<6). The moment manifests as a CLVD component, which means that interpretation of non-isotropic energy may be flawed for shallow events even with high SNR data. Though as Figure 2.9 suggests this effect is station configuration, frequency, and SNR dependent. There is quite a difference in $M_{ISO}$ determined for different frequency bands for the HOYA

configuration (Figure 2.9a-b), whereas there is only a slight difference for the Ideal configuration (Figure 2.9c-d). Also, the high frequency scenario of the HOYA configuration is relatively less sensitive to low SNR than other scenarios (Figure 2.9b).

The explosions analyzed here do not have as much non-isotropic energy as has historically been observed at NTS and in other regions (Walter and Patton, 1990; Ekstrom and Richards, 1994). This may be due to the "wearing out" of the test site over time (Aki and Tsai, 1972), so future work will expand the dataset of explosions to encompass other regions exhibiting exotic records like the "reversed" Rayleigh waves observed for the 1998 Indian tests (Walter and Rodgers, 1999). Future work will also address more challenging station configurations and noise considerations as is commonly found in recent nuclear tests. As shown in this study, a robust constraint on the isotropic component is station configuration, signal bandwidth, and data-quality dependent. Therefore, future work will test the extent to which an isotropic component can be resolved and believed for specific previous and potential future test scenarios.

## 2.6 Conclusions

Nuclear test explosions from NTS and earthquakes from the surrounding region separate into specific populations according to source-type parameters, which are based on relative magnitudes of isotropic and deviatoric moments. The separation allows for anomalous event identification and discrimination between explosions, earthquakes, and collapses. Synthetic tests show that a mislocation in depth and small

deviations in a simple 1D velocity model still recover a significant isotropic component, though Earth complexity is inadequately represented by a three-layer structure. We also assess error due to vanishing traction at the free surface and are able to resolve a reliable mechanism at depths greater than 300 m for data with a good SNR.

## 2.7 Error Analysis Methods

This section is a detailed description of the error analysis described in Chapter 2. As an example we will use the DIVIDER test. The data and best-fit solution for DIVIDER is given in Figure 2.8 and we will describe the steps that went into producing the error ellipse for DIVIDER shown in Figure 2.4.

The standard method uses the covariance matrix weighted by the mean-square-error (mse) of the residuals. These are calculated by first using the standard linear model

$$\mathbf{d} = \mathbf{Gm}, \tag{2.4}$$

where **d** is the data vector (displacement amplitudes), **G** is the Green's function matrix, and **m** is the model vector (a six element vector, the independent elements of the seismic moment tensor). The residual error (or residuals) is

$$\mathbf{r} = \mathbf{d} - \mathbf{Gm}. \tag{2.5}$$

To find **m** we first weight the inversion by assigning a weight to each data point as

$$\mathbf{w} = \frac{\mathbf{r}_{\min}}{\mathbf{r}}, \tag{2.6}$$

where $\mathbf{r}_{\min}$ is the distance to the closest station and **r** is the distance to the station that made the measurement. The weight matrix, **W**, has **w** along its diagonal. We can now invert for **m**, the best-fit model in a least-squares sense with

$$\mathbf{m} = (\mathbf{G}^{\mathbf{T}}\mathbf{W}\mathbf{G})^{-1}\mathbf{G}^{\mathbf{T}}\mathbf{W}\mathbf{d}, \tag{2.7}$$

which is also the maximum likelihood solution.

The covariance matrix is given by

$$\mathbf{C} = (\mathbf{G}^{\mathbf{T}}\mathbf{W}\mathbf{G})^{-1} \tag{2.8}$$

Since we don't know the true error in the data we approximate it by looking at the residuals so to find the estimated covariance matrix $\mathbf{C}_{\text{est}}$ we scale $\mathbf{C}$ by the *mse* of the residuals

$$mse = \frac{\sum(\mathbf{d} - \mathbf{G}\mathbf{m})^2}{a - b}, \tag{2.9}$$

where $a$ is the length of the data and $b$ is the number of model parameters, and

$$\mathbf{C}_{\text{est}} = mse \cdot \mathbf{C}. \tag{2.10}$$

The standard errors for $\mathbf{m}$ are given by the square-root of the diagonal of $\mathbf{C}_{\text{est}}$. This method assumes the error is independent and normally distributed. In the case of DIVIDER the standard errors are (in the order, $m_{xx}$ $m_{xy}$ $m_{xz}$ $m_{yy}$ $m_{yz}$ $m_{zz}$)

$$m_{std} = \begin{bmatrix} 1.96 & 0.39 & 1.59 & 1.94 & 1.88 & 8.42 \end{bmatrix}, \tag{2.11}$$

and its associated covariance matrix

$$C_{est} = \begin{bmatrix} 3.87 & 0.04 & 0.02 & 3.50 & 0.06 & 15.67 \\ 3.5 & 0.01 & 0.01 & 3.76 & 0.03 & 15.74 \\ 15.67 & -0.04 & 0.05 & 15.74 & 0.18 & 70.89 \\ 0.04 & 0.15 & 0.01 & 0.01 & -0.01 & -0.04 \\ 0.02 & 0.01 & 2.51 & 0.01 & -0.42 & 0.05 \\ 0.06 & -0.01 & -0.42 & 0.03 & 3.54 & 0.18 \end{bmatrix}. \tag{2.12}$$

However, the assumption of normality may not be valid, as is the case for DIVIDER where the residuals do not have a well-fit normal distribution (Figure 2.10). In the case where the underlying distribution may not be well understood a good method to approximate the error is the Bootstrap method. All my knowledge of this topic comes from a handout given at David Brillinger's time-series statistics course, the MATLAB documentation for 'bootstrp', and my bible along this linear inversion

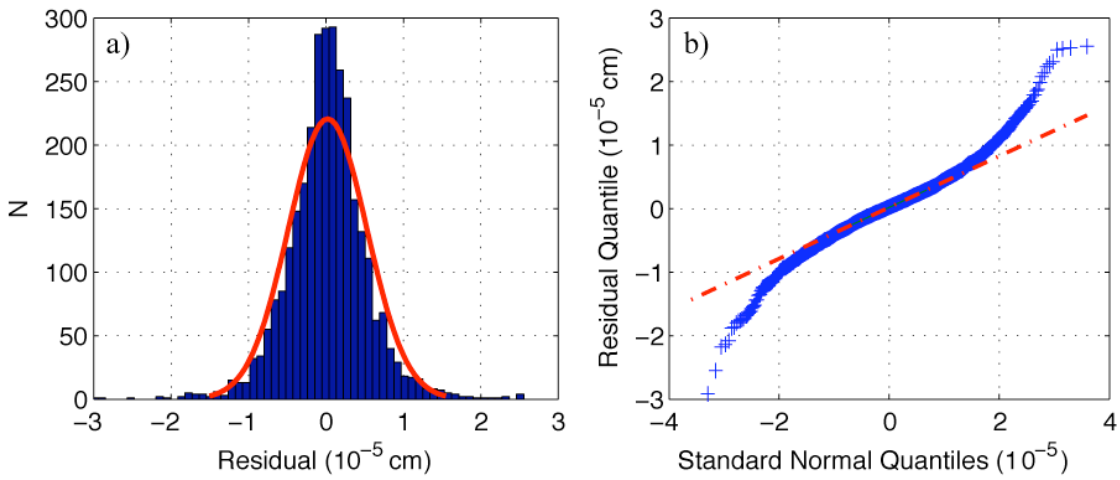


Figure 2.10. Residual analysis. a) Residual histogram with normal distribution fit. b) Quantile-quantile plot for the residual population (crosses) versus a normally distributed population (line). If the residual population acted as a normal distribution it would follow the line.

journey, the text by Aster et al. (2005). The method I use is termed 'bootstrap the residuals'. This method creates new data realizations by drawing values from the population of residuals and adding them to the original synthetic data that were predicted using the best-fit model. This concept is shown in Figure 2.11 for a few data realizations using DIVIDER. The 'new' data is inverted and a new model is calculated. This is done *n* times with replacement to come up with a population of models of size *n*.

You can then use this population of models, in our case an *n* by 6 matrix **m**, to create an empirical estimate of the covariance matrix $\mathbf{C}_{\text{boot}}$. First calculate

$$\mathbf{A} = \mathbf{m} - \overline{\mathbf{m}}, \tag{2.13}$$

where $\overline{\mathbf{m}}$ is the average model (or best-fit model) and then

$$\mathbf{C}_{\text{boot}} = \frac{\mathbf{A}^{\mathrm{T}}\mathbf{A}}{n}, \tag{2.14}$$

which for the case of DIVIDER is

$$C_{boot} = \begin{bmatrix} 3.26 & 0.00 & 0.13 & 3.04 & 0.13 & 13.59 \\ 3.04 & -0.02 & 0.12 & 3.40 & 0.12 & 13.95 \\ 13.59 & -0.09 & 0.48 & 13.95 & 0.50 & 62.45 \\ 0.00 & 0.14 & 0.00 & -0.02 & -0.02 & -0.09 \\ 0.13 & 0.00 & 2.27 & 0.12 & 0.07 & 0.48 \\ 0.13 & -0.02 & 0.07 & 0.12 & 2.69 & 0.50 \end{bmatrix}, \quad (2.15)$$

and therefore the standard error of the model parameters is

$$m_{std} = \begin{bmatrix} 1.80 & 0.37 & 1.51 & 1.84 & 1.64 & 7.90 \end{bmatrix}. \quad (2.16)$$

But the real reason I like this method is because I'm lazy and this makes error propagation easy. You can just calculate the source-type parameters (or whatever you want) for each of the *n* models (this is what you see in Figure 2.4) and then do the $\mathbf{C}_{boot}$ calculation to find the standard errors (diagonal of $\mathbf{C}_{boot}$) and the error ellipse using the standard diagonalization of $\mathbf{C}_{boot}$ (see Aster et al. (2005) eq 2.42). For example, to find the 95% confidence interval of the source-type parameters, *k* and $\varepsilon$, first calculate *n k*s and $\varepsilon$s from the **m** population to make a new *n* by 2 matrix where the columns are **k** and $\boldsymbol{\varepsilon}$. Find the $\mathbf{C}_{boot}$ and diagonalize to get the eigenvalues and vectors, $\boldsymbol{e}$ and **V**, respectively. **V** is the ellipse axes with lengths equal to the square-root of $\boldsymbol{e}$ scaled by the 95% value of a chi-squared distribution (because we treat m as a random variable). You can discretely draw out this ellipse with

$$\mathbf{E} = \Phi \sqrt{\chi^2_{0.95} \cdot \mathrm{diag}(\boldsymbol{e})}\ \mathbf{V}, \quad (14)$$

or in Matlab:

```
[V,e] = eig(C);
E = [cos(p)', sin(p)'] * sqrt(e*chi2inv(0.95,2)) * V';
```

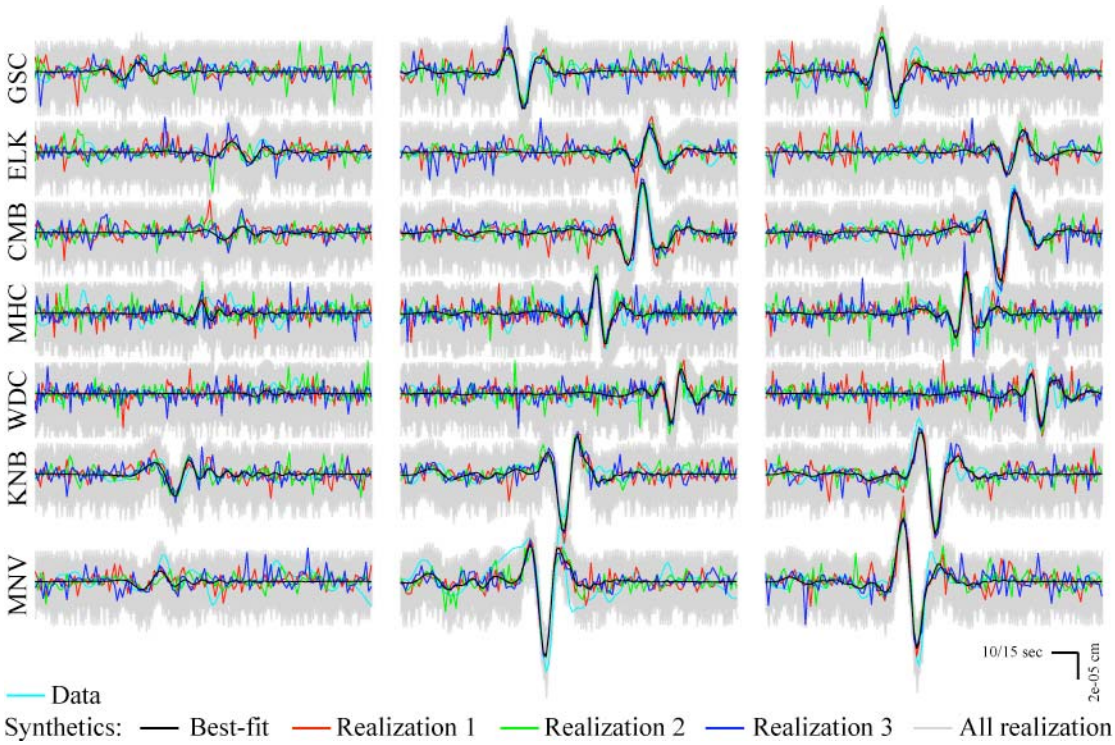


Figure 2.11. Bootstrapping the residuals for the DIVIDER example (see Figure 2.8). Cyan is the data and black is the best-fit model from which the residual population is created. Those residuals are then randomly and with replacement added to the best-fit model 1000 times to create the light gray traces. Three of those realizations are given by the red, blue and green traces.

and then add the mean parameters to this traced ellipse. Please note that I do the transformation into the source-type space to calculate the ellipse because the transformation in probability space is linear (Thank you, Hudson et al. (1989)).

# Chapter 3

## Source Characterization of the 6 August 2007 Crandall Canyon Mine Seismic Event in Central Utah

Published as: Ford, S. R., D. S. Dreger, and W. R. Walter (2008), Source Characterization of the 6 August 2007 Crandall Canyon Mine Seismic Event in Central Utah, *Seis. Res. Lett.*, 79 (5), 637-644.

### 3.1 Introduction

On August 6, 2007 a local magnitude 3.9 seismic event occurred at 08:48:40 UTC in central Utah. The epicenter is within the boundaries of the Crandall Canyon coal mine (c.f. Pechmann et al., this volume). We performed a moment tensor analysis with complete, three-component seismic recordings from stations operated by the USGS, the University of Utah, and EarthScope. The analysis method inverts the seismic records to retrieve the full seismic moment tensor, which allows for interpretation of both shearing (e.g., earthquakes) and volume-changing (e.g., explosions and collapses) seismic events. The results show that most of the recorded seismic wave energy is consistent with an underground collapse in the mine. We contrast the waveforms and moment tensor results of the Crandall Canyon Mine seismic event to a similar sized tectonic earthquake about 200 km away near Tremonton, Utah, that occurred on September 1, 2007. Our study does not address the actual cause of the mine collapse.

We apply the moment tensor analysis techniques described in Ford et al. (2007) to improve our understanding of the source of the seismic waves for two very different recent events in Utah. Ford et al (2007) implement the time-domain full regional waveform inversion for the complete moment tensor (2nd rank tensor, $M_{ij}$) devised by Minson and Dreger (2007) after Herrmann and Hutchenson (1993) based on the work of Langston (1981). Moment tensors are determined by matching synthetic seismograms to data at periods where the Earth can be characterized by a simple plane layer model. The complete moment tensor allows for a characterization of the relative amounts of deviatoric and isotropic ($M_{ij}$ where $i=j$) source components, and a constraint on the source depth. The isotropic component is related to the volume change associated with a source (Muller, 1973), and in the case of a collapse this volume change is expected to be significant.

In general, synthetic seismograms are represented as the linear combination of fundamental Green's functions where the weights on these Green's functions are the individual moment tensor elements. The Green's functions for a one-dimensional (1-D) velocity model of eastern California and western Nevada (Table 2.2; Song et al., 1996) are calculated as synthetic displacement seismograms using a frequency-wavenumber integration method (Saikia, 1994). The synthetic data is filtered with a 4-pole acausal Butterworth filter with a low-corner of 0.02 Hz and a high-corner of 0.1 Hz (10-50s period). The high corner of the filter was chosen so as to achieve a good signal-to-noise ratio while keeping it low enough to assume a point-source at the wavelengths investigated. The low corner was chosen empirically and for stability. At these frequencies, where the dominant wavelengths are approximately 30 to 150 km,

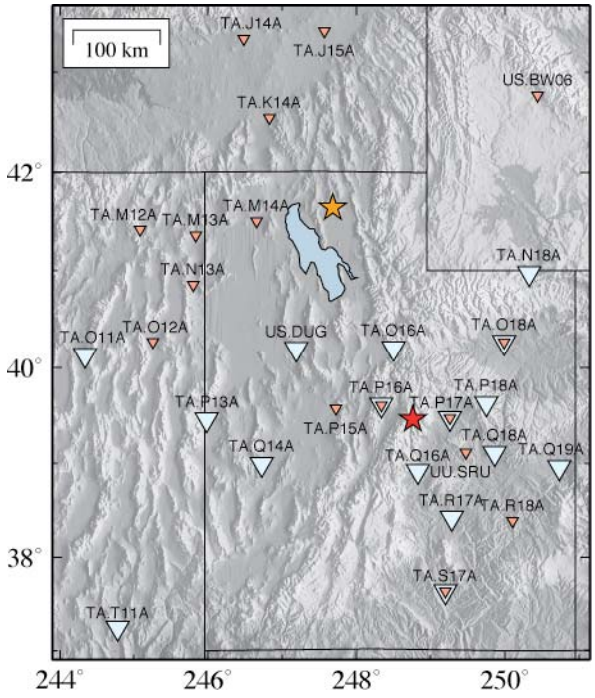


Figure 3.1. Map with locations of the August 6, 2007 Crandall Canyon Mine event (red star) and September 1, 2007 event near Tremonton, Utah (orange star) and stations used in the inversion of the events shown with light blue and light red inverted triangles, respectively.

we assume a point source for the low-magnitude regional events investigated in this study. The point source assumption allows for linearization in the time-domain, which is where we carry out the least-squares inversion. The data is processed by removing the instrument response, rotating to the great-circle frame of reference, integrating to obtain displacement, and filtering to the same frequency band as the synthetic seismograms.

The broadband stations from the USGS, the University of Utah and EarthScope's USArray networks provide excellent azimuthal coverage of the event at the Crandall Canyon Mine in central Utah on August 6, 2007. Over 200 stations

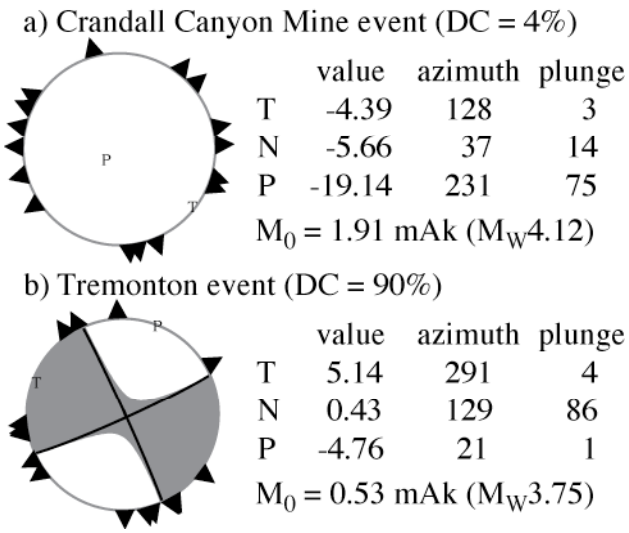


Figure 3.2. Best-fit mechanisms for the a) Crandall Canyon Mine event and b) Tremonton, Utah event. Triangles are positioned at the azimuth to the stations used in the inversion. The principal axes and values are given along with the total scalar moment ($M_0$) and moment magnitude ($M_W$).

recorded this event well, and we choose three-component data from the 16 best stations, based on signal to noise level and azimuthal coverage to perform the inversion. We will compare the Crandall Canyon Mine event results with those from an earthquake about 200 km to the north that occurred on September 1, 2007 near Tremonton, Utah. Figure 3.1 shows the locations of the events and stations used in the inversions.

### 3.2 Analysis

The Green's functions for the Crandall Canyon Mine event were calculated at a depth of 1 km, consistent with the shallow depth reported for this event. We will test this assumption in a later section. The best-fit moment tensor has a total scalar seismic

moment of 1.91 mAk (The 2007 IUGG/IASPEI General Assembly in Perugia, Italy recommends $10^{18}$ N-m equal 1 Aki [Ak], so that 1.91 mAk is $1.91 \times 10^{15}$ N-m), corresponding to a moment magnitude ($M_W$) of 4.12. Total scalar seismic moment, $M_0$, is equal to the trace of the full moment tensor divided by three, plus the largest deviatoric principal moment (Bowers and Hudson, 1999). The mechanism is one that is dominated by implosive isotropic energy, and predicts dilational (down) first-motions at all azimuths as shown in Figure 3.2a. The waveform fits to the data using this mechanism are excellent as shown in Figure 3.3 and give a 54.1% variance reduction (VR), where 100% VR is perfect fit. We compare this mechanism with one obtained for the earthquake near Tremonton, Utah. For the Tremonton event the depth that produced the best fit is 9 km and the mechanism is dominantly double-couple (DC) with a $M_W$ of 3.7 as shown in Figure 3.2b. Waveform fits are excellent as shown in Figure 3.4, with a 65.7% VR. In contrast to the Crandall Canyon Mine event, this mechanism predicts both compressional and dilational P-wave first motions in contrast to the Crandall Canyon Mine event.

We compare the best-fit mechanism for the Crandall Canyon Mine event with other potential mechanisms using the best six stations (Figure 3.5). As with the 16-station analysis, the full solution provides a good fit to the data (with an improved VR of 72.8%). We also calculate the best-fit deviatoric solution, which zeros out the isotropic component by setting $M_{zz} = -(M_{xx} + M_{yy})$. The deviatoric solution fits the data poorly (VR of 41.8%) and does not adequately produce energy on the radial and vertical traces to fit the data, especially at the nodal station DUG. We also test a best-fit pure closing crack with the axis in the horizontal plane, or a horizontal closing

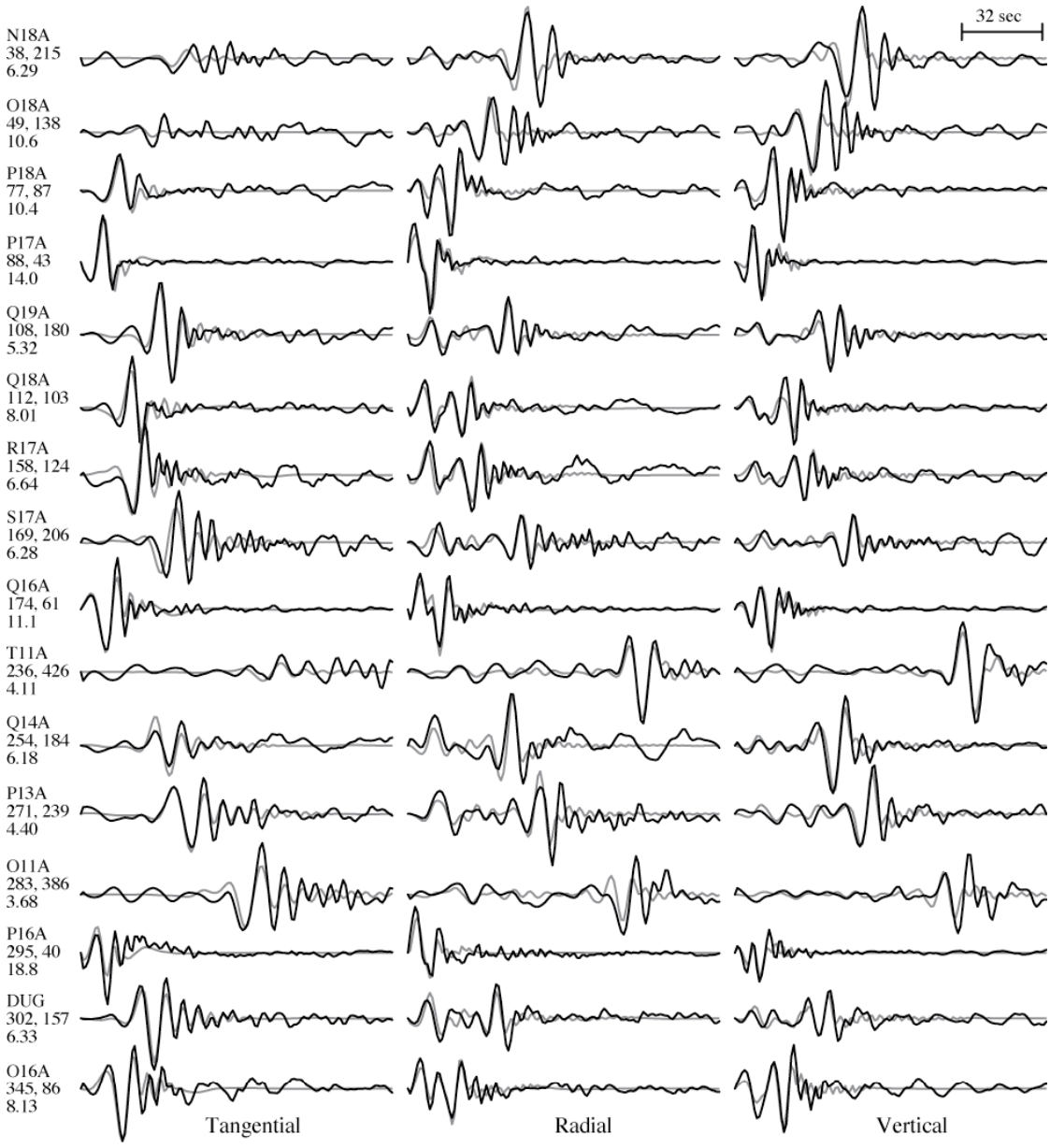


Figure 3.3. Data (black) and synthetics (grey) generated using the mechanism for the Crandall Canyon Mine event given in Figure 3.2a. To the left of each set of traces are the station, azimuth, and distance in km to the event. The traces are ordered by azimuth and are normalized to the maximum amplitude for a set of three-component recordings, where the amplitude is given in $10^{-7}$ m on the last line to the left of the traces.

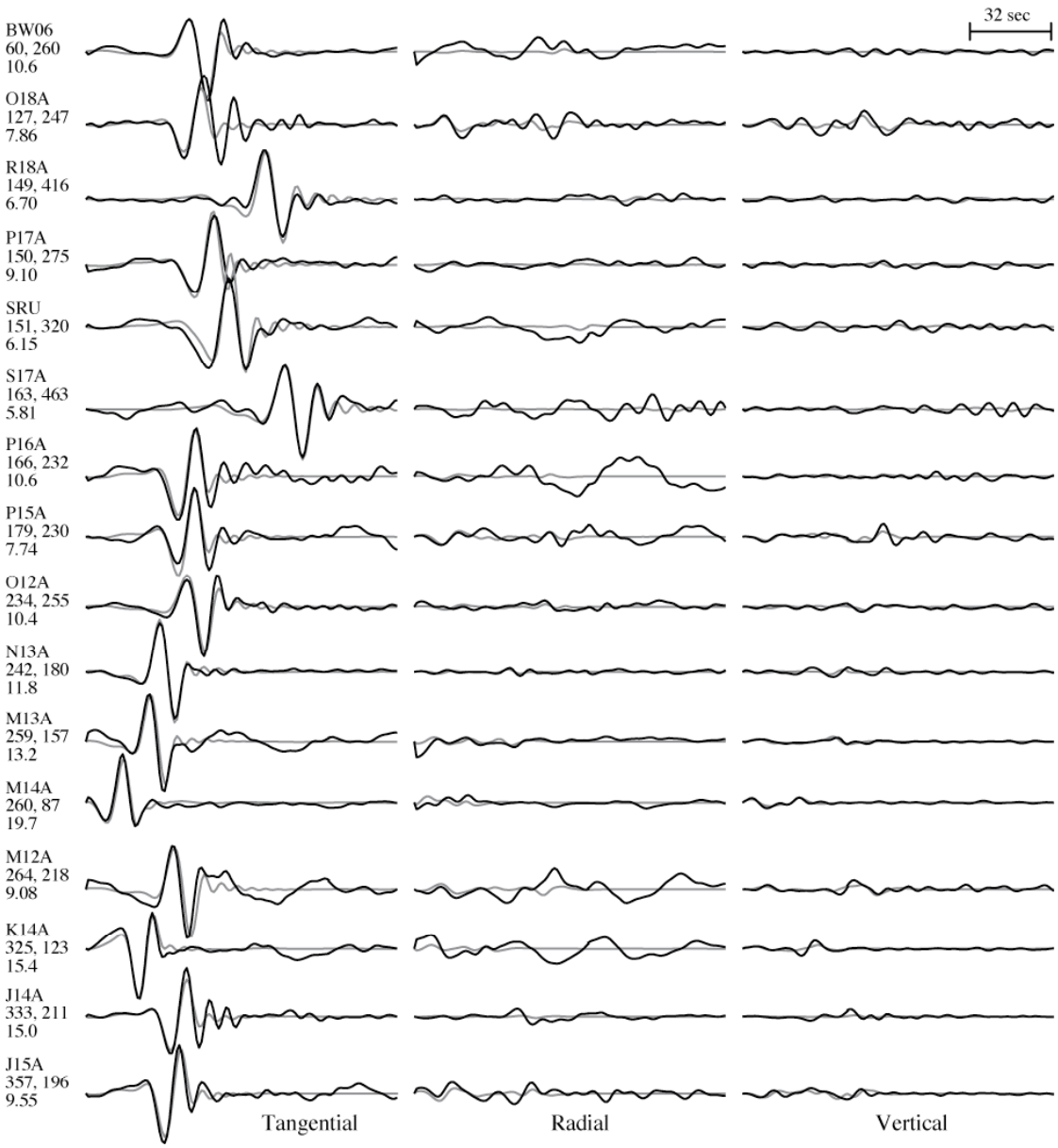


Figure 3.4. Data (black) and synthetics (grey) generated using the mechanism for the Tremonton event given in Figure 3.2b. To the left of each set of traces are the station, azimuth, and distance in km to the event. They are ordered by azimuth and are normalized to the maximum amplitude for a set of three-component recordings, where the amplitude is given in $10^{-7}$ m on the last line to the left of the traces.

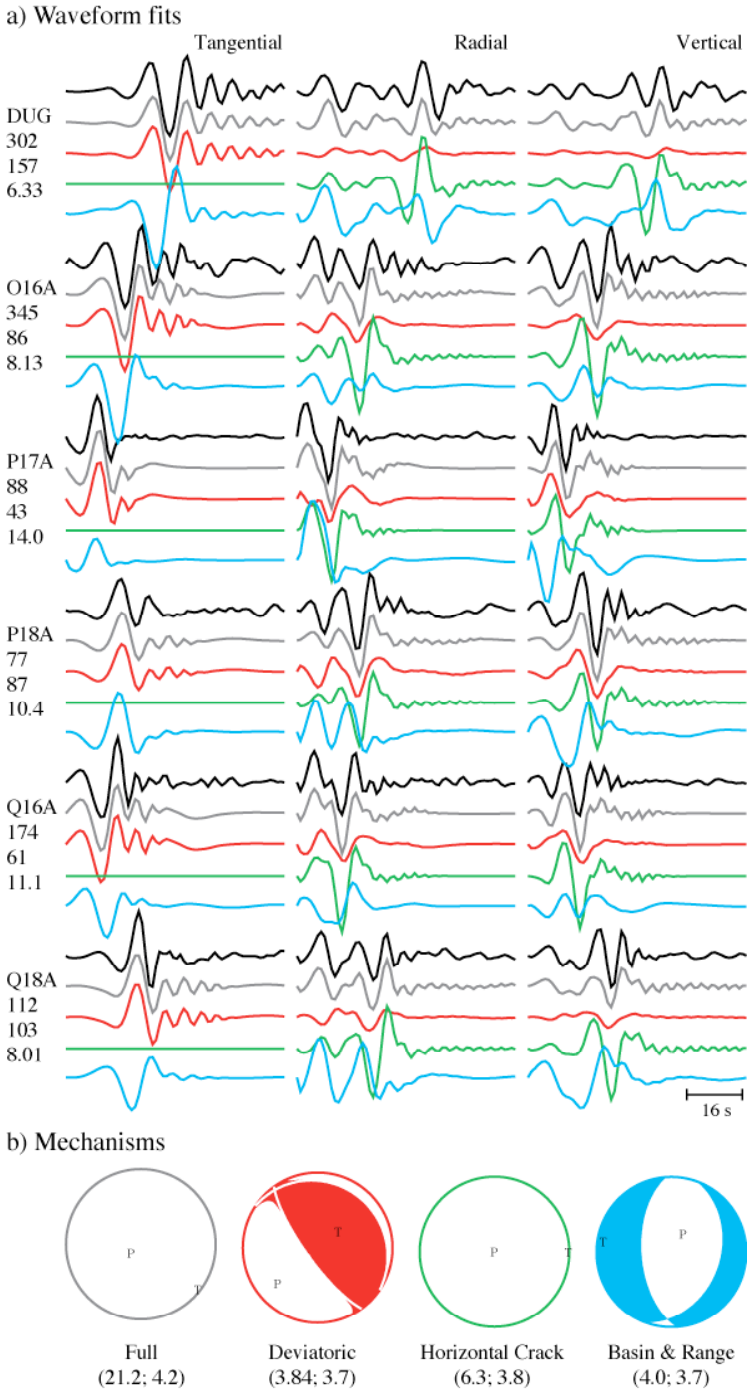


Figure 3.5. Comparison of mechanisms. Data (black) is compared with predicted waveforms for 4 mechanisms: Best-fit full solution (grey); Best-fit deviatoric solution (red); Horizontal crack (green); and a typical Basin & Range normal event (cyan). $M_0$ (in $10e^{14}$ N-m) and $M_W$ are given below the focal mechanism plot for each type. To the left of each set of traces are the station, azimuth, and distance in km to the event. Traces are normalized to the maximum amplitude of the data, which is given in $10^{-7}$ m on the last line to the left of the traces.

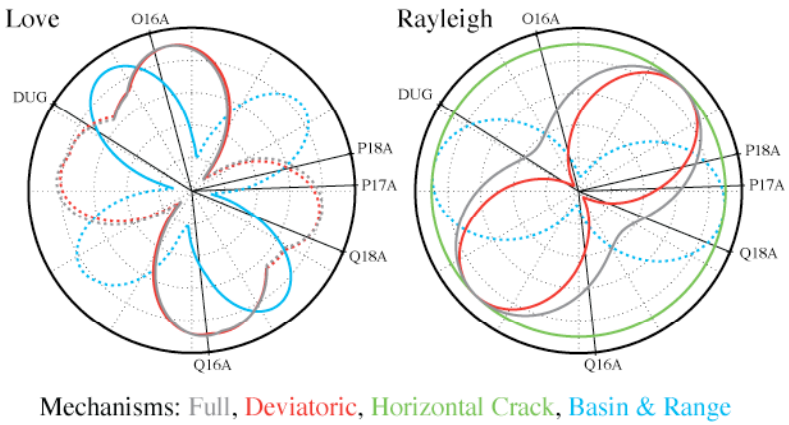


Figure 3.6. Radiation patterns of potential mechanisms. Polar plots where the radius is normalized to the maximum amplitude. The color of the pattern is related to the mechanism and the dashed or solid line represents positive and negative polarity for the maximum amplitude of a velocity trace at 300 km distance, respectively. There is no green pattern in the Love waves since the horizontal closing crack produces no SH energy along the horizontal. Stations are plotted at the appropriate azimuth.

crack. Contrary to the observations, this mechanism does not produce any Love waves. Finally, we test a typical 6 km deep Basin & Range normal mechanism that has the strike of the nearby Joe's Valley Fault, and where the $M_0$ is chosen to best fit the data. At some stations the waveforms predicted by this mechanism are completely out of phase with the data. This effect is easily seen when comparing the Love and Rayleigh wave radiation patterns predicted by these potential mechanisms as shown in Figure 3.6 for a distance of 300 km. The Basin & Range mechanism predicts Love waves that are of opposite polarity than that predicted for the full solution at DUG. The deviatoric solution predicts almost no Rayleigh waves at stations DUG and Q18A, and significant amplitude and phase mismatches of Rayleigh waves at other stations.

It is difficult to grasp the source-type from the standard focal mechanism plot. For example, one cannot discern the relative contributions of the isotropic and

deviatoric components from the full focal mechanism in Figure 3.2a. In addition, decompositions of the deviatoric component are non-unique (Julian et al., 1998), and will be discussed later. Following the source-type analysis described in Hudson et al. (1989), and as employed by Ford et al. (2007), we calculate $-2\varepsilon$ and $k$, which are given by

$$\varepsilon = \frac{-m_1'}{|m_3'|}.,\tag{3.1}$$

and

$$k = \frac{M_{\mathrm{ISO}}}{|M_{\mathrm{ISO}}| + |m_3'|}\ ,\tag{3.2}$$

where $m'_1$, $m'_2$ and $m'_3$ are the deviatoric principal moments for the T, N, and P axes, respectively, and $M_{\mathrm{ISO}} = \mathrm{trace}(M_{ij})/3$. $\varepsilon$ is a measure of the departure of the deviatoric component from a pure double-couple mechanism, and is 0 for a pure double-couple and ±0.5 for a pure compensated linear vector dipole (CLVD). $k$ is a measure of the volume change, where +1 would be a full explosion and −1 a full implosion. We calculate $-2\varepsilon$ and $k$ for the Crandall Canyon Mine and Tremonton events and present them on the source-type plot in Figure 3.7. The projection used in the source-type plot is designed so as to make the parameter variance linear for the moment tensor elements. The Crandall Canyon Mine event plots very near the point for a theoretical closing crack mechanism or anti-crack in a Poisson solid, which represents the process of collapse of an underground cavity (Pechmann et al., 1995; Bowers and Walter, 2002). The Tremonton event plots near the origin, which is consistent with a DC tectonic event. The source-type parameters from two past mine collapses in the Trona mine area of Wyoming and one explosion cavity collapse at the Nevada Test Site

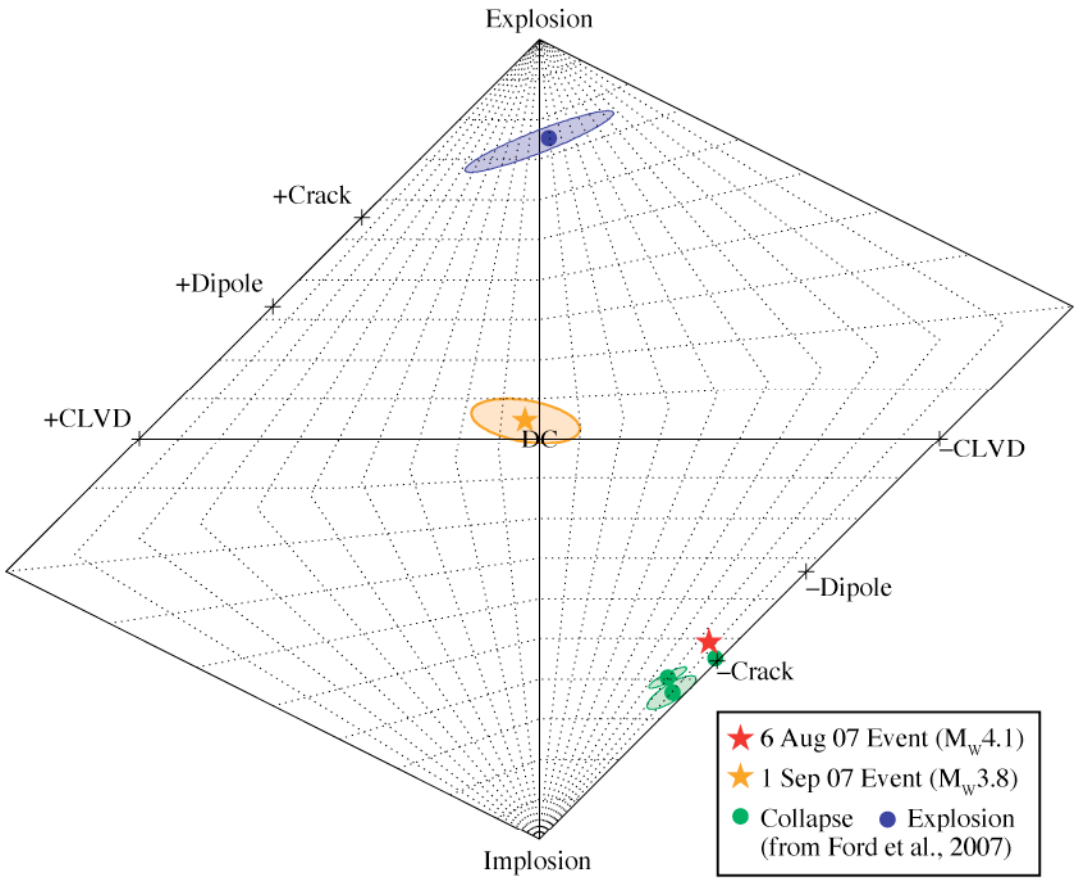


Figure 3.7. Source-type plot after Hudson et al. (1989). Theoretical mechanisms are plotted with crosses and annotated. The September 1, 2007 event near Tremonton (orange star) plots near the DC mechanism. The August 6, 2007 Crandall Canyon Mine event (red star) plots in the general moment tensor space that defines a closing crack, or collapse. The event is located well outside the region occupied by tectonic earthquakes and explosions, and is near other collapse mechanisms (two mine collapses and one explosion cavity collapse) calculated by Ford et al. (2007). 95% confidence regions are also given, where the region for the Crandall Canyon Mine event is so small as to not be visible outside the symbol.

(NTS) along with the NTS nuclear test explosion, BEXAR, are also given from the analysis of Ford et al. (2007) for comparison. The other collapse events are also located in the region of the plot near a pure closing crack and near the Crandall Canyon Mine event.

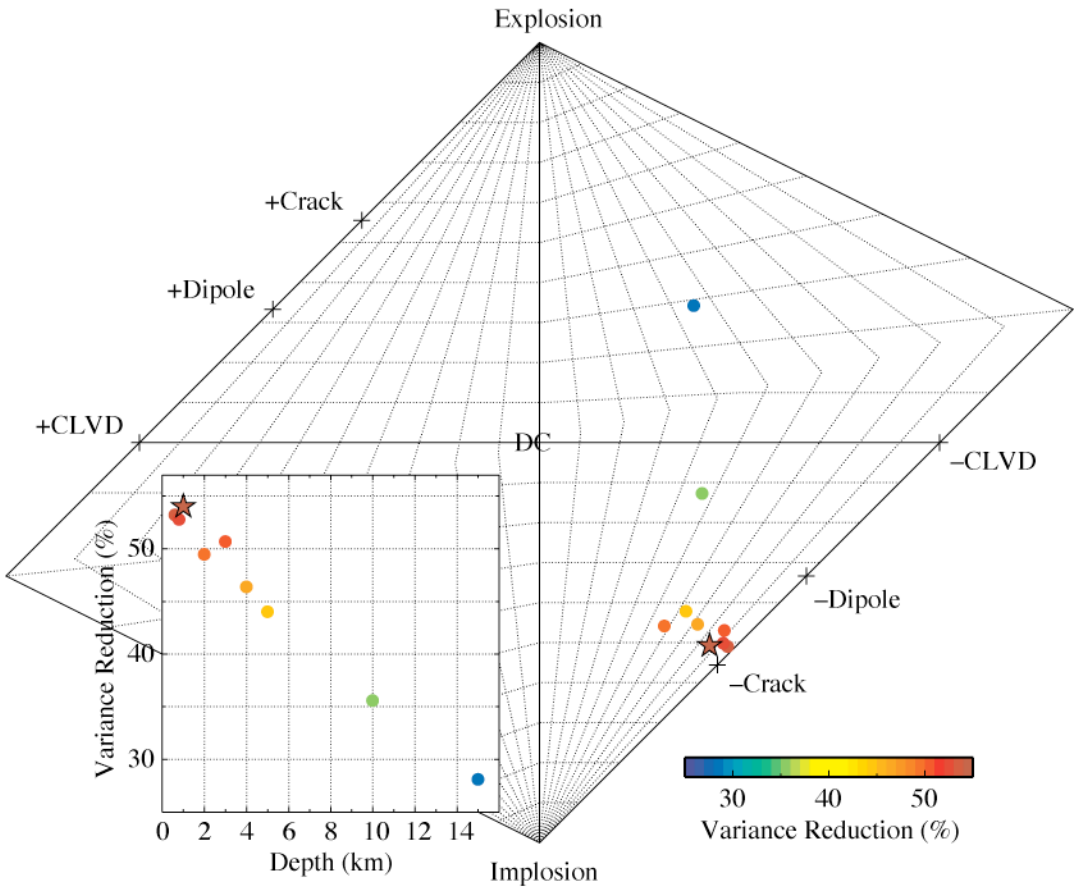


Figure 3.8. Source-type plot as a function of depth. Inset, variance reduction (VR) as a function of depth used to create the Green's functions. The color corresponds to VR and can be used to reference the depth from the inset plot. The star is the parameters given for a depth of 1 km.

### 3.3 Depth Sensitivity

Analysis of the sensitivity of the moment tensor solution to source depth indicates that shallow depths are preferred (Figure 3.8). In this analysis 16 stations were used and the data was processed as described above. Depths of 600m, 800m and 1 km gave similar levels of fit. The slight improvement in fit from 2 to 3 km depth is likely due to the presence of a velocity discontinuity in the structure modeled used to

compute the Green's functions (Table 2.2). The moment tensor solution remains stable and strongly crack-like over the depth range from 600 m to 5 km. Assumed sources at greater than 5 km depth become less crack-like, but remain substantially different from a double-couple.

### 3.4 Source Decomposition

Previous work modeling intermediate period (10-50s) seismic waveforms has shown the sudden collapse of underground cavities is well modeled using a vertically closing crack model (e.g., Pechmann et al., 1995; Bowers and Walter, 2002). For example the collapse of an approximately two square kilometer area of the Solvay trona mine in Wyoming on February 3, 1995 generated an $M_L$ 5.2 seismic event. Intermediate surface waves and short period first motion data were nicely fit using a closing tensile crack moment tensor, and were inconsistent with earthquake DC mechanisms (Pechmann et al, 1995). This 1995 event and a subsequent collapse event in 2000 are the green colored reference points near the closing (negative) crack location in Figure 3.7. For sources near the surface of the Earth one can show that a related model for cavity collapses: a block dropping vertically downward represented as vertical point forces (Taylor, 1994), produces basically the same waveforms as the closing crack model (Day and McLaughlin, 1991; Bowers and Walter, 2002).

The simple closing crack representation allows an estimate of the area of the mine collapse from the seismic data alone, analogous to the ability to estimate the

rupture area of a purely DC earthquake from its point source moment. In the case of the gravity driven, horizontally lying vertical closing crack, the moment is given by

$$M_{xx} = M_{yy} = -\lambda\, S\bar{u} \quad \text{and} \quad M_{zz} = -(\lambda + 2\mu)\, S\bar{u}\ , \tag{3.3}$$

where $\lambda$ and $\mu$ are Lame parameters, $S$ is the area of the crack and $\bar{u}$ is the average closure distance. Once we have a waveform based moment and an estimate of the average closure distance, we can seismically determine the collapse area.

The damaged region in the Crandall Canyon coal mine has a room and pillar configuration (www.msha.gov/Genwal/CrandallCanyon.asp), where parts of the coal seam are removed and portions are left as pillars to support the roof in a grid-like pattern. Typically room and pillar mines have an "extraction rate" for the percent of material removed. In a mine with 50% extraction the largest possible closure would be half the pillar height, if the mined material had the same density as the original seam after collapse. However, the pillar material will fracture and rubblize in the collapse (called the "swell"), so the actual closure distance will be less. For example in the February 3,1995 Wyoming mine collapse, which occurred in an approximately 60% extraction room and pillar section of a trona mine, the average closure distance determined from both the seismic moment and the surface subsidence was about 0.6 m (Pechmann et al, 1995). This distance was between one fourth and one fifth of the original pillar height of 2.8m.

In the case of the Crandall Canyon mine, Pechmann et al. (2008) estimated the extraction rate in the vicinity of the collapse to be between approximately 35 and 45%. They also give the pillar height as 2.4 m and estimate the coal to swell between 40 and 50%. Under the assumptions that pillars are entirely rubblized, such that any

remaining air space after collapse is accounted for by the swell, and the area under consideration does not change, we can derive a formula for the closure distance, $\bar{u}$, in terms of the original pillar height *h*, the extraction fraction *e*, and the swell fraction *s* as

$$\bar{u} = h\left[1-(1-e)(1+s)\right] . \tag{3.4}$$

This leads to estimates of the closure distance of 0.06 to 0.55 m. We can decompose the full moment tensor ($M_{\text{full}}$) for the Crandall Canyon Mine event into the simple gravity driven collapse model (represented as a horizontal closing crack; $M_{\text{crack}}$) plus smaller secondary components contained in a remainder moment tensor ($M_{\text{rem}}$), or

$$M_{\text{full}} = M_{\text{crack}} + M_{\text{rem}} . \tag{3.5}$$

We estimate the Lame parameters from the velocity model used to calculate the Green's functions for the inversion so that $\lambda = 1.0\text{x}10^{10}$ Pa. In this case the Poisson's ratio ($v$) is 0.26 and the $M_{\text{crack}}$ moment ratio is [1:1:2.85]. The moment associated with the volume change ($S\bar{u}$) is selected so as to remove the isotropic component in $M_{\text{rem}}$, which is to say that all volumetric change is due to the collapse. In matrix form (5) becomes

$$\begin{bmatrix} -55.24 & -10.51 & 20.51 \\ -10.51 & -54.16 & 26.55 \\ 20.51 & 26.55 & -182.50 \end{bmatrix} = \begin{bmatrix} -60.25 & 0 & 0 \\ 0 & -60.25 & 0 \\ 0 & 0 & -171.40 \end{bmatrix} + \begin{bmatrix} 5.01 & -10.51 & 20.51 \\ -10.51 & 6.09 & 26.55 \\ 20.51 & 26.55 & -11.10 \end{bmatrix}, \tag{3.6}$$

where each moment is in units of $10^{-5}$ Ak ($10^{13}$ N-m). In this case $M_{\text{rem}}$ and $M_{\text{crack}}$ are $4.16\text{x}10^{14}$ and $1.71\text{x}10^{15}$ N-m, each obtained by taking the maximum eigenvalue of each moment tensor (e.g. Bowers and Hudson, 1999). $M_{\text{rem}}$ represents 20% of the sum of these two moments ($2.13\text{x}10^{15}$ N-m). The total scalar moment of the full tensor, $M_{\text{full}}$ as defined by Bowers and Hudson (1999), is $1.91\text{x}10^{15}$ N-m. The total scalar

moment is not preserved when the tensor is decomposed into two or more parts with deviatoric components. In this case the small difference in the scalar moment estimates is due to the decomposition of $M_{\text{full}}$ to a $M_{\text{crack}}$, which has both isotropic and deviatoric components, and a fully deviatoric $M_{\text{rem}}$. In this decomposition the only invariant is the isotropic component. We feel this decomposition is justified based on physical considerations. The closing crack $M_{xx}$ moment tensor component is $6.03 \times 10^{14}$ N-m. Using the range 0.06 to 0.55 m for the closure distance, we estimate the collapse area to be about 1.1 to 10.0 $\times 10^5$ $m^2$. If square, this area would be approximately 330 to 1000 m on a side. Small closure distances lead to unrealistically large collapse areas, so we favor solutions near the larger closure distance and the smaller collapse area.

As can be seen in Figure 3.3, there is substantial Love wave energy at all stations, which cannot be produced from a purely gravity-driven closing crack as analyzed above. We investigate the source of this anomalous energy through an exercise in non-unique decompositions in the form of (3.5), where we remove the pure collapse mechanism and examine the remainder. We try two different types of decompositions, the first using the remainder as given in (3.6) and a second decomposition where we allow the $v$ to vary.

We test two non-unique decompositions of the remainder, $M_{\text{rem}}$ given by (3.6). The first decomposition splits $M_{\text{rem}}$ into a DC and CLVD mechanism that share the same P and T axes as shown in Figure 3.9a. This results in a small DC component and a large CLVD component where the largest principal moment is 73% of the largest principal moment of $M_{\text{rem}}$. We note that Fletcher and McGarr (2005) present full

moment tensor results for 6 small (1.3<M<1.8) mining-induced seismic events in the Trail Mt. region of Utah about 15 km south of the Crandall Canyon Mine event. Decomposition of those events in the same manner (using a horizontal crack that leaves no isotropic remainder with a Poisson ratio ($v$=0.25) defined by their Green's function velocity model parameters) also produces significant non-DC components. If

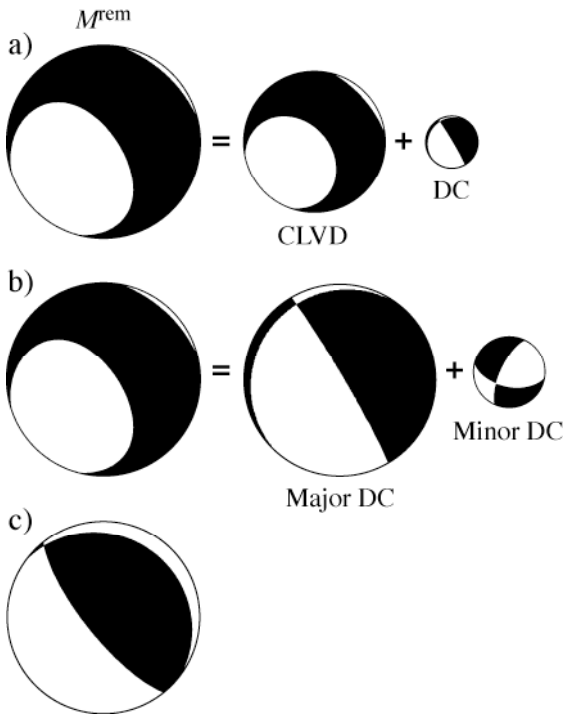


Figure 3.9. Moment tensor decomposition where the diameter of the lower hemisphere projection is relative to the largest principal moment. a) The remainder mechanism ($M_{rem}$) after subtraction of a horizontal crack that leaves no isotropic component and where the Poisson's ratio is given by the velocity model used to calculate the full moment tensor is decomposed to a CLVD and DC with the same T and P axes. The azimuth and plunge of the major vector dipole in the CLVD are 229° and 48°, respectively. b) The same remainder as in a) is decomposed to a major and minor DC. Source parameters of the major DC are strike = 329°, rake = –100°, and dip = 86°. c) The remainder mechanism after subtraction of a horizontal crack that leaves no isotropic component and with a Poisson's ratio that gives a full DC remainder. Source parameters are strike = 306°, rake = 76°, and dip = 16°.

one assumes a remainder split into DC and CLVD that share the P and T axes, then half of the Fletcher and McGarr (2005) events also have a majority CLVD component in the remainder.

The same $M_{\text{rem}}$ from (3.6) can also be decomposed to a major and minor DC as shown in Figure 3.9b. In this case the largest principal moment of the major DC is the largest principal moment of $M_{\text{rem}}$, and the largest principal moment of the minor DC is the smallest principal moment of $M_{\text{rem}}$, so that the moment of the minor DC is 36% of the major DC. This decomposition produces mechanisms with different T and P axes. Interpretations of these non-unique decompositions are themselves non-unique. A simplistic and speculative possibility in the case of the large CLVD remainder could be that it is associated with non-volumetric redistribution of material within the mine following the collapse, or additional elastic relaxation near the mine due to non-uniform stress. In the major DC remainder case (Figure 3.9b) an interpretation might be that the collapse was uneven so that portions of the closure were accommodated by a large nearly vertical block motion on one side of the collapse. Alternatively the large DC remainder could represent shear between the floor and roof of the cavity. In both cases we might assume the smallest DC remainder could simply come from noise in the data and errors in the Green function compared to the true Earth structure.

The second type of decomposition allows the Poisson ratio and volume change to vary so that $M_{\text{rem}}$ is purely DC. This occurs when $\nu = 0.18$ giving a $M_{\text{crack}}$ moment ratio [1:1:4.56] so that (3.4) is given by

$$\begin{bmatrix} -55.24 & -10.51 & 20.51 \\ -10.51 & -54.16 & 26.55 \\ 20.51 & 26.55 & -182.50 \end{bmatrix} = \begin{bmatrix} -44.53 & 0 & 0 \\ 0 & -44.53 & 0 \\ 0 & 0 & -202.85 \end{bmatrix} + \begin{bmatrix} -10.71 & -10.51 & 20.51 \\ -10.51 & -9.63 & 26.55 \\ 20.51 & 26.55 & 20.35 \end{bmatrix}., \quad (3.7)$$

where each moment is in units of $10^{-5}$ Ak ($10^{13}$ N-m). In this case $M_{rem}$ represents only 21% of the total moment in $M_{full}$, and the closing crack $M_{xx}$ moment tensor component is 4.45x$10^{14}$ N-m. If we assume that $\lambda$ and $\bar{u}$ are the same, the collapse area is approximately 280 to 860 m on a side and $M_{rem}$ would be given by Figure 3.9c. It is interesting to note that the $M_{rem}$ mechanism in this decomposition is the same as the deviatoric inversion results shown in Figure 3.5. As we discussed in the previous case with the DC remainder this mechanism could be consistent with an uneven collapse of the cavity accommodated by normal mechanism style block motion above part of the cavity. This could be related to asymmetric in-situ stresses in the region from a variety of possible sources such as topography, tectonic forces and mining-related changes. Finally we note that the second decomposition gives a low Poisson ratio that is inconsistent with the velocity model used in the inversion or with the intact coal or sedimentary rocks in the region. Recalculation of the moment tensor using a velocity model with a 500 m strip at the source depth of decreased $V_\alpha$ that is consistent with the inferred *v* does not result in a decomposition similar to (7). Therefore, a speculative interpretation would be that the low Poisson ratio is a local effect related to the damaged rock in the immediate region of the mine collapse. Another explanation of the greater vertical to horizontal moment ratio than specified by the Green's functions is that it is a manifestation of over-closure of the crack due to inelastic accommodation afforded by a secondary vertical dip-slip source. The conjugate fault of the DC given by $M_{rem}$ in (7) and shown in Figure 3.9c (strike = 303°, rake = 73°, dip = 16°) suggests another alternate scenario, which is differential shear between the roof and floor of the mine along a southwesterly trajectory.

The decompositions discussed in this section are non-unique and the interpretations associated with them are speculative. Our intent here was to cover the range of possibilities for the secondary source. However one should not lose sight of the fact that the primary and dominant source for this event is a closing crack mechanism (78 and 79% of the total moment for the two decomposition types), which is consistent with the observed collapse in the mine and with that observed in previous large cavity collapse seismic events in the Western U.S. (e.g., Taylor et al 1994; Pechmann et al.; 1995, Bowers and Walter, 2002). As the comparison with the September 1, 2007 Tremonton earthquake and many other western U.S. earthquakes analyzed in Ford et al. (2007) show, the Crandall Canyon Mine event is not consistent with a tectonic earthquake. The cause of the significant secondary shear source associated with this event remains poorly understood and perhaps differentiates this mine collapse from some of the previous ones analyzed. Significant work remains to be done to reconcile the collapse area implied by the seismic event and the causes of the secondary shear source with the details of what occurred in the mine itself and warrant further investigation that is beyond the scope of this paper.

## 3.5 Conclusions

The source characteristics of the local magnitude 3.9 Crandall Canyon Mine event that occurred in central Utah on August 6, 2007 are significantly different from the similar size earthquake that occurred near Tremonton, Utah on September 1, 2007. Full moment tensor analysis shows the Crandall Canyon Mine event is most consistent

with previous shallow cavity collapse events that have a closing crack mechanism, and is quite different from typical tectonic earthquakes at depths of 5-15 km. This interpretation is robust to small errors in the source depth, and a non-DC mechanism is retrieved at all depths. Mechanisms that have no volume-change and typical Basin & Range normal focal mechanism do not fit the observed waveforms. However, a purely vertically closing, horizontally lying crack cannot explain the large Love wave observations, and an additional shear mechanism is needed to fully explain the observed waveforms. Such a mechanism could be explained by an asymmetric collapse of the mine cavity due to unevenly distributed in-situ stresses, sympathetic shear on a roof fault, or between the roof and floor of the mine, and warrants further investigation.

### 3.6 Field Investigation

As discussed in section 3.4 and shown by Figure 3.9, the preferred source for the Crandall Canyon event on 6 Aug 07 (Figure 3.10) had a component of shear that could be explained by a near vertical slip plane oriented approximately N-S with the east side down. There are a few interpretations of this mechanism. It could be that the source is a break in the mine roof along the edge of the collapse zone. Collapses above mined-out coal seams propagate to the surface along deformation zones dipping 70-80 degrees (Sileny and Milev, 2006; K. McCarter, 2007, pers. comm.). Other scenarios are that the faulting occurred in the nearby Joe's Valley Fault, but then it would probably need to be deeper and further west than the mine collapse. Furthermore the uppermost 2-4 km of fault zones is thought to be too soft to store elastic strain energy, based in part on studies of aftershock distributions. Finally, most normal faults don't have near-vertical dips, except in the unconsolidated sediments near the surface (J. Pechmann, 2007, pers. comm.), and the sense of slip of the inferred mechanism from the moment tensor remainder is inconsistent with the expected motion on the Joe's Valley fault. Another possibility is that the mine roof moved horizontally to the north-northeast. While there is some mention of roof deformation in the Mine Safety & Health Administration (MSHA) report it was not pervasive enough, nor was there other evidence that suggests large scale horizontal movement of the mine roof.

We actively discussed these scenarios while presenting our research at the 19th IRIS Workshop, which was held 4-6 Jun 08 in Stevenson, Washington. To try to distinguish between these different possibilities for the deviatoric remainder in the

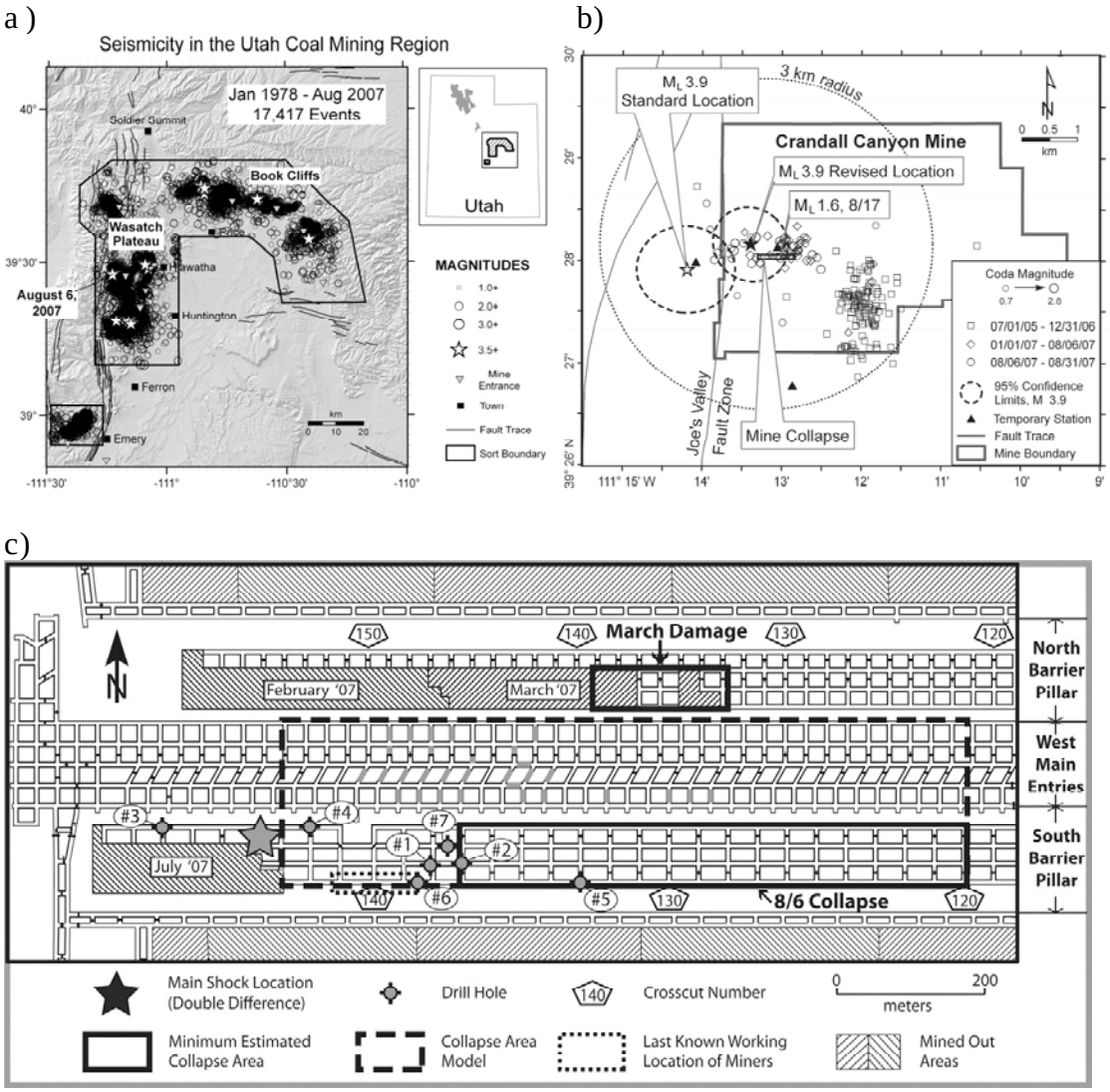


Figure 3.10. a) Epicenter map of seismicity within polygons outlining the Wasatch Plateau-Book Cliffs coal-mining region of Utah (black polygons) from January 1978 through August 2007. b) Map of the Crandall Canyon Mine area showing the epicenter of the 6 August 2007 ML 3.9. The crosshatched box shows the minimum estimated area of the 6 August Crandall Canyon Mine collapse shown in c). c) Map showing the west mains section of the Crandall Canyon Mine where the 6 August 2007 collapse occurred. The dashed box shows a collapse area model that is more consistent with the seismological data, including our best location for the main shock (star). Reproduced from Pechmann et al. (2008).

moment tensor solution we decided to look for evidence of faulting on the ground above the collapsed portion of the mine. We planned a reconnaissance trip with Jim

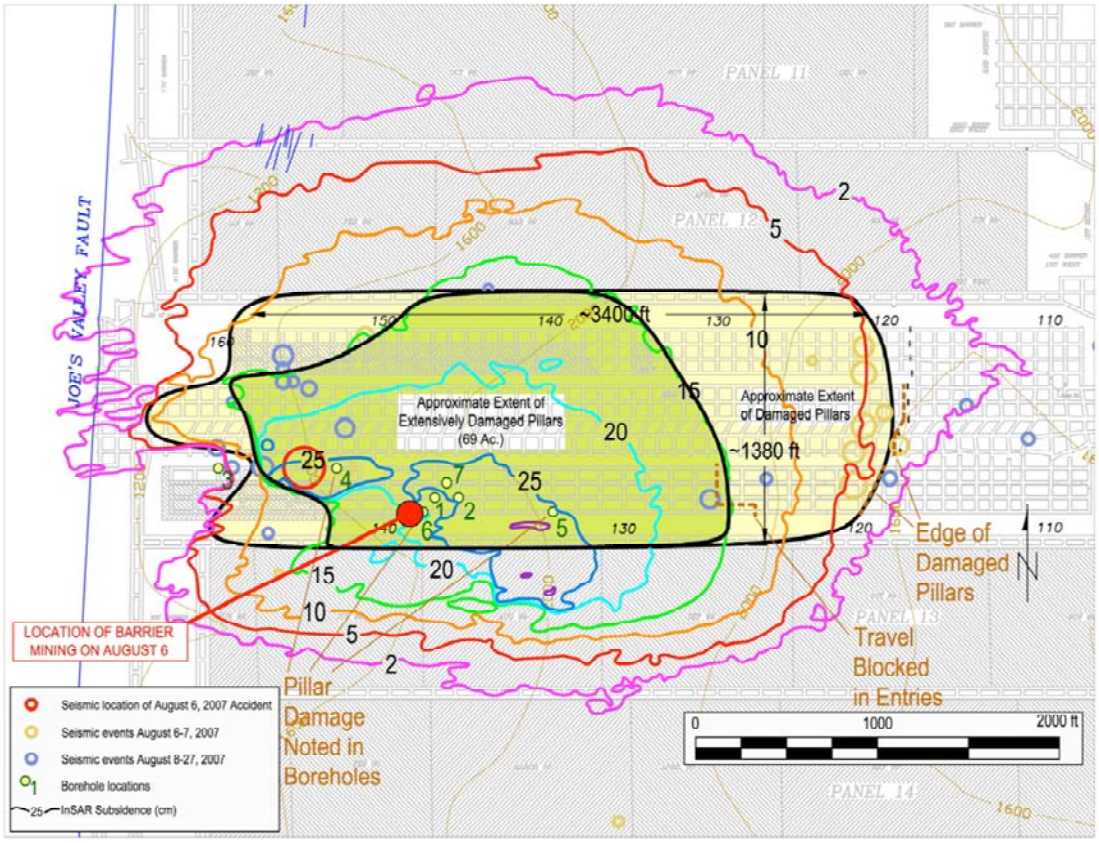


Figure 3.11. superimposes a variety of data used to determine the extent of the collapse, including: the seismic data from the time of the August 6 accident to August 27, 2007, the borehole locations, the InSAR subsidence contours, and the likely extent of damaged pillars. The eastern boundary of the pillar failures was based on the underground observations and InSAR subsidence data and is consistent with residual seismic activity. The western edge of the pillar failures was based on the borehole observations and InSAR subsidence data and is consistent with the seismic location of the accident and the additional seismicity later in August 2007.

Pechmann at the University of Utah Seismograph Station for 25 - 30 Jul 08. A week before we left the MSHA fatal accident report was released and we were greatly encouraged by InSAR results reported therein (Figure 3.11), which showed areas of up to 25 cm of subsidence near the collapse site. In the days after the 6 Aug 07 accident MSHA begin drilling boreholes to assess the oxygen levels and look for signs of life from the trapped miners. On 16 Aug 07 a pillar burst fatally injuring three of the

a)

b)

c)

d)

Figure 3.12. a) View from Borehole 3 looking Southwest. b) View of mountain from road looking East (black and white arrows in Figure 3). c) Signs of recent subsidence elsewhere at the site. d) Forest view.

rescue workers digging through the collapse rubble from the east toward the last know location of the miners at the west end of the collapse section. Following this accident efforts were directed toward drilling boreholes (MSHA Report). The boreholes were concentrated initially near the last known location of the miners ("location of barrier mining on August 6" in Figure 3.11), but continued down the mountain toward the west. A photo of borehole 3 is shown in Figure 3.12a, and this borehole showed the

mine to be open. All of the other boreholes shown in Figure 3.11 indicated that the mine had collapsed in those locations.

We only had two days at the site and the plan for the first day was to start from the road (dashed line, Figure 3.13) and ascend to borehole 3 and then use the roads and drill pads built for the borehole equipment that had yet to be reclaimed. This plan seemed good on paper, but when we arrived at the site, the treacherousness of the path became apparent as can be seen in Figure 3.12b (shown as an arrow in Figure 3.13). The field party of Jim Pechmann, Judy Pechmann, Doug Dreger, and the author managed to climb the incline while encountering a nearly vertical sandstone outcrop (member of the Price River formation). We then surveyed the area for signs of subsidence (Figure 3.12c) where our tracks are plotted in Figure 3.13. We concentrated on the region between boreholes 3 and 4 (Figure 3.13) because this encircled the region of the epicenter and the collapsed (borehole 4) versus uncollapsed (borehole 3) section of the mine as shown by the InSAR and by the borehole observations. It was very difficult to see the forest floor due to all the vegetation (this had been the wettest Spring in recent memory) and all agreed that even if there were small signs of subsidence it could have gone unnoticed beyond ± 3 m of the paths.

The location that drew most of our attention was a sandstone outcrop very near borehole 4 (Figure 3.14). The sandstone was very blocky with nearly-vertical joints striking approximately N10°W. This joint set is pervasive in the units above the mine (MSHA report). There was no sign of obvious recent deformation, but there were certainly signs of 10s of cm of motion in the geologic past (Figure 3.14, inset). The inset of Figure 3.14 shows an open joint with the eastside down, which is consistent

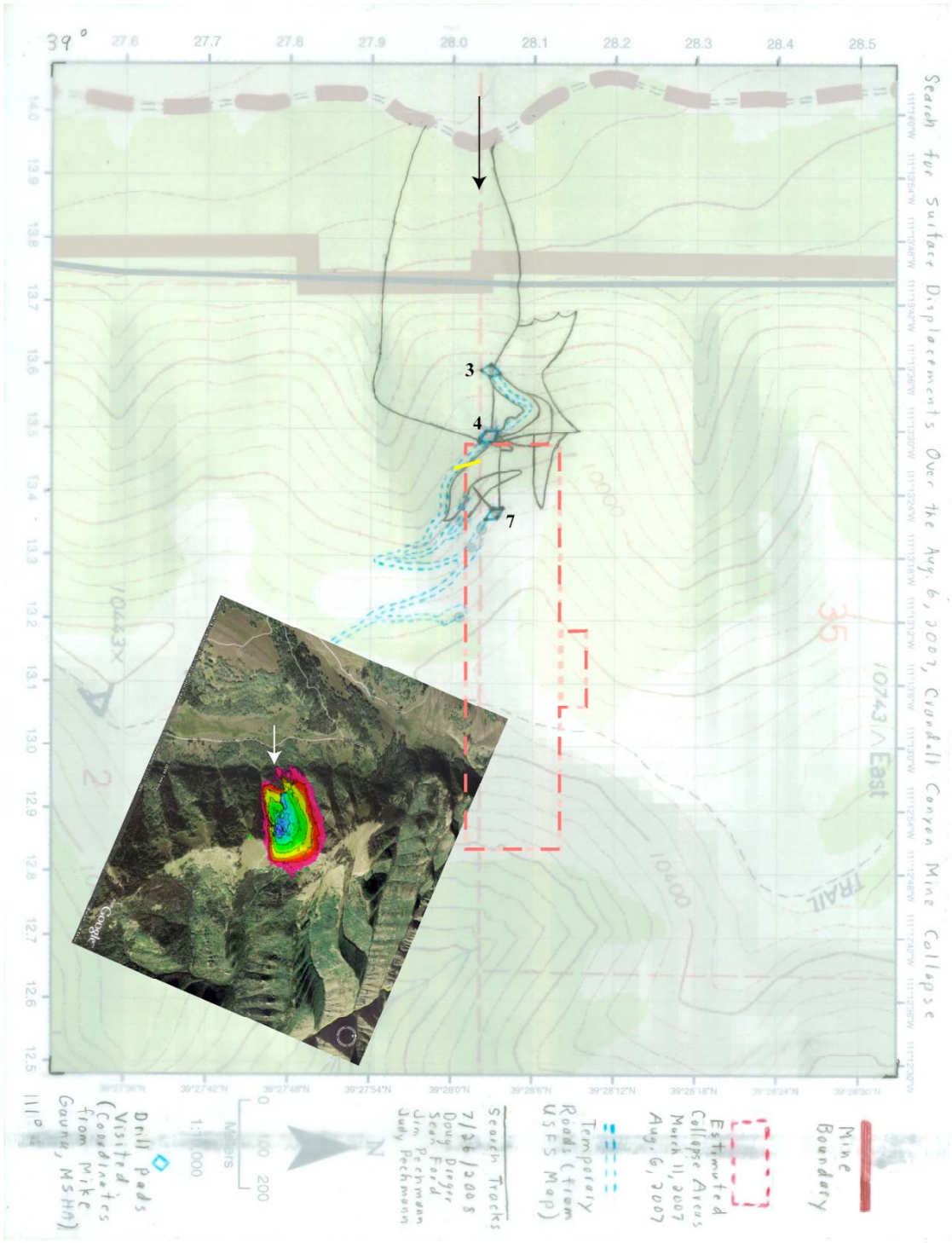


Figure 3.13. Crandall Canyon Mine collapse area (dashed red outline) with survey tracks (black lines). The arrows show the location and direction of the photo in Figure 3.12a as well as orient the map and inset with InSAR contours superimposed. Visited boreholes are numbered and the location of the outcrop of interest (Figure 3.14) is in yellow.

with the double-couple inferred from the moment tensor remainder. The surface of the joint was fresh white in color, which distinguished it from older joints which showed hematite staining. This joint is located close to the road that was graded for the rescue effort, and we could not deny that the open joint was due to the grading work. The arrows in Figure 3.14 highlight another joint that shows a discontinuous shalely unity with possibly as much as 30 cm of offset with the eastside down. This deformation does not appear to be recent. This joint and the previous one discussed are within an approximately 2m wide zone of more densely concentrated vertical joints and horizontal fractures with cantilevered blocks in the formation. Outside of this zone, either to the southeast or northwest the joint density appreciably reduced. This concentrated jointing and the apparent offset indicates fauting in the geologic past. While this zone had the sense of motion consistent with the moment tensor there was no evidence that the deformations at the outcrop or on the ground above the outcrop that could be attributed to recent moment. However, if this network of joints continues at depth, then its possible that this pre-existing fabric could have allowed sympathetic shear along its face, thereby producing a mechanism consistent with the secondary shear mechanism from our inversion.

The next day we approached the site from the top of the ridge (dashed dark line, Figure 3.13) with a Forest Service Ranger, Tom Lloyd. His expertise was very valuable as not only was he around during the construction of the boreholes and knew the area well, he had also been a mine geology engineer in the region. We found no other signs of subsidence, despite being better informed as to its effects when Tom

Figure 3.14. Massive fractured sandstone block at collapse site. Yellow line in Figure 3.13 shows location of this photo and strike of joints. Inset is blow-up of feature in white box. Arrow points to vertical joint with the discontinuous and apparently offset shaley unit. Author's advisor shown for scale.

Lloyd showed us subsidence that had occurred in 2002 and been monitored since. The location of this subsidence is off the mapped area in the figures. We traversed the graded road from the summit back to the outcrop near borehole 4 and Tom Lloyd remarked on the change in joint density at the location, but remarked that no faults had ever been mapped in the region of the mine east of the Joes's Valley fault.

The roadcuts made to haul the borehole equipment were several meters deep, and it is possible that this anthropogenic deformation is the cause of the steep gradient in the InSAR deformation contours. Future work may try to model such an effect. Also, LIDAR has the ability to map the surface even with vegetation cover, so such an effort may be worthwhile to completely survey the area. Of course, any anomalies would have to be confirmed with field observation.

# Chapter 4

# Network sensitivity solutions for regional moment tensor inversions

## 4.1 Introduction

In chapter three we calculated seismic moment tensors for 17 nuclear test explosions, 12 earthquakes, and 3 collapses in the vicinity of the Nevada Test Site in the Western US. We found that the relative amount of isotropic and deviatoric moment provided a good discriminant between the explosions and earthquakes. The observational work to describe the discriminant was accompanied by a theoretical study into the sensitivities of the method and it was found that the ability to resolve a well-constrained solution is dependent on station configuration, data bandwidth, and signal-to-noise ratio (SNR). It is difficult to state steadfast rules for what source-types can be resolved for all conditions, when different conditions lead to different levels of confidence in the solution. Therefore, in this study we develop event-specific confidence analyses, which we call the network sensitivity solution (NSS).

There have been many attempts to understand error in seismic moment tensor inversions. Sileny and coathors have done extensive sensitivity testing of the methods they use to calculate the moment tensor. Sileny et al. (1992; 1994), Sileny (1998), Jechumtalova and Sileny (2001), Sileny and Vavrycuk (2002), and Sileny (2004) have collectively investigated the effects of incorrect event depth, poor knowledge of the

structural model including anisotropy, noise, and station configuration on the retrieved solution. They found that for only a few stations with data of SNR>5 the moments of various components were sensitive to improper source depth and velocity model, but that the mechanism remained robust, and that spurious isotropic components may manifest in the solution if an isotropic medium assumption is made incorrectly. Roessler et al. (2007) confirm this last result. The probabilistic inversion method by Weber (2006) using near-field full-waveform data helped to inspire the approach taken in this study. Weber (2006) inverts for hundreds of sources using a distribution of hypocentral locations based on *a priori* information. Perturbations to the velocity model and noise are also added in the synthetic portion of the study. Empirical parameter distributions are then produced to assess the resolution. Mechanism distribution is plotted with a Riedesel and Jordan (1989) plot, which is also the preference of many of the previously mentioned studies. In the following study we will employ the source-type plot from Hudson et al. (1989), which is described in Ford et al. (2009). Further details of the inversion method and its practical implementation are also given in Ford et al. (2009).

## 4.2 Data and Method

The network sensitivity solution is first performed for the nuclear test, JUNCTION, which took place at the Nevada Test Site (NTS) and was analyzed in Ford et al. (2008). Three-component data was collected from a total of six stations from the Berkeley Digital Seismic Network, Trinet, and the Lawrence Livermore

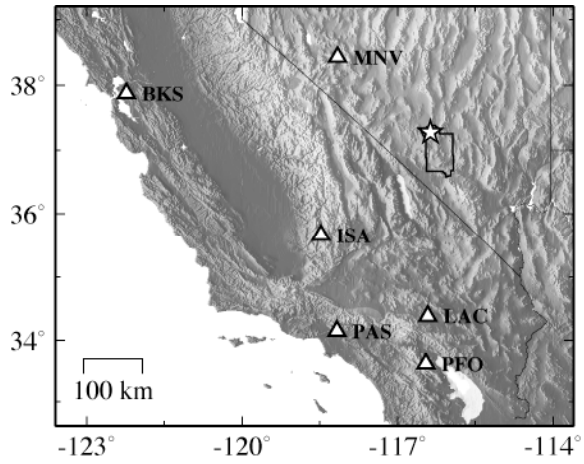


Figure 4.1. Map of the Western US with the Nevada Test Site (NTS) outlined and the NTS test, JUNCTION (star). Stations used in the analysis are also shown (triangles) with their names.

National Laboratory (LLNL) network (Figure 4.1). All data is freely available from IRIS and the NCEDC via the internet except the LLNL historic network data, which is available on compact disk (Walter et al., 2004). We remove the instrument response, rotate to the great-circle frame, integrate to obtain displacement, and filter the data with a 4-pole acausal Butterworth filter with a low-corner of 50 sec and a high-corner of 20 sec, except for the LLNL network (composed of Sprengnether instruments with limited long-period response), which is filtered between 10 and 30 sec. The full-waveform regional data is inverted in the time-domain for the complete moment tensor as described in Minson and Dreger (2008). The Green's functions (GFs) used in the inversion are for a one-dimensional (1-D) velocity model of eastern California and western Nevada (Song et al., 1996) where the source is at 1km depth. We use these GFs to produce two types of NSSs, a theoretical NSS and an actual NSS. The theoretical NSS tries to answer the question of how well a pure explosion can be

resolved with very high signal-to-noise ratio (SNR) data for the given event scenario (i.e., data bandwidth and station distribution). To do this we use the GFs to first produce data for a model explosion as well as a uniform distribution of synthetic sources representing all possible sources, where the moment of these sources is chosen so as to best fit the model explosion data. The model explosion data *d* is then compared with the synthetic source data *s* and the fit for each comparison is quantified by the variance reduction VR

$$\mathrm{VR} = \left[1 - \frac{\sum_i (d_i - s_i)^2}{\sum_i d_i^2}\right] \times 100 \,. \qquad (4.1)$$

where *i* are the displacements at all times for all components at all stations. The synthetic solutions and their corresponding VR are then plotted as empirical distributions on the source-type plot (Hudson et al. 1989) as in Figure 4.2a. The actual NSS tries to find what source can be reliably resolved for the given event scenario. The actually recorded data is used in place of the model explosion data, which is compared with the same dataset of all possible sources to produce empirical VR distributions on the source-type plot as in Figure 4.2b.

The 9 Oct 06 North Korea nuclear test and a nearby earthquake that occurred on 16 Dec 04 is also analyzed with records of four stations that recorded the events well in the period band of interest (Figure 4.3). The same data processing steps are followed as previously described except that the data for three of the stations (INCN, TJN, and BJT) are filtered between 15 and 30 sec and data from station MDJ is filtered between 15 and 50 sec in order to increase the SNR. The GFs for these events

a) Theoretical explosion (JUNCTION GFs)

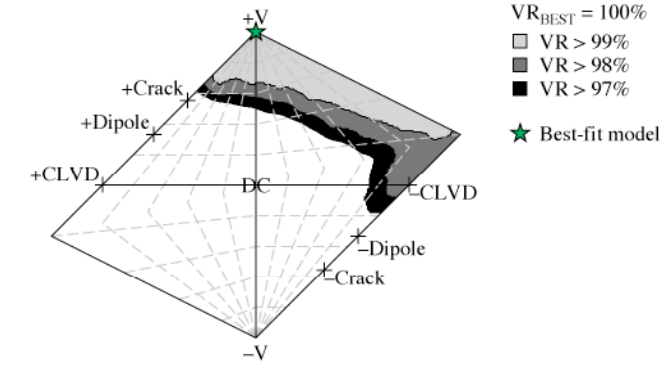


b) JUNCTION Data

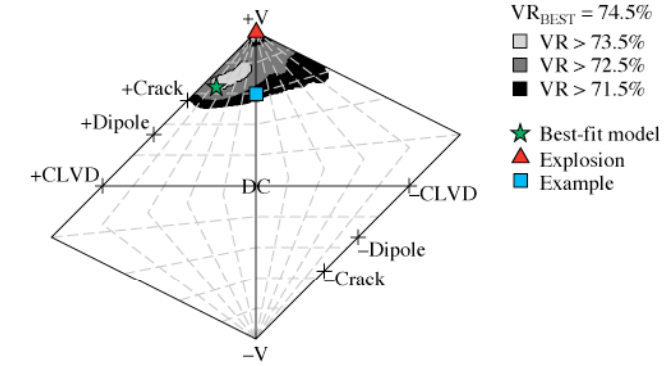


c) Models and waveforms

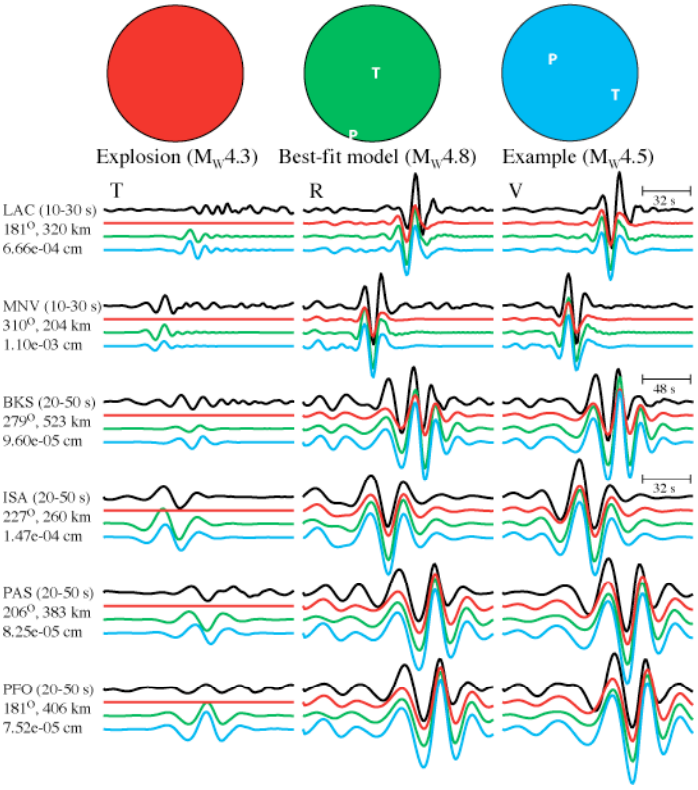

Figure 4.2 (previous page). Network sensitivity solution (NSS) for the NTS nuclear test, JUNCTION (26 Mar 92). a) Theoretical NSS for an explosion where the Green's functions are derived from the actual JUNCTION network setup and there is no noise in the data. The best-fit model is an explosion with a Variance Reduction (VR) of 100% (star). Empirical distributions of other models and the corresponding VR are also given on the source-type plot. b) Actual NSS using data from JUNCTION test. The best-fit model with a VR of 74.5% (star) along with other models and the corresponding VR distributions are shown. For comparison, an explosion and a poorly-fitting model with the least explosive component are also plotted and correspond with the models and waveforms given in c). c) Models corresponding to those plotted in b) and their respective forward-predicted waveforms as a function of color compared with the actual waveforms (black line). The left, middle, and right columns are the tangential (T), radial (R), and vertical (V) displacement waveforms, respectively. The text block to the left of the waveforms gives the station name, passband, azimuth, epicentral distance (km), and maximum displacement (cm).

are derived from the MDJ2 velocity model (Table 1). Also, for the earthquake theoretical NSS instead of an explosion a uniform distribution of all possible DCs is used as the model data. The theoretical NSSs for the earthquake and explosion are shown in Figures 4.4a and 4.5a, respectively, and the actual NSSs are shown in Figures 4b and 5b, respectively.

We also test applicability of the GFs derived from the chosen velocity model, MDJ2, in the case of the N. Korea test analysis. This is done by using several hundred velocity models from study by Pasyanos et al (2004) which uses a Markov-chain Monte Carlo method to create a suite of acceptable 1-D velocity models. We take several hundred of these models in the location beneath the source and perform an inversion using the GFs derived from each velocity model. The results are given in Figure 4.6 and will be discussed at the end of the next section.

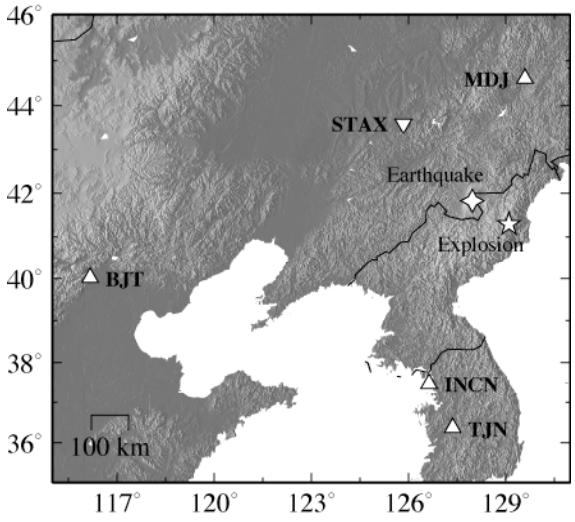


Figure 4.3. Map of the Yellow Sea / Korean Peninsula with the North Korea test (5-point star) and nearby earthquake (4-point star) as well as the stations used in this study (cyan triangles) and a synthetic station (STAX) used in the sensitivity analysis (inverted triangle).

### 4.3 Discussion

The theoretical NSS can aid in the understanding of the potential of a given event scenario to constrain a particular source at a chosen level of fit. In the case of JUNCTION the best fit (VR = 100%) is a purely isotropic source (star, Figure 4.2a), as expected, but the theoretical NSS can also show how well other sources fit the model explosion data. With only a 2% decrease in VR, a purely –CLVD fits the data well, demonstrating that a shallow –CLVD at these low frequencies recorded at regional distances effectively mimics the radiation pattern of an explosion (Taylor et al., 1991). However, the region of high VR (>97%) in Figure 4.2a is well separated from a DC source. Another advantage to this type of error analysis is that

a) Theoretical earthquake (China EQ GFs)

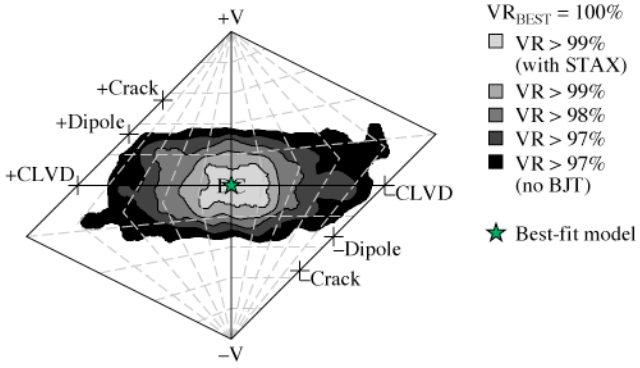


b) China EQ Data

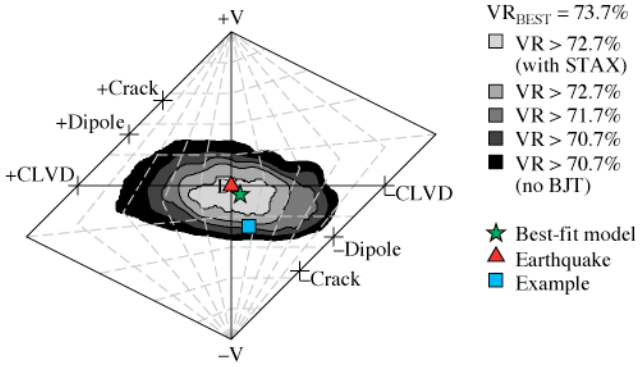


c) Models and waveforms

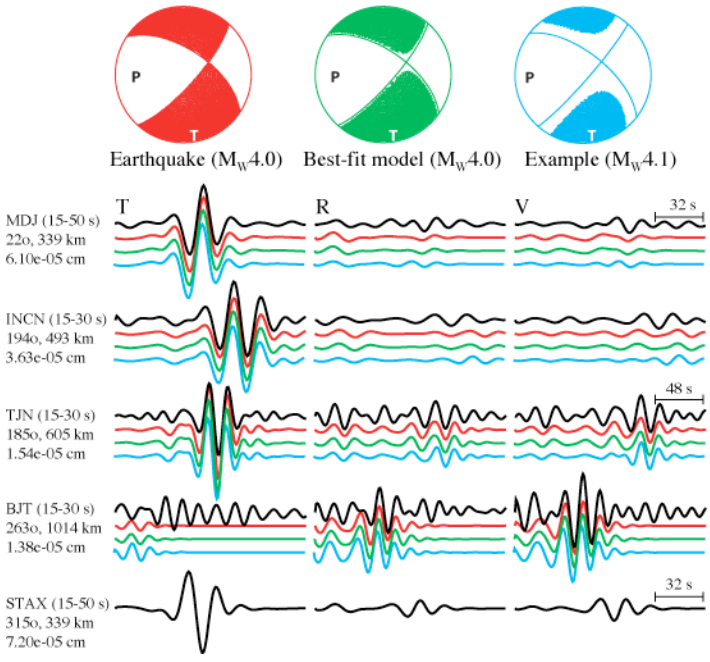

Figure 4.4 (previous page). Network sensitivity solution (NSS) for an earthquake (16 Dec 04) in near the North Korea test location. a) Theoretical NSS using one hundred earthquakes with a uniform distribution of fault parameters where the Green's function are derived from the actual network setup and the data is noiseless. The best-fit model is a pure double-couple (DC) with a VR of 100% (green star). Empirical distributions of other models and the corresponding VR are also given on the source-type plot. The distributions are also given for solutions where station BJT is not used in the inversion (black) and where the theoretical station STAX is used in the in the inversion (light gray). b) Actual NSS using data from the China earthquake. The best-fit model with a VR of 73.7% (star) along with other models and the corresponding VR distributions are shown. For comparison, an explosion and a poorly-fitting model with the largest volumetric component are also plotted and correspond with the models and waveforms given in c). c) Models corresponding to those plotted in b) and their respective forward-predicted waveforms as a function of color compared with the actual waveforms (black line). The left, middle, and right columns are the tangential (T), radial (R), and vertical (V) displacement waveforms, respectively. The text block to the left of the waveforms gives the station name, passband, azimuth, epicentral distance (km), and maximum displacement (cm).

one can define what 'high VR' means. In all cases we show VR regions that are 1, 2, and 3% less than the best-fit VR.

The actual NSS gives an idea of what sources can be resolved based on the true SNR. In the case of JUNCTION the high VR region encompasses a smaller area than the theoretical case, and an explosion source is even better constrained. To get an idea of why this difference may be, and what types of sources are contained in the high VR region it is helpful to view the waveforms from the synthetic and actual sources. Figure 4.2c shows the data compared with three sources, a pure explosion (triangle, Figure 4.2b), the best-fit model (star, Figure 4.2b, where VR = 75.5%), and an example from the VR>71.5% population (square, Figure 4.2b). Unlike the pure explosion case, the data has signal on the tangential component. This energy cannot be fit well with –CLVD sources so they are not represented in the VR>71.5% population

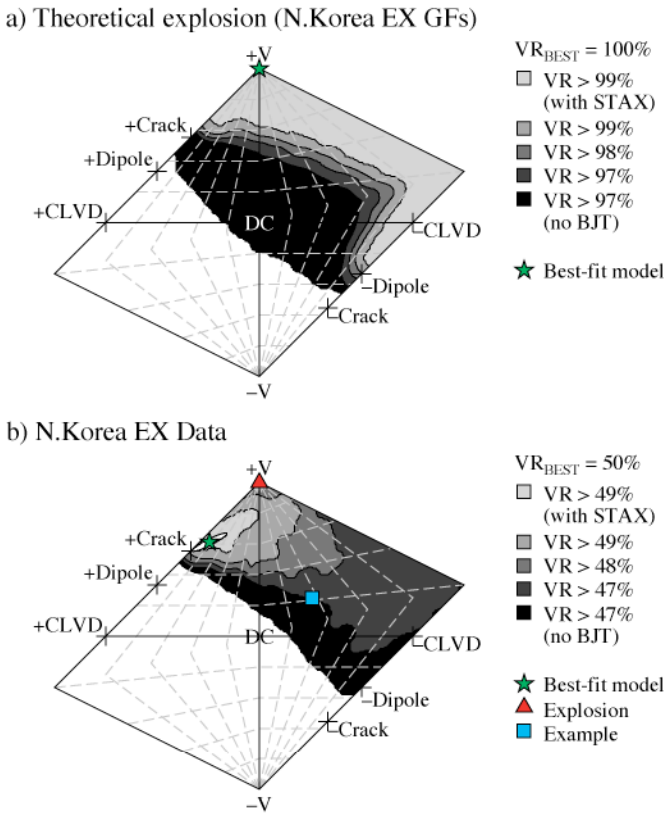
a) Theoretical explosion (N.Korea EX GFs)
+V
+Crack
+Dipole
+CLVD
DC
CLVD
Dipole
Crack
–V
VR_BEST = 100%
VR > 99% (with STAX)
VR > 99%
VR > 98%
VR > 97%
VR > 97% (no BJT)
Best-fit model
b) N.Korea EX Data
+V
+Crack
+Dipole
+CLVD
DC
CLVD
Dipole
Crack
–V
VR_BEST = 50%
VR > 49% (with STAX)
VR > 49%
VR > 48%
VR > 47%
VR > 47% (no BJT)
Best-fit model
Explosion
Example
c) Models and waveforms
T
P
T
P
Explosion (M_W3.6)
Best-fit model (M_W4.1)
Example (M_W3.7)
T
R
V
32 s
MDJ (10-50 s)
6o, 371 km
2.04e-05 cm
INCN (10-20 s)
207o, 473 km
1.64e-05 cm
48 s
TJN (10-20 s)
196o, 566 km
1.21e-05 cm
BJT (10-20 s)
267o, 1101 km
2.24e-05 cm
32 s
STAX (10-50 s)
315o, 371 km
1.54e-05 cm

Figure 4.5 (previous page). Network sensitivity solution (NSS) for the North Korea test (9 Oct 06, $m_b$4.2). a) Theoretical NSS for an explosion where the Green's functions are derived from the actual network setup and the data is noiseless. The best-fit model is an explosion with a VR of 100% (star). Empirical distributions of models and their corresponding VR are also given on the source-type plot. The distributions are also given for solutions where station BJT is not used in the inversion (black) and where the theoretical station STAX is used in the in the inversion (light gray). b) Actual NSS using data from the North Korea test. The best-fit model with a VR of 50.0% (star) along with other models and the corresponding VR distributions is shown similar to a). For comparison, an explosion and a poorly-fitting model with almost no explosive component are also plotted and correspond with the models and waveforms in c). c) Models corresponding to those plotted in b) and their respective forward-predicted waveforms as a function of color compared with the actual waveforms (black line). The left, middle, and right columns are the tangential (T), radial (R), and vertical (V) displacement waveforms, respectively. The text block to the left of the waveforms gives the station name, passband, azimuth, epicentral distance (km), and maximum displacement (cm). The moment magnitudes of the models are also given below the mechanism.

shown in Figure 4.2b as they are in the VR>97% population for the theoretical NSS shown in Figure 4.2a. The example model is very similar to the best-fit and looks to fit the data just as well, but the magnitude is 0.3 units smaller than the best-fit case. This is a consequence of the increased DC moment in the example, which can be viewed graphically as the difference between the star and square on the source-type plot in Figure 4.2b.

Figure 4.4 gives the theoretical and actual NSSs for the earthquake in China, as well as the waveforms for the data and important models described previously. We chose to first run the inversion without GFs for station BJT because the epicentral distance is more than 1000 km and performance of the simple 1-D velocity model employed here degrades at such great distances. When BJT is added, the VR>97% area in Figure 4.4a decreases only slightly and a well-constrained theoretical

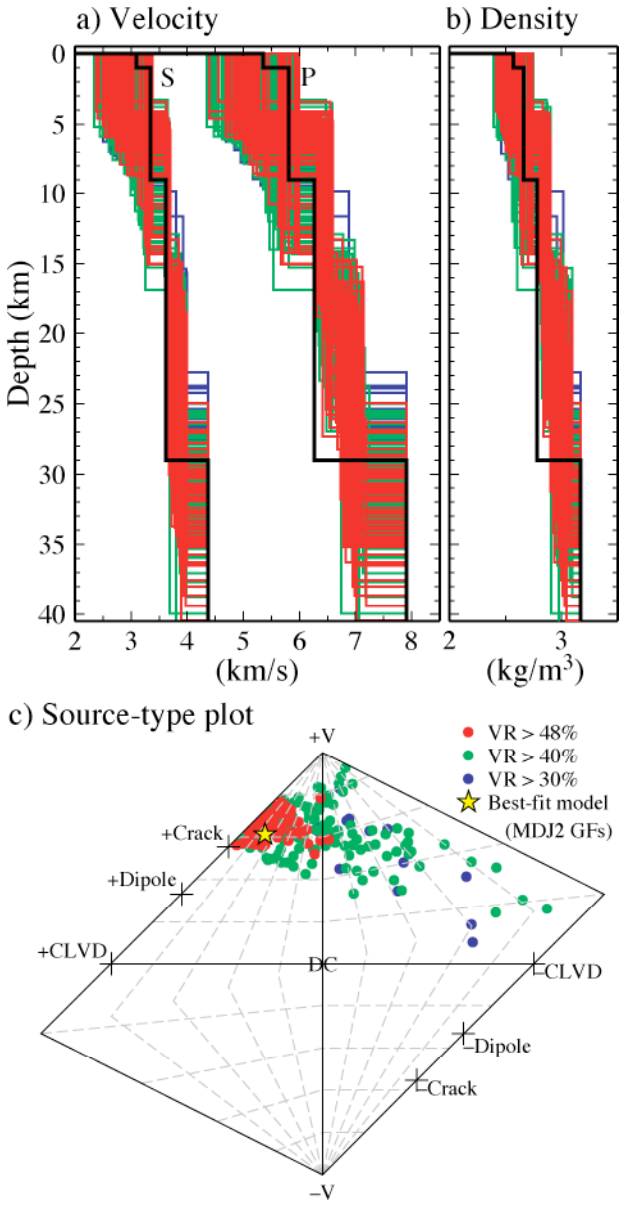


Figure 4.6. Probabilistic velocity model analysis. a) Model parameters for the MDJ2 model (black line) and the 880 Markov-chain Monte Carlo derived models used in the analysis. b) Source-types and associated variance reduction (grayscale) for best-fit models using Green's functions derived using the models in a). The best-fit solution using the MDJ2 velocity model is given by the star.

earthquake is possible with just the three closest stations. This exercise demonstrates another benefit of the theoretical NSS where one can learn before an actual event

which stations are needed to constrain a particular type of source. To that end, we also added an imaginary station, STAX (inverted triangle, Figure 4.3), to see the effect on the NSSs. As expected, the VR>99% region is smaller.

The actual NSS for the earthquake given in Figure 4.4b shows a well-constrained region similar to the theoretical NSS (Figure 4.4a). This result gives us confidence that the MDJ2 model is a good 1-D approximation of the velocity structure in this region, as the expectation is that the small earthquake should be well represented by a double-couple point-source. The waveforms of the best-fit model (VR = 73.7%), shown in Figure 4.4c, fit the data just as well as a pure DC (based on the best-fit model's principal axes). The data for the imaginary station STAX shown in Figure 4.4c are for this mechanism. The model in the VR>70.7% population with the most isotropic energy is shown by the example in Figure 4.4c. This type of comparison is necessary in order to gain an understanding of how the VR relates to waveform misfit.

The solution for the explosion in North Korea is much less constrained than the earthquake due to the simpler radiation pattern. In this case, the theoretical NSS given in Figure 4.5a shows that station BJT is necessary in order to satisfactorily exclude DC sources from the inversion solution. Although this result could be gained from simple inspection of the station configuration shown in Figure 4.3, where without BJT all stations fall along one azimuth with $\pi$ periodicity (a condition that can always fit the two-lobed Rayleigh radiation pattern of a 45-degree dip-slip mechanism), the example is still instructive for cases that aren't so easily visually inspected. With station BJT, the high VR region has the familiar shape from the JUNCTION test.

The addition of station BJT presents some problems for the actual NSS shown in Figure 4.5b, since the measured displacement (2.24e-05 cm) is larger than that of station MDJ (2.04e-05 cm), which is only 371 km from the source. The usual method of weighting the data as a function of inverse distance caused the data from BJT to dominate the inversion, since there is only one station at this very great distance. As a corrective measure, we decreased the weight of data from BJT and produced the actual NSS in Figure 4.5b. The effect of this manual reweighting can be seen in the waveforms (Figure 4.5c), where the best-fit model does not produce as good a fit to the amplitudes at BJT as it does to other stations. The best-fit solutions cluster between an opening crack (+Crack, Figure 4.5b) and an explosion (+V, Figure 4.5b), and the best-fit model has an isotropic component of 60%. With the addition of data for a pure explosion recorded at imaginary station STAX (Figure 4.5c), the highly isotropic nature of the source could be even better constrained. Without STAX, a solution with a VR that is 3% less than the best-fit VR of 50% has only a 20% isotropic component. This source is given by the example shown in Figure 4.5c. The best-fit explosion source is also shown and has an $M_W$ of 3.6, which agrees with the results of Hong and Rhie (2008). For comparison, the formal error ellipse calculated with the method described in Ford et al. (2009) is plotted in Figure 4.5b. The area in the ellipse is much smaller than the region of solutions with a VR only 1% less than the VR for the best-fit solution.

Previous studies of the error introduced by improperly modeled velocity structure have used random perturbations to the best model in order to produce a range of solutions. Here, we use a population of velocity models that are related to variation

in the data used to create them, and hence have a more physical relationship with the range of possible velocity models for a region. Figure 4.6a shows the models obtained from the study of Pasyanos et al. (2006) at one node near the explosion source. The models are on average faster in the mid-crust and slower in the lower crust than the MDJ2 model, which was used to produce the solutions previously discussed and plotted in Figures 4 and 5. Nevertheless, many of these models produce a good fit to the data that is comparable to the fit of the best-fit model using the MDJ2 velocity model to produce the GFs (Figure 4.6b). The best models cluster very near the same region as in Figure 4.5b and in a few cases the fit was actually marginally better than the model using MDJ2 synthetics. These best-fitting models (VR>48%) are colored dark gray in Figure 4.6a and show a trade-off between a) a very thin sediment layer with a fast, thick top-layer, and b) a slow, thick sediment layer with a thin faster top-layer. This range of models straddles the velocity-depth profile given by MDJ2. The worst models (light gray, Figure 4.6a) have a shallow Moho.

## 4.4 Conclusion

Confidence in the best-fit solution for the regional full-waveform moment tensor inversion is dependent on station configuration, data bandwidth, and signal-to-noise ratio (SNR). The best way to characterize that dependence is on a case-by-case basis, where each individual event scenario is analyzed. The network sensitivity solution attempts to do this characterization and is introduced and implemented for the NTS test, JUNCTION, as well as the Oct 06 North Korea test and a nearby earthquake

in China. The theoretical network sensitivity solution provides solution confidence regions for ideal models (explosion or earthquake) with high SNR data. With this type of network sensitivity solution, one can learn if the station configuration and bandwidth is sufficient to resolve a given model. The actual network sensitivity solution assesses confidence using the actual data from the event. Goodness-of-fit for each model is parameterized with a percent variance reduction (VR), where the complete VR space can be mapped out on a source-type plot and the well-fit region of solutions is defined by a chosen threshold VR.

The theoretical network sensitivity solutions for JUNCTION and the North Korea test show a trade-off between –CLVD and explosion, but the well-fit solution space is separated from a double-couple, indicating that an anomalous event can be resolved. In the case of the North Korea test, a specific configuration using the very distant station BJT is required to rule out a DC solution. The actual network sensitivity solution of JUNCTION provides good confidence in the large isotropic component obtained from the inversion. With some additional data weighting, the actual network sensitivity solution of the North Korea test also shows a tight region of well-fit solutions clustered between an opening crack and an explosion, though with the addition of just one more imaginary station, this region is made much smaller. The network sensitivity solutions for the earthquake in China provide high confidence in the best-fit solution, which is indistinguishable from a double-couple. This analysis gives us confidence in the velocity model used to create Green's functions for the inversion.

Variance in the solution caused by a poorly constrained velocity model is assessed by incorporating many hundreds of velocity models for the region obtained from a prior probabilistic study of the source area. A best-fit solution is obtained using each velocity model. The solutions with the greatest VR cluster near the solution obtained with the velocity model used in the prior analysis and therefore contain approximately 60% isotropic moment. Future work can combine spatial and temporal event uncertainty with the velocity model analysis to produce network sensitivity solutions and more completely characterize confidence in a given solution.

# Chapter 5

# Regional Attenuation in Northern California: A Comparison of Five 1-D *Q* Methods

Published as: Ford, S. R., D. S. Dreger, W. R. Walter, K. Mayeda, W. S. Phillips, and L. Malagnini (2008), Regional Attenuation in Northern California: A Comparison of Five 1-D Q Methods, *Bull. Seis. Soc. Amer.*, 98 (4), 2033-2046.

## 5.1 Introduction

Measurement of attenuation $Q^{-1}$ of regional seismic phases provides important input for a variety of geophysical applications. It can help with structure and tectonic interpretation (e.g., Aleqabi and Wysession, 2006; Benz et al., 1997; Frankel et al., 1990), seismic hazard mitigation through better understanding of strong ground motion attenuation (e.g., Anderson et al. 1996; Hanks and Johnston, 1992), simulation of strong ground motions (e.g., Graves and Day, 2003; Olson and Anderson, 1988), and in nuclear explosion monitoring (e.g., Baker et al., 2004; Mayeda et al., 2003; Taylor et al., 2002). A well-known issue with reported values of *Q* for regional phases is that they can vary greatly in the same region depending upon the methodology used to derive them. For example, recent one-dimensional (1-D) *Q* studies in South Korea find frequency-dependent *Q* of the regional seismic phase, *Lg* ($Q_{Lg}$), at 1 Hz ($Q_0$) varies between 450 and 900 (Chung and Lee 2003; Chung et al., 2005). Another

Table 5.1. Event parameters

| Event (YYYYDDDHHMM) | Lat | Lon | Mag | Dep (km) |
|---|---|---|---|---|
| 19922480043 | 37.91 | -120.50 | 2.5 | 0.8 |
| 19922941302 | 39.99 | -120.72 | 3.6 | 0.2 |
| 19930151113 | 37.91 | -122.28 | 2.9 | 6.3 |
| 19930160629 | 37.01 | -121.46 | 5.1 | 7.9 |
| 19930412148 | 40.32 | -119.68 | 4.5 | 4.5 |
| 19932232233 | 37.31 | -121.67 | 5.0 | 9.3 |
| 19932640545 | 42.36 | -122.08 | 5.7 | 6.6 |
| 19933181225 | 35.95 | -120.49 | 5.0 | 11.7 |
| 19940661649 | 38.84 | -119.73 | 3.7 | 0.1 |
| 19941111637 | 36.29 | -120.43 | 4.4 | 9.8 |
| 19941770842 | 37.91 | -122.28 | 4.0 | 6.6 |
| 19942501910 | 37.50 | -121.28 | 4.0 | 2.9 |
| 19942551223 | 38.80 | -119.69 | 5.9 | 0.1 |
| 19942560615 | 38.77 | -119.70 | 4.1 | 0.1 |
| 19943222050 | 39.16 | -119.74 | 4.1 | 6.2 |
| 19943541027 | 35.91 | -120.46 | 5.0 | 9.1 |
| 19950160134 | 38.82 | -122.79 | 3.9 | 2.1 |
| 19950180353 | 37.15 | -121.56 | 2.2 | 3.0 |
| 19950260424 | 37.76 | -121.93 | 2.6 | 8.1 |
| 19950322204 | 40.86 | -121.17 | 3.5 | 8.3 |
| 19950341133 | 36.59 | -121.05 | 2.9 | 9.3 |
| 19950581813 | 38.36 | -122.23 | 2.7 | 0.1 |
| 19950592309 | 38.93 | -122.62 | 4.0 | 5.7 |
| 19950931142 | 39.50 | -122.97 | 2.6 | 8.9 |
| 19951131412 | 36.60 | -121.20 | 2.3 | 6.7 |
| 19951221256 | 40.18 | -123.16 | 3.9 | 35.3 |
| 19951261246 | 40.38 | -123.67 | 3.5 | 27.4 |
| 19951362001 | 39.80 | -122.73 | 3.3 | 1.3 |
| 19951370229 | 39.80 | -122.73 | 4.2 | 3.6 |
| 19951692223 | 39.83 | -120.78 | 4.0 | 0.1 |
| 19951991355 | 38.82 | -122.79 | 2.8 | 4.8 |
| 19952471416 | 38.68 | -122.74 | 4.4 | 7.6 |
| 19952562036 | 37.09 | -121.51 | 4.1 | 8.2 |
| 19952570822 | 37.10 | -121.51 | 3.7 | 7.8 |
| 19952651447 | 38.76 | -118.58 | 4.2 | 5.0 |
| 19952680951 | 38.99 | -121.65 | 2.4 | 22.8 |
| 19953152019 | 40.37 | -123.66 | 3.6 | 24.8 |
| 19953192033 | 39.62 | -120.05 | 4.4 | 0.1 |
| 19953352311 | 37.92 | -122.28 | 3.5 | 9.2 |
| 19953470544 | 36.97 | -121.46 | 3.3 | 5.3 |
| 19960040014 | 38.69 | -119.65 | 2.7 | 0.6 |
| 19960330040 | 39.94 | -120.88 | 3.7 | 0.1 |
| 19961422050 | 37.35 | -121.72 | 4.8 | 8.1 |
| 19962332303 | 38.93 | -122.68 | 2.3 | 1.9 |
| 19962860425 | 38.74 | -122.71 | 3.6 | 3.6 |
| 19962922011 | 37.62 | -119.39 | 3.0 | 6.4 |
| 19963230656 | 38.79 | -122.74 | 3.7 | 3.4 |
| 19963321107 | 39.77 | -121.69 | 2.8 | 21.8 |
| 19963322017 | 36.09 | -117.61 | 5.3 | 6.8 |
| 19963392121 | 38.79 | -122.75 | 3.9 | 3.4 |
| 19970220717 | 40.27 | -124.38 | 4.8 | 23.6 |
| 19970260623 | 40.28 | -124.39 | 4.0 | 21.9 |
| 19970360025 | 38.36 | -122.65 | 3.6 | 6.7 |
| 19970861539 | 38.14 | -121.93 | 3.6 | 21.5 |
| 19971491021 | 37.11 | -121.52 | 3.3 | 8.0 |
| 19971751148 | 40.46 | -121.55 | 2.9 | 4.3 |
| 19971950611 | 37.17 | -122.33 | 3.7 | 13.9 |
| 19971981946 | 36.96 | -121.59 | 4.1 | 7.3 |
| 19972040318 | 40.90 | -123.37 | 3.9 | 26.3 |
| 19972181929 | 40.75 | -124.45 | 4.2 | 21.3 |
| 19972331611 | 38.60 | -118.51 | 4.5 | 23.1 |
| 19972980854 | 39.60 | -122.06 | 3.8 | 12.9 |
| 19973091749 | 39.94 | -120.91 | 4.7 | 0.0 |
| 19973260133 | 38.88 | -123.21 | 3.7 | 3.0 |
| 19973522119 | 40.30 | -124.46 | 4.4 | 9.4 |
| 19980251642 | 41.09 | -121.92 | 3.4 | 0.0 |
| 19980482208 | 39.85 | -120.51 | 4.0 | 0.0 |
| 19980650547 | 36.08 | -117.63 | 4.2 | 7.9 |
| 19980660036 | 36.09 | -117.61 | 4.6 | 6.7 |
| 19980861934 | 40.99 | -121.59 | 3.5 | 18.8 |
| 19981660159 | 37.03 | -121.47 | 4.0 | 8.5 |
| 19982020838 | 40.62 | -122.40 | 4.5 | 23.0 |
| 19982181507 | 37.37 | -119.99 | 2.7 | 18.2 |
| 19982201626 | 37.42 | -119.93 | 3.5 | 26.8 |
| 19982830650 | 36.95 | -121.57 | 4.0 | 6.5 |
| 19982880505 | 40.83 | -123.55 | 3.9 | 26.3 |
| 19982931839 | 39.74 | -120.66 | 2.8 | 0.0 |
| 19982940831 | 39.73 | -120.68 | 4.1 | 0.0 |
| 19983301949 | 40.62 | -122.40 | 5.1 | 23.3 |
| 19983381216 | 37.92 | -122.28 | 4.1 | 6.8 |
| 19990241534 | 39.55 | -123.77 | 4.0 | 5.5 |
| 19990270358 | 37.25 | -121.63 | 3.7 | 6.5 |
| 19990490858 | 38.78 | -122.77 | 3.9 | 2.3 |
| 19990940600 | 38.84 | -122.75 | 3.8 | 4.2 |
| 19991352140 | 37.48 | -118.84 | 4.0 | 5.9 |
| 19992100452 | 38.79 | -122.73 | 3.6 | 3.9 |
| 19992300106 | 37.90 | -122.68 | 4.9 | 6.6 |
| 19992652227 | 38.39 | -122.63 | 4.2 | 9.7 |
| 19992720622 | 41.36 | -123.43 | 3.9 | 38.1 |
| 19993120153 | 37.35 | -118.58 | 4.4 | 9.4 |
| 19993461812 | 39.66 | -118.42 | 4.0 | 6.6 |
| 19993522104 | 39.79 | -122.64 | 2.9 | 15.3 |
| 19993601941 | 40.27 | -124.40 | 4.1 | 23.3 |
| 20000062138 | 38.84 | -122.82 | 3.3 | 2.4 |
| 20000102141 | 38.75 | -122.91 | 4.2 | 6.8 |
| 20000111419 | 38.76 | -122.91 | 4.3 | 6.8 |
| 20000182326 | 38.75 | -122.91 | 4.2 | 7.6 |
| 20000592308 | 36.09 | -117.57 | 4.0 | 6.6 |
| 20000851622 | 36.90 | -121.01 | 3.7 | 4.6 |
| 20000881516 | 36.00 | -117.87 | 4.0 | 7.5 |
| 20000960220 | 38.78 | -122.77 | 3.6 | 5.7 |
| 20001382232 | 39.39 | -123.06 | 4.1 | 8.0 |

Table 5.1. (Continued) Event parameters

| Event (YYYYDDDHHMM) | Lat | Lon | Mag | Dep (km) |
|---|---|---|---|---|
| 20001971156 | 37.97 | -122.03 | 3.6 | 15.3 |
| 20002340445 | 39.33 | -123.03 | 3.7 | 13.3 |
| 20002470836 | 38.37 | -122.41 | 5.1 | 10.1 |
| 20002481027 | 38.23 | -119.40 | 3.1 | 10.3 |
| 20002661050 | 40.85 | -124.46 | 4.3 | 13.2 |
| 20003371534 | 39.35 | -120.47 | 4.3 | 5.3 |
| 20003430741 | 38.78 | -122.76 | 4.1 | 4.0 |
| 20010332303 | 39.72 | -122.80 | 3.9 | 12.1 |
| 20010562318 | 37.33 | -121.69 | 4.4 | 7.7 |
| 20010701011 | 39.48 | -122.94 | 3.7 | 17.3 |
| 20011372153 | 35.79 | -118.03 | 4.1 | 12.0 |
| 20011630241 | 39.37 | -120.47 | 2.8 | 5.4 |
| 20011951730 | 36.02 | -117.87 | 4.0 | 7.8 |
| 20011981207 | 36.01 | -117.86 | 4.6 | 9.0 |
| 20012222019 | 39.81 | -120.61 | 5.5 | 3.9 |
| 20012802113 | 39.79 | -121.64 | 3.0 | 19.9 |
| 20013411429 | 39.04 | -123.11 | 4.0 | 6.9 |
| 20013480941 | 39.04 | -123.12 | 4.0 | 6.9 |
| 20013622114 | 36.64 | -121.25 | 4.6 | 6.8 |
| 20020610719 | 40.82 | -120.66 | 3.1 | 4.2 |
| 20021190043 | 40.60 | -124.45 | 4.3 | 29.7 |
| 20021340500 | 36.96 | -121.59 | 4.9 | 7.1 |
| 20021651240 | 36.66 | -116.09 | 4.2 | 7.8 |
| 20021681655 | 40.82 | -124.60 | 5.0 | 22.3 |
| 20021962018 | 37.38 | -118.40 | 4.0 | 13.6 |
| 20022942230 | 39.52 | -119.20 | 3.4 | 0.1 |
| 20023161648 | 35.97 | -120.52 | 4.2 | 8.5 |
| 20030722229 | 36.80 | -121.38 | 4.3 | 8.8 |
| 20030250911 | 35.33 | -118.66 | 4.0 | 15.2 |
| 20030331822 | 37.74 | -121.94 | 4.1 | 16.7 |
| 20030671535 | 37.57 | -118.88 | 4.0 | 5.4 |
| 20031450709 | 38.45 | -122.69 | 4.3 | 5.0 |
| 20031461038 | 36.97 | -120.16 | 3.7 | 6.4 |
| 20031500903 | 36.99 | -120.18 | 3.1 | 7.2 |
| 20032091910 | 39.23 | -122.26 | 3.1 | 3.2 |
| 20032110450 | 38.68 | -122.90 | 4.0 | 5.0 |
| 20032151200 | 38.79 | -122.76 | 4.2 | 0.8 |
| 20032480139 | 37.84 | -122.22 | 4.1 | 10.8 |
| 20032921532 | 37.90 | -122.14 | 3.5 | 8.3 |
| 20033192119 | 38.22 | -117.87 | 3.8 | 3.1 |
| 20033561915 | 35.70 | -121.09 | 6.5 | 8.0 |
| 20040021047 | 35.70 | -121.15 | 3.8 | 7.4 |
| 20040190402 | 37.72 | -121.80 | 2.2 | 18.8 |
| 20040200519 | 37.71 | -121.81 | 3.2 | 17.1 |
| 20040200544 | 37.71 | -121.81 | 2.3 | 17.7 |
| 20040201224 | 35.54 | -120.84 | 2.2 | 2.8 |
| 20040210623 | 37.72 | -121.81 | 3.5 | 18.6 |
| 20040210635 | 37.72 | -121.81 | 3.4 | 18.4 |
| 20040210735 | 37.72 | -121.81 | 3.0 | 18.5 |
| 20040451242 | 38.76 | -119.65 | 2.2 | 2.0 |
| 20042622302 | 38.01 | -118.68 | 5.5 | 7.3 |

example is Tibet, where analyses using the same data, but different methods produce a factor of three difference in $Q_0$ (McNamara et al., 1996; Xie, 2002). Different data in similar regions in Tibet find a factor of two difference in the power-law dependence that is also dependent on the frequency band in which $Q_{Lg}$ is measured (Fan and Lay 2003a; Xie et al., 2004). Previous work in Northern California has produced best-fit 1-D power-law models ($Q_0 f^n$) of $129f^{0.57}$ (Mayeda et al., 2005) and $105(\pm 26)f^{0.67(\pm 0.16)}$ (Erickson et al., 2004), and $180f^{0.42}$ in the San Francisco Bay Area (Malagnini et al., 2007), though, as described below, the focus of this article is not to present a best 1-D *Q* for Northern California, but rather to document each of the methods and

Table 5.2. Station parameters

| Station | Network | Lat | Lon | Elevation |
|---|---|---|---|---|
| ARC | BK | 40.8777 | -124.0774 | 30 |
| BKS | BK | 37.8762 | -122.2356 | 244 |
| CMB | BK | 38.0346 | -120.3865 | 697 |
| CVS | BK | 38.3453 | -122.4584 | 295 |
| FARB | BK | 37.6978 | -123.0011 | 18 |
| HOPS | BK | 38.9935 | -123.0723 | 299 |
| KCC | BK | 37.3236 | -119.3187 | 888 |
| MHC | BK | 37.3416 | -121.6426 | 1250 |
| MOD | BK | 41.9025 | -120.3029 | 1554 |
| ORV | BK | 39.5545 | -121.5004 | 335 |
| PKD | BK | 35.9452 | -120.5416 | 583 |
| POTR | BK | 38.2026 | -121.9353 | 20 |
| SAO | BK | 36.7640 | -121.4472 | 317 |
| WDC | BK | 40.5799 | -122.5411 | 268 |
| WENL | BK | 37.6221 | -121.7570 | 139 |
| YBH | BK | 41.7320 | -122.7104 | 1060 |

demonstrate a strategy for more reliable determination of $Q_0$ and its frequency dependence $\eta$.

In order to reliably use reported $Q$ estimates for other geophysical applications it is essential to know the uncertainty in the estimate. Commonly, individual studies will present aleatoric (random) uncertainty, however epistemic (bias) uncertainty is not possible to assess when only a single method and parameterization is considered. To this end, we implement four commonly applied methods and one new method to measure $Q_{Lg}$, using a high-quality dataset from the Berkeley Digital Seismic Network (BDSN), in order to better understand the effects of different methods and parameterizations on $Q$ models. The coda normalization (CN) method is implemented in the time domain for paths leading to a common station and it returns a stable $Q$

measurement when the region near a station is homogenous. The coda-source normalization (CS) method uses previously calculated coda-derived source spectra to remove the source term in the frequency domain and is best suited to calculate an effective $Q$ for a given path. The two-station (TS) and reverse two-station (RTS) methods are implemented in the frequency domain and the calculated $Q$ is more stable due to the extraction of the source term. The RTS method produces a power-law $Q$ with less error than the TS method due to its additional extraction of the site terms, though it is more restrictive in its data requirements. The source-pair / receiver-pair (SPRP) method is the RTS method with a relaxation of the data requirements and is implemented in the time domain here. With a more complete knowledge of uncertainty it will be possible to better assess the results of published attenuation studies. Future efforts that employ the multi-method analysis presented here can lead to improved estimates of regional $Q$.

## 5.2 Data and Methods

We utilize a dataset consisting of 158 earthquakes recorded at 16 broadband (20 sps) three-component stations of the BDSN between 1992 and 2004 (Figure 5.1, Tables 5.1 and 5.2). An example of the high-quality recordings is given in Figure 5.1b. The wide distribution of data parameters allows for detailed sensitivity testing. We calculate $Q_{Lg}$ by fitting the power-law model, $Q_0 f^{\eta}$, using the five different methods. The first two methods, CN and CS, use the seismic coda to correct for the source effect. The last three methods, TS, RTS and SPRP, use a spectral ratio technique to

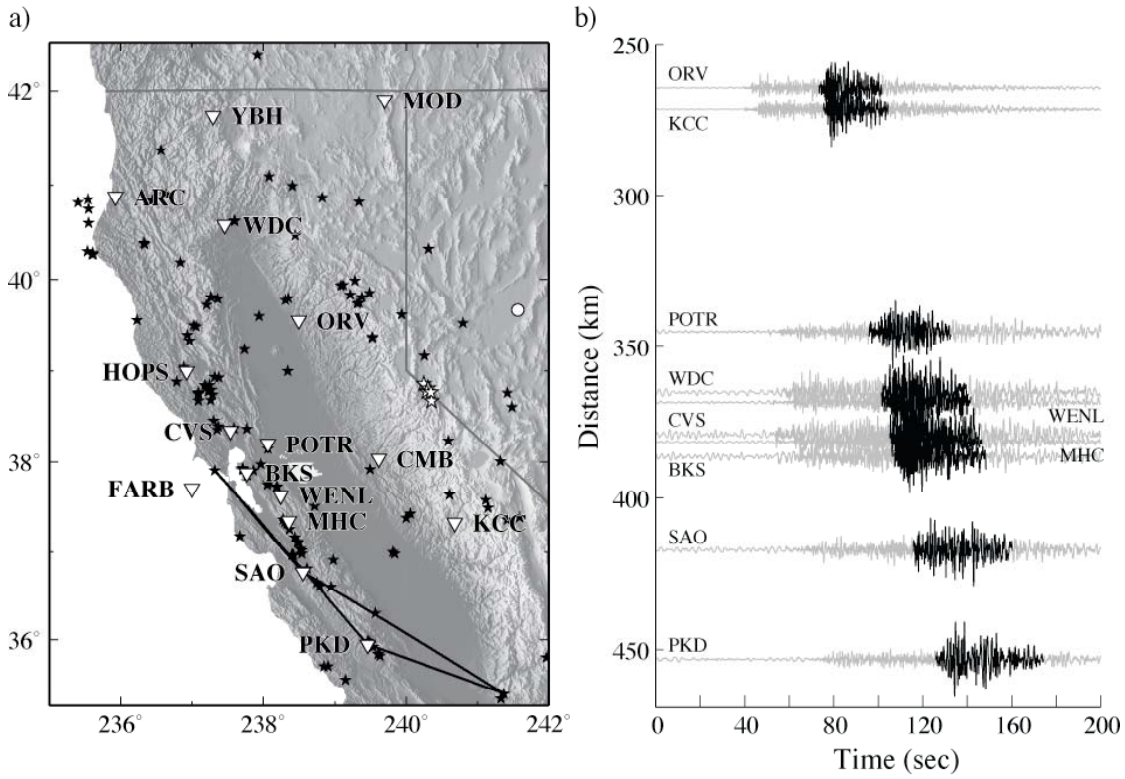


Figure 5.1. a) Events (stars) and stations (inverted triangles) used to calculate $Q_{Lg}$ in Northern California. The great-circle paths used in the example figures for the CS, TS and RTS methods are black. b) Record section for M4 event on 12 Dec 99 (white circle in (a)) of vertical component waveforms bandpassed between 0.25 - 8 Hz (the total band employed in this study). The *Lg* portion of the waveform as defined by the group velocity window 2.6-3.6 km/s (the total window of this study) is black.

correct for source and, in the case of RTS and SPRP, site effects. In the following we summarize the methods and point out significant differences. Our philosophy in presenting each of the methods is to maintain the approach and style of the commonly applied version of each method as closely as possible. Later, we will attempt to normalize each of the methods for comparison and sensitivity testing. Examples of each method are provided using the control parameterization given in Table 5.3, where the data used are for paths and stations highlighted in Figure 5.1a.

Table 5.3. $Q_{Lg}$ measurement method parameterization for sensitivity tests

| Group | Spreading exponent [$\gamma$] | Measurement bandwidth (Hz) | Epicentral distance [$r$] (km) | *Lg* velocity window (km/s) |
|---|---|---|---|---|
| Control | 0.5 | 0.5 - 8 | 100 - 400 | 2.6 - 3.5 |
| Test 1 ($\gamma$) | **0.83** | | | |
| Test 2 (Bandwidth) | | **0.25 - 4** | | |
| Test 3 (Distance) | | | **100 - 700** | |
| Test 4 (Window) | | | | **3.0 - 3.6** |

### 5.2.1 Coda normalization (CN)

The CN method uses the local shear-wave coda as a proxy for the source and site effects, thus amplitude ratios remove these two effects from the *S*-wave spectrum (Aki, 1980; Yoshimoto et al., 1993). In his original application, Aki (1980) assumed that the local shear-wave coda was homogeneously distributed in space and time. For the current study region, Figure 1 of Mayeda et al. (2005) shows that the coda at ~1 Hz is in fact homogeneous, at least up to ~240 km. More recently, we have evidence that the high frequencies are also homogeneous and thus the extension of the Aki (1980) method to near-regional distances is warranted. However, the distance limit of the homogeneity assumption has not been fully tested and may manifest in the parameter analysis below. This method assumes the *Lg* amplitude $A_{Lg}$ at a given distance $r$ and frequency $f$ can be estimated by

$$A_{Lg}(f,r) = S(f)R(\theta)I(f)P(f)G(r)\exp\left(\frac{-r\pi f}{QU}\right), \qquad (5.1)$$

where $S(f)$ is the source spectrum and $R(\theta)$ is the source radiation in the source-receiver direction $\theta$. $P(f)$ is the site term, $I(f)$ is the instrument term, and $G(r)$ is the geometrical spreading term, approximated here as

$$G(r) = \left(\frac{1}{r}\right)^{\gamma}, \tag{5.2}$$

where $\gamma$ is given in Table 5.3. The final term is an apparent attenuation, where $U$ is the *Lg* group velocity, which is fixed at 3.5 km/s for this and all other methods. The CN method also assumes that the coda spectrum $C(f)$ is approximately equal to the source spectrum at a given critical propagation time $t_C$, or

$$C(f,t_C) = S(f)I(f)P(f)E(f,t_C), \tag{5.3}$$

where $E(f,t_C)$ is a coda excitation term that represents how the spectral amplitude decays with time. The coda excitation term is assumed to be constant at all distances for a given $t_C$. If the source radiation is smoothed by considering several sources at many source-receiver directions we can take the ratio of $A_{Lg}$ to $C$, measured at $t_C$, which effectively removes instrument, site, and source contributions resulting in the geometrical spreading and attenuation terms. The natural log of this spectral ratio taken at discrete frequency bands (between 0.25, 0.5, 1, 2, 4, and 8 Hz) results in the equation of a line as a function of distance,

$$\ln\left(\frac{A_{Lg}(f)r^{\gamma}}{C(f,t_C)}\right) = \frac{-r\pi f}{QU} + K, \tag{5.4}$$

where $K$ is the constant derived from the coda excitation factor and the slope is related to $Q^{-1}$. $Q^{-1}$ at the center frequency of each band then reveals a power-law model for each station.

$A_{Lg}$ is the maximum envelope amplitude in each bandpassed (8-pole acausal Butterworth filter), windowed (according to the window parameter in Table 5.3) and tapered (10% cosine window) raw vertical trace. *C* is the root-mean-square (rms) amplitude in each bandpassed 10 second window centered on a $t_C$ of 150 seconds. Data were excluded if either $A_{Lg}$ or *C* had a SNR less than two, where noise is measured as the maximum amplitude in a window the same length as $A_{Lg}$ prior to the event. This method is similar to that of Chung and Lee (2003), whereas Frankel et al. (1990) used a weighted average of the smoothed coda to measure *C*. We calculate (4) with all records at a given station, where the slope ($Q^{-1}$) is calculated with an iteratively weighted least-squares method that reduces the influence of outlier observations. An example for station PKD is given in Figure 5.2. The resulting $Q^{-1}$ are then fit in the log domain as a function of midpoint frequency with a weighted (the squared inverse of the standard error in each $Q^{-1}$ measurement) least-squares line to calculate the power-law parameters (Figure 5.2b). We bootstrap the residuals of the weighted fit 1000 times with replacement to calculate standard error of the power-law parameters. This bootstrapping method randomly adds the residuals of the inversion to the fit and repeats the inversion. The procedure is repeated *n* times with replacement, and variance in the fit parameters can be extracted from the empirical covariance matrix calculated from the model parameter population of size *n* (Aster et al., 2004; Moore and McCabe, 2002). Resampling more than 1000 times introduced no additional variation.

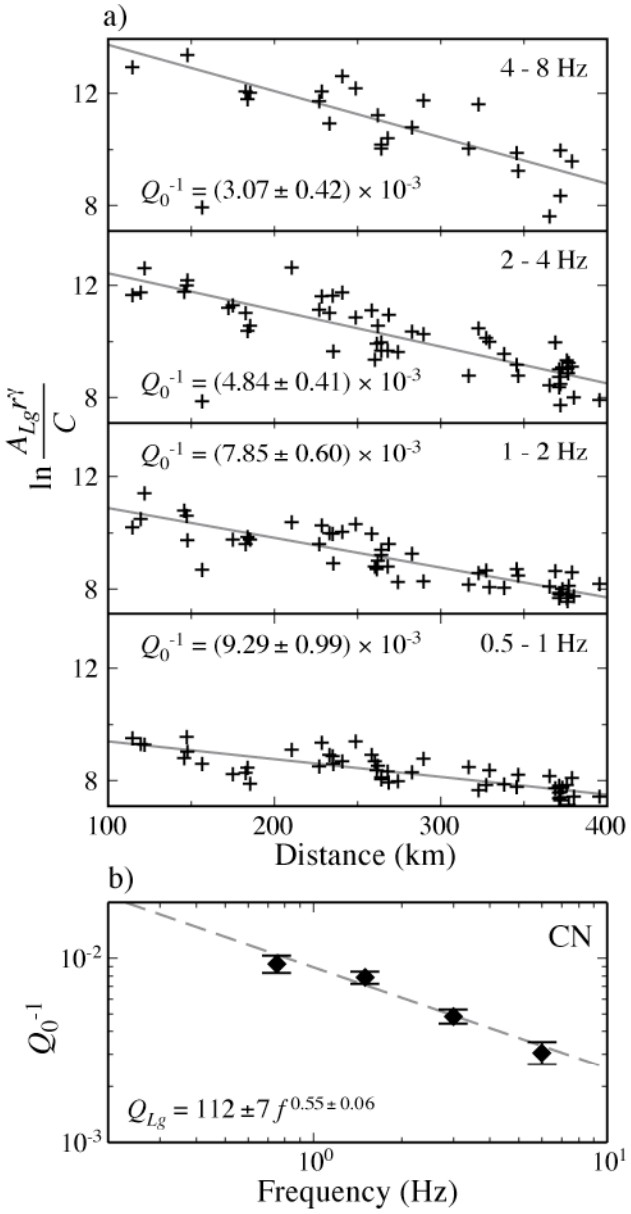


Figure 5.2. $Q_{Lg}$ at station PKD measured by the coda normalization method. a) Robust regression of coda normalized *Lg* amplitudes (crosses) versus distance where the spreading exponent $\gamma$ is 0.5 and the bandwidth of the measurement is in the upper right corner. The slope is related to $Q^{-1}$ which is given on the left with standard error. b) Weighted regression of $Q^{-1}$ (diamonds with standard error bars) versus frequency bandwidth midpoint, where the power-law attenuation parameters with standard deviations are given in the lower left.

### 5.2.2 Coda-source normalization (CS)

The CS method uses the stable, coda-derived source spectra to isolate the path attenuation component of the *Lg* spectrum. This new method to measure *Q* is described in Walter et al., (2007). The method assumes $A_{Lg}$ is represented as in equation (1) with $S(f)$ described as in Aki and Richards (2002),

$$S(f) = \frac{\dot{M}(t)}{4\pi\sqrt{\rho_s\rho_r\beta_s\beta_r\beta_s^2}}, \tag{5.5}$$

where $\dot{M}(t)$ is the moment-rate time function, and $\rho$ and $\beta$ are the density and velocity of the medium near the source, *s*, and receiver, *r*, respectively. We use an average $\rho$ of 2600 kg/m$^3$ and $\beta$ of 3000 m/s near both the source and receiver. $R(\theta)$ is fixed at 0.6, the absolute value average of the radiation pattern for a double-couple (Boore and Boatwright, 1984). $G(r)$ is a critical distance formulation (Street et al., 1975),

$$G(r) = \begin{cases} r^{-1} & \text{for } r < r_0 \\ \frac{1}{r_0}\left(\frac{r_0}{r}\right)^{\gamma} & \text{for } r \geq r_0 \end{cases}, \tag{5.6}$$

where $\gamma$ is given in Table 5.3. We fix $r_0$ at 60 km, which is two times an approximate crustal thickness for the region. We assume a site term $P(f)$ of unity and thus any site effect is projected into the path attenuation term.

The windowed (according to the window parameter in Table 5.3) and tapered (10% cosine window) transverse component is transferred to velocity and its Fourier amplitude is calculated. $A_{Lg}$ is then the mean of the Fourier amplitude for fixed discrete frequency bands (between 0.2, 0.3, 0.5, 0.7, 1, 1.5, 2, 3, 4, 6, and 8 Hz). Path attenuation can then be extracted with the log transform via

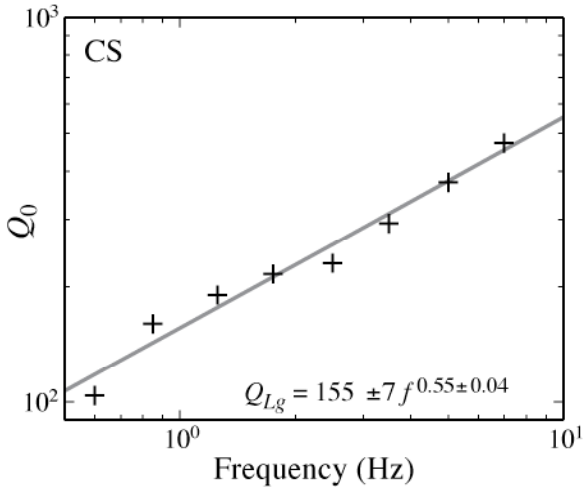


Figure 5.3. $Q_{Lg}$ for the path between event 1999230010618 (see Table 5.1) and station PKD measured by the coda-source normalization method. $Q_0 f^{\eta}$ with standard error is given in the lower right.

$$Q(f) = \frac{\left(r\pi f \log(e)/U\right)}{\log\left(S(f)\right) + \log\left(G(r)\right) + \log\left(P(f)\right) - \log\left(A_{Lg}(f)\right)}, \tag{5.7}$$

where the same frequency bands are used to calculate the source spectra, $S(f)$. Source spectra derived from the coda are calculated via the methodology of Mayeda et al. (2003) and are from the Northern California study of Mayeda et al. (2005). $Q(f)$ is only calculated for records where $A_{Lg}$ is two times the amplitude of the pre-event signal (SNR > 2). $Q$ at the center frequency of each band then reveals a power-law model for each event-station path.

We fit a least-squares line in the log domain (a robust regression gave similar results) and the intercept term is then the log transform of $Q_0$ and the slope is $\eta$ (Figure 5.3). We bootstrap the residuals of the fit to calculate standard error of the power-law parameters as described in the CN method.

### 5.2.3 Two-station (TS)

The TS method takes the ratio of *Lg* recorded at two different stations along the same narrow path from the same event in order to remove the common source term (e.g., Xie and Mitchell, 1990). We implement this method in the frequency domain and take the ratio of two *Lg* signals with the form of equation (1) that are recorded at station 1 and station 2, which gives

$$\frac{A_{Lg}^{1}(f)}{A_{Lg}^{2}(f)} = \frac{S(f)R(\theta)I^{1}(f)P^{1}(f)G(r_1)}{S(f)R(\theta)I^{2}(f)P^{2}(f)G(r_2)}\exp\left(\frac{(r_2 - r_1)\pi f}{QU}\right), \tag{5.8}$$

where the superscripts refer to station 1 or 2 and $r_1 < r_2$. If we assume the ratio of the site terms ($P^1(f)/P^2(f)$) to be near unity we can linearize equation (8) with the natural log transform to obtain

$$\alpha(f) = \frac{U}{\pi(r_2 - r_1)}\ln\left(\frac{A_{Lg}^{1}}{A_{Lg}^{2}}\left(\frac{r_1}{r_2}\right)^{\gamma}\right) = \frac{f^{(1-\eta)}}{Q}, \tag{5.9}$$

assuming a power-law model for attenuation and $G(r)$ as in equation (2). $A_{Lg}$ is the Fourier amplitude spectra of the windowed (according to the window parameter in Table 5.3) and tapered (10% cosine window) vertical component that has been transferred to velocity. We only calculate ratios where the smoothed (moving average of 0.4 Hz) Fourier amplitude ratio of $A_{Lg}$ to pre-event signal is greater than two (SNR > 2), and where $\alpha(f)$ is directly proportional to frequency. This method requires the choice of a maximum azimuth in order to define the experimental set-up. Chun et al. (1987) used 10º, whereas Xie (2002) uses 12 and 30º. We limit the azimuthal gap between stations and event to a conservative 15° since we do not test this parameter.

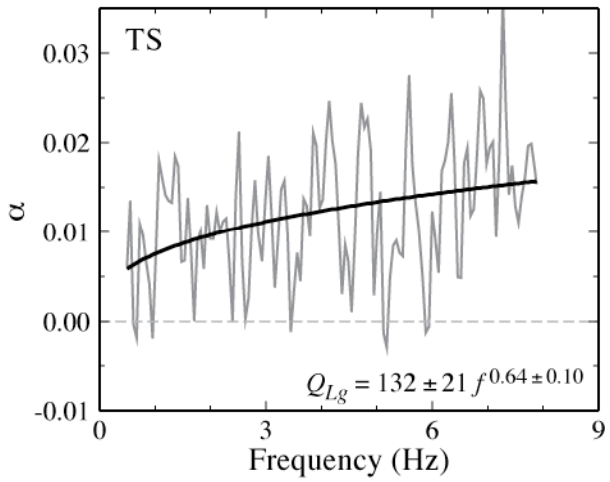


Figure 5.4. $Q_{Lg}$ measured by the two-station method for the path between stations PKD and SAO from event 1999230010618 (see Table 5.1). The best-fit parameters are given in the lower right with standard error. Notice the $\alpha < 0$ at some points which creates a singularity when the power-law model is linearized with the log transform.

$\alpha(f)$ is decimated so that the frequency step $\Delta f$ is

$$\Delta f = \frac{f_{Nyq}}{L}, \tag{5.10}$$

where $f_{Nyq}$ is the Nyquist frequency of the $A_{Lg}$ time-series and $L$ is the number of points. This is done so that $\alpha(f)$ represents the resolution of the discrete Fourier transform. Equation (8) can be transformed to the log-domain and a linear regression is possible to calculate the power-law parameters. However, random error due to propagation can produce a negative $\alpha(f)$ at some frequencies (Xie, 1998), which prohibits analysis in the log-domain. Figure 5.4 illustrates this effect. Therefore, we perform a non-linear regression on $\alpha(f)$ that minimizes the sum of squares error on the power-law function in the least-squares sense (Bates and Watts, 1988). We bootstrap

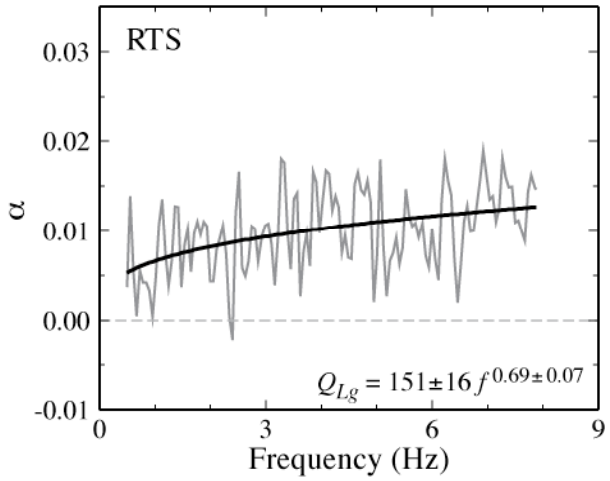


Figure 5.5. $Q_{Lg}$ measured by the reverse two-station method for the path between stations PKD and SAO for events 1999230010618 and 2004273225453 (see Table 5.1). The best-fit parameters are given in the lower right with standard error.

the residuals of the non-linear fit to calculate standard error of the power-law parameters as described in the CN method, where the inversion is done non-linearly.

### 5.2.4 Reverse two-station (RTS)

The RTS method uses two TS station-event configurations and forms a ratio of two equations of the form of (8), where a source is on either side of the station pair in a narrow azimuthal window (Chun et al., 1987). The two ratios are combined to remove the common source and site terms to give

$$\alpha(f) = \frac{U}{\pi(r_2 - r_1 + r_4 - r_3)} \ln\left(\frac{A_{Lg}^1 A_{Lg}^3}{A_{Lg}^2 A_{Lg}^4}\left(\frac{r_1 r_3}{r_2 r_4}\right)^{\gamma}\right) = \frac{f^{(1-\eta)}}{Q}, \qquad (5.11)$$

where $r_2 > r_1$ and $r_4 > r_3$ and $G(r)$ as in equation (2). $\alpha(f)$ is calculated similarly to the TS method. Figure 5.5 shows an example of the RTS method for the same interstation path as the TS example given in Figure 5.4. The RTS method reduces the variance of $\alpha(f)$.

### 5.2.5 Source-pair/receiver-pair (SPRP)

The SPRP method is the RTS method with a relaxation on the narrow azimuthal window requirement (Shih et al., 1994). We implement this method in the time domain so that equation (11) becomes

$$\ln\left(\frac{A_{Lg}^1 A_{Lg}^3}{A_{Lg}^2 A_{Lg}^4}\left(\frac{r_1 r_3}{r_2 r_4}\right)^{\gamma}\right) = \frac{\pi f}{QU}(r_2 - r_1 + r_4 - r_3). \tag{5.12}$$

Unlike the RTS method, data are no longer restricted by a given azimuth, but by a distance formulation

$$r_A^2 > (SP^2 + r_B^2), \tag{5.13}$$

where the subscript A refers to the larger epicentral distance records ($r_2$ and $r_4$) and B refers to the smaller distance records ($r_1$ and $r_3$), and $SP$ is the distance between stations and must be greater than 50 km (see Figure 2 of Chung et al., 2005). This can give an effective maximum azimuthal gap at some interstation distances of 70°. $A_{Lg}$ is the maximum zero-to-peak amplitude in each bandpassed (8-pole acausal Butterworth filter), windowed (according to the window parameter in Table 5.3) and tapered (10% cosine window) vertical component record that has been transferred to velocity. The left side of equation (12) is least-squares fit as a function of the effective interstation distance, ($r_2$ - $r_1$ + $r_4$ - $r_3$), for the same discrete frequency bands as in the CN method,

where $f$ is the midpoint of these frequency bands (Figure 5.6a). We require the correlation of the fit be positive and the correlation coefficient be nonzero with a high degree of confidence ($p < 0.05$). The slope of the fit is a function of $Q^{-1}$ in the band that it was measured. The positive correlation constraint forces $Q^{-1}$ in each band to be nonnegative. Negative $Q^{-1}$ is physically unrealistic and occurred in less than 2% of the measurements. The resulting $Q^{-1}$ are then fit in the log domain as a function of midpoint frequency with a weighted (the squared inverse of the standard error in each $Q^{-1}$ measurement) least-squares line to calculate the power-law parameters (Figure 5.6b). Standard error in the power-law parameters is from the covariance matrix estimated from the residuals.

We note that in the example calculation given in Figure 5.6, where $Q_{Lg}$ is estimated between stations PKD and SAO, that $Q^{-1}$ between 1 and 2 Hz in Figure 5.6a is so small as to not be a visible data point on Figure 5.6b. The available data does not support a stable calculation of the power-law parameters in this case. The instability is due to a small sub-population of data centered at an effective distance (difference between epicentral distance for PKD and SAO) of 150 km. These data are due to an event that has a difference in azimuth between stations of 26° (white stars in Figure 5.1a). This effect illustrates a pitfall of this method whereby, although more data is made available, the paths to each station may not be along a narrow azimuth and will sample a structure that is different along paths and no longer directly between stations.

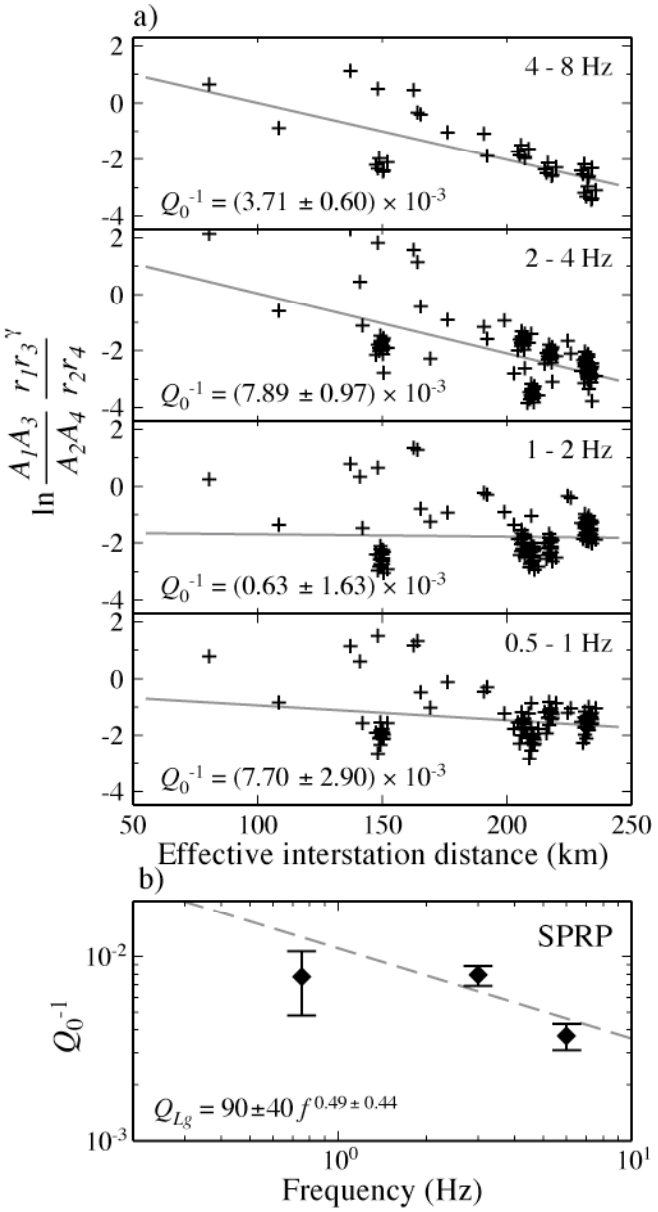


Figure 5.6. $Q_{Lg}$ for the path between stations PKD and SAO as measured by the source-pair/receiver-pair method. a) Robust regression of *Lg* amplitude ratios (crosses) versus effective distance where the spreading rate $\gamma$ is 0.5, and the bandwidth of the measurement is in the upper right. The slope is related to $Q^{-1}$, which is given in the lower left with standard error. b) Weighted regression of $Q^{-1}$ (diamonds with standard error bars) versus frequency bandwidth midpoint, where the power-law attenuation parameters with standard deviations are given in the lower left. The bandwidth between 1-2 Hz produced a very small slope, and thereby unrealistic $Q^{-1}$, so its value is not regressed and is absent in (b).

## 5.3 Method comparison

Since each method has a different data requirement it is inappropriate to compare the methods with the full dataset. For example, the CN method will sample geology at all back-azimuths relative to a station, whereas the RTS method is restricted to a narrow azimuthal window aligned roughly along a pair of stations and events. In an attempt to normalize the dataset used for each method, we restrict the data to lie in a small region along the Franciscan block (Figure 5.7a).

We implement all five methods to calculate $Q_0 f^n$ in the sub-region defined by Figure 5.7a using the Control parameterization given in Table 5.3 (Figure 5.7b). Equation (4) of the CN method is calculated and regressed for all epicentral distances in the sub-region. The $Q^{-1}$ and their standard errors are then put into a weighted least-squares as above, where the residuals are bootstrapped 1000 times to produce a population of power-law parameters. This population is then smoothed with a two-dimensional Gaussian kernel (Venables and Ripley, 2002) to produce an empirical probability density so that the 95% confidence region can be estimated. This 2-D technique is similar to the 1-D method of obtaining a probability distribution from a histogram of data. Equation (7) of the CS method is calculated for all event-station paths in the sub-region. In order to estimate the variability in the region, we create 1000 subsets of these paths by randomly selecting one member of each $Q$ population for a given discrete frequency band at all frequencies. This new subset is then least-squares fit in the log-domain to find the power-law parameters. We find the empirical distribution as described previously and estimate a 95% confidence region. A similar

method is employed for the TS and RTS methods. All $\alpha(f)$ from equations (9) or (11) are calculated for the sub-region and 1000 subsets are produced by randomly selecting one member of each $\alpha$ population for a given frequency. This subset is then fit with the same non-linear least-squares method as described above to produce an empirical distribution of power-law parameters where a 95% confidence region can be estimated. The SPRP method is carried out similarly to the CN method. This is a more appropriate implementation of this method, as compared to a single interstation path, since now a more even distribution of effective interstation distances can be used.

Figure 5.7b shows that the range in $Q_0$ (~30) and $\eta$ (~0.5) are similar for all methods, though the mean of the empirical population distribution is not always the same. This difference is most evident between the RTS and TS methods, as the the RTS method differs in the ability to remove the site terms. The different parameter means may suggest that the site term has a considerable effect on attenuation in the region, and this effect will be discussed below. Except for the TS method, all methods retrieve a similar mean $Q_0$, where the mean $\eta$ for the RTS method differs from the other methods by just ~0.15. Using the limits for all the methods, the 1-D model parameters in the region vary between 40 and 125 for $Q_0$, and 0.3 and 1.0 for $\eta$. The grey region in Figure 5.7b represents a parameter space that fits all method parameter distributions, where $Q_0$ is between 70 and 95, and $\eta$ is between 0.5 and 0.7.

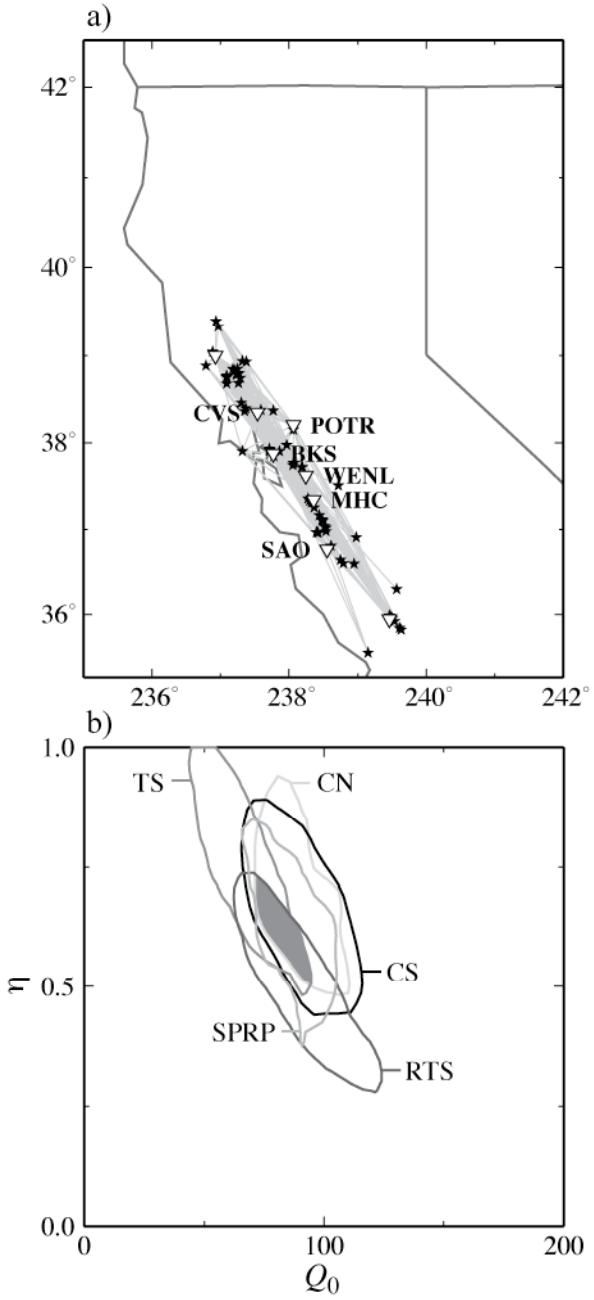


Figure 5.7. Method comparison. a) Map (same region as Figure 5.1) of the data subset used in the comparison analysis. Data are in a small region near the San Francisco Bay Area, primarily along the Franciscan block. b) Power-law parameters ($Q_0$, $\eta$) associated with each method; coda normalization (CN), coda-source normalization (CS), two-station (TS), reverse two-station (RTS), and source-pair/receiver-pair (SPRP). The empirical 95% confidence regions for each method are given. The intersecting region is shaded grey.

### 5.4 Sensitivity tests

Using the complete dataset, we investigated how the choice of parameterization affects the results. In each test, only one parameter was varied, and $Q_0 f^{\eta}$ was calculated with each of the methods. The varied parameters are geometrical spreading rate ($\gamma$), measurement bandwidth, epicentral distance, and the *Lg* window. The values of the varied parameters are listed in Table 5.3, where the range was chosen based on values used in previous studies.

For the CN method, standard error regions were constructed from the covariance of the power-law model parameters estimated by bootstrapping the residuals of the weighted least-squares fit 1000 times. Figure 5.8a shows the standard error regions for each test at station PKD. All tests cluster around the control parameters except the distance test (Test 3). To assess the significance of model parameterization differences one could find the average difference in the model parameters calculated with the control group versus the four tests and produce a mean change in $Q$ and $\eta$ ($\Delta Q_0$, $\Delta\eta$) for each of the four tests. However, to incorporate error in the calculated parameters we use a more sophisticated approach and perform an analysis of covariance (ANCOVA) for the weighted least-squares regression with Tukey's honest significant difference (HSD) pairwise comparison tests (Faraway, 2004). This pairwise comparison method finds a significant difference in the model parameters only if the 95% confidence region of the mean difference in the model parameters between the test and control does not include zero. The HSD test is more appropriate than a t-test when comparing more than one group, as is done here

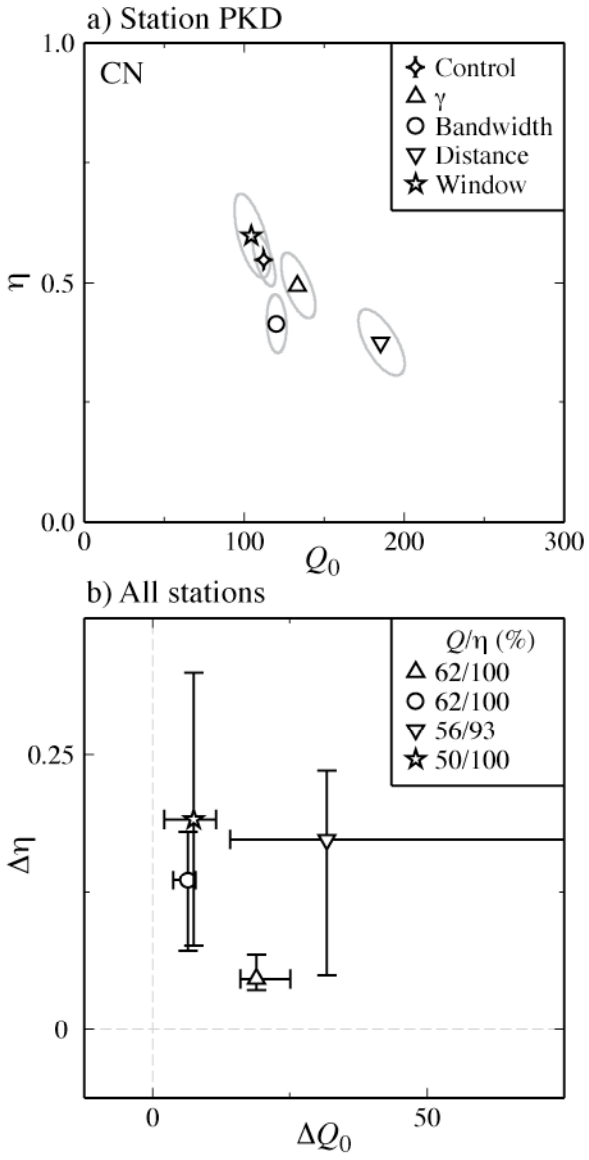


Figure 5.8. Parameterization effects of the coda-normalization method. a) Power-law parameters ($Q_0$, $\eta$) for each choice of parameterization and the standard error region using the example station as in Figure 5.7. b) Results of significant difference in pairwise comparisons between the control parameterization and tests (similar symbol as panel a) at all stations. The box in the upper right gives percentage of measurements that had a significant difference and the symbols are at the median difference ($\Delta Q_0$, $\Delta\eta$) with upper (3rd quartile) and lower (1st quartile) bounds given by the bars.

between the control and four tests. We group all significant differences between a given test and the control parameterization and plot the median and 25th and 75th

percentile values of that group, while noting the percentage of stations that had significant differences for each test (Figure 5.8b). In this way, we can try and separate aleatoric uncertainty due to poorly constrained power-law model parameters and epistemic uncertainty due to the choice of parameterization for each method. Therefore, the confidence regions in panel a) of Figures 5.8-5.12 can be interpreted as the aleatoric uncertainty, and the quartiles of $\Delta Q_0$ and $\Delta\eta$ in panel b) as epistemic uncertainty. There is a significant difference for almost all CN method comparisons in $\eta$, and the greatest difference for both model parameters is when the epicentral distance of the dataset is changed (Test 3). This is due to the fixed time $t_C$ at which the coda is measured, where for greater distances it may be more appropriate to increase $t_C$, or relate its value to the *S*-wave velocity.

Standard error regions and pairwise comparisons are calculated for the CS method as described above, though the residuals and ANCOVA are for a direct linear regression (Figure 5.9). For most Tests only a small fraction of the comparisons are significantly different. However, when γ is changed in equation (7) (Test 1) there is a significant difference in $Q_0$ for 39% of the path comparisons, where the median difference is almost 50. This effect highlights the difficulty in extracting an intrinsic $Q$ from the full path attenuation when examining a single path. The CS method is best for evaluating the total path term $P(f)G(r)\exp(-r\pi f/QU)$ from equation (1).

Since the TS and RTS methods require nonlinear regressions, we estimate covariance matrices from the bootstrapped power-law model parameter populations. ANCOVA is performed with this estimated covariance and the pairwise comparisons are made with the results (Figure 5.10-Figure 5.11). A change in epicentral distance

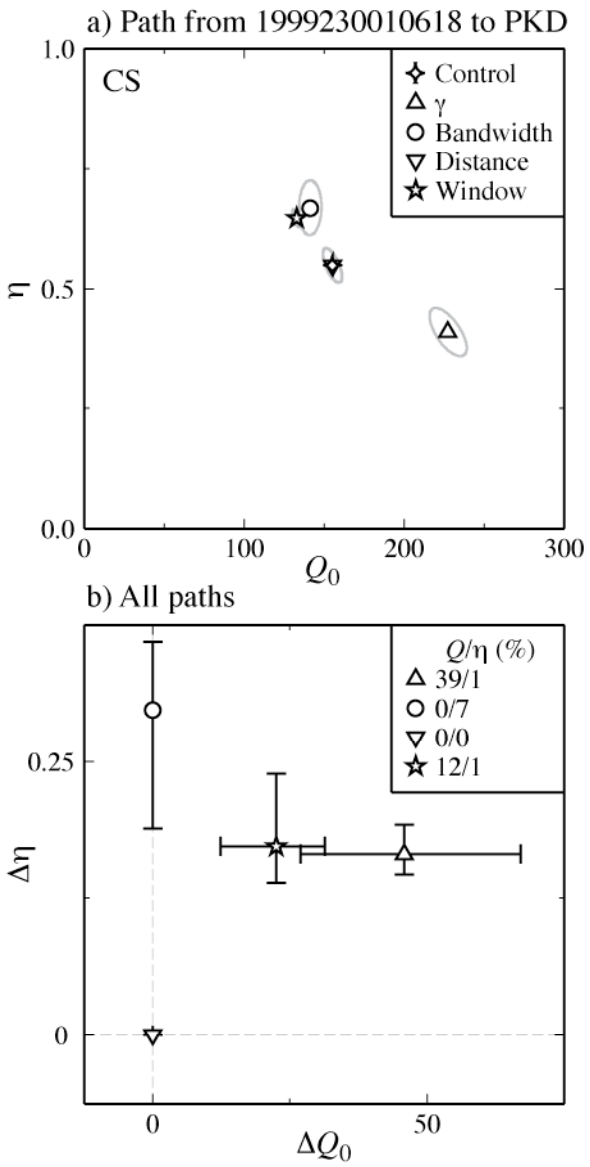


Figure 5.9. Parameterization effects of the coda-source normalization method. See Figure 5.8 for explanation, where a) is the same path as in Figure 5.3 and b) is for all paths.

does not significantly affect the power-law parameters for both the TS and RTS methods, but a change in bandwidth (Test 2) produces an interquartile range of 0.05 to 0.22 for the difference in $\eta$ using the TS method. The TS method is sensitive to site effects and this difference may be due to site effects that are different below 1 Hz than

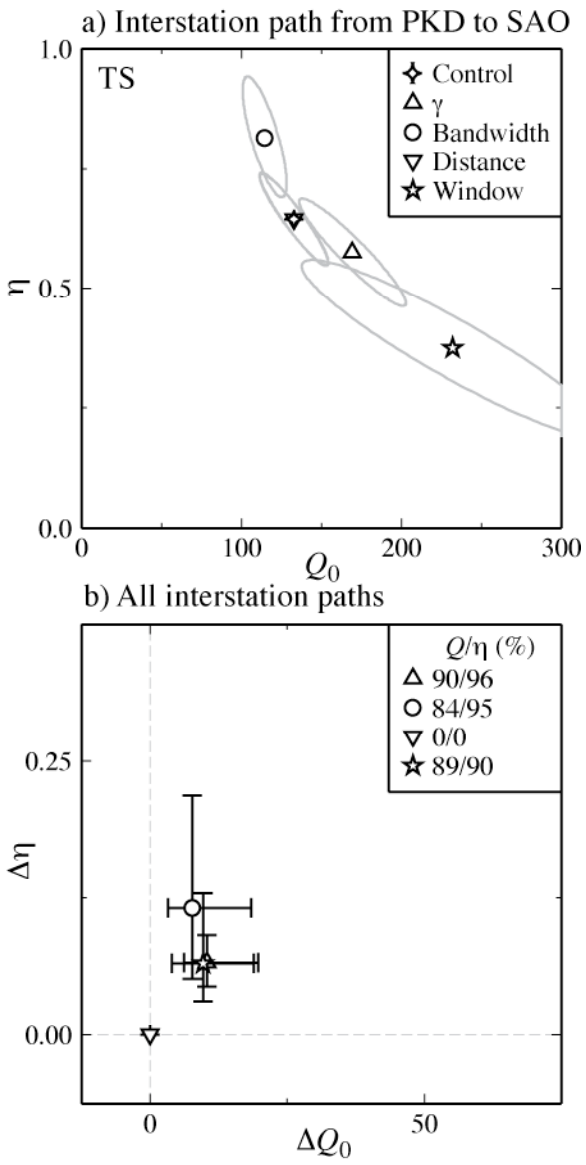


Figure 5.10. Parameterization effects of the two-station method. See Figure 5.8 for explanation, where a) is the same interstation path as in Figure 5.4 and b) is for all interstation paths.

they are above it. For several stations in the BDSN this seems to be the case (Malagnini et al., 2007). The RTS method doesn't suffer from this same dependency and its median significant differences are low for all Tests.

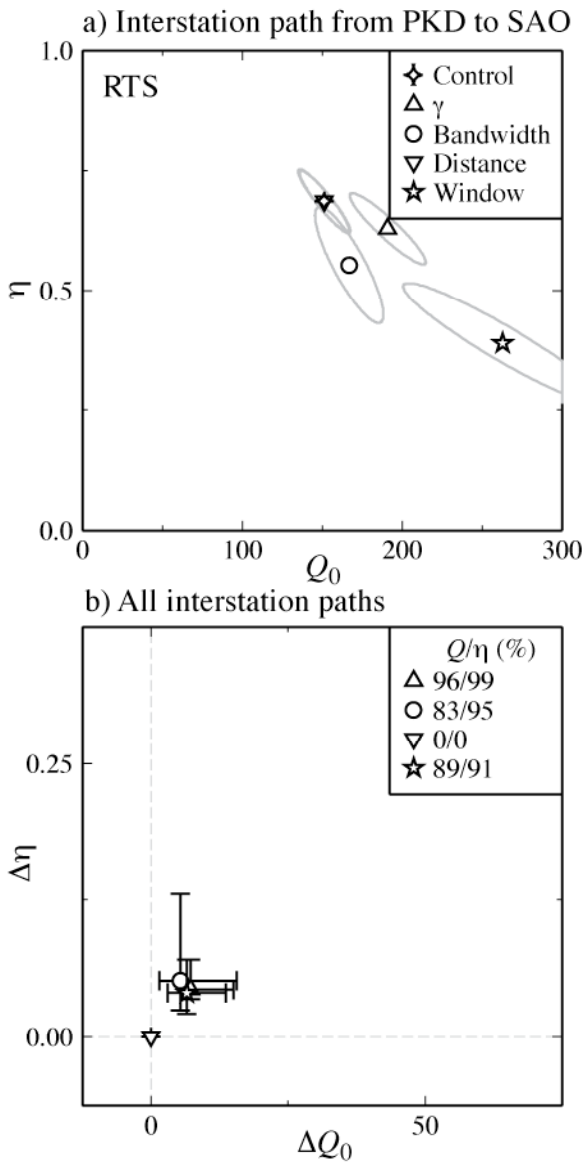


Figure 5.11. Parameterization effects of the reverse two-station method. See Figure 5.8 for explanation, where a) is the same interstation path as in Figure 5.5 and b) is for all interstation paths.

As previously stated, the SPRP method implemented in the time domain requires a distribution of effective interstation distances that can best be given when several interstation paths are considered. However, it should be able to constrain $Q_0 f^{\eta}$ for a single interstation path, and in order to allow for comparison with the

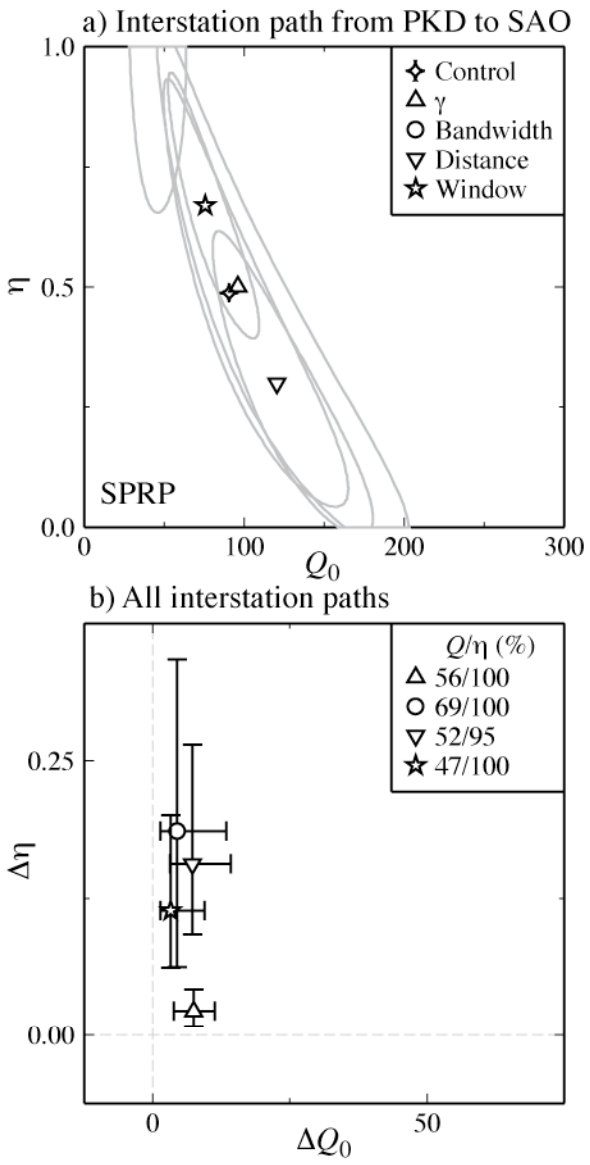


Figure 5.12. Parameterization effects of the source-pair/receiver-pair method. See Figure 5.8 for explanation, where a) is the same interstation path as in Figure 5.6 and b) is for all interstation paths.

implementation of the other interstation methods, TS and RTS, we carry out the method on an interstation basis. The effects of this suboptimal design are evident in the aleatoric error shown for the example path from PKD to SAO in Figure 5.12a, where the standard error regions are very large. Due to such large standard error

regions only approximately half of the pairwise comparisons give a significant difference in $Q_0$. However, the same comparisons reveal a large difference in $\eta$ for all but the $\gamma$ Test (Test 1).

### 5.5 Discussion

Each method analyzed here is employed for different types of investigations. Table 5.4 displays the advantages, disadvantages and assumptions of the methods. The CN method should produce a stable $Q$ measurement when the region near a station is homogenous, and could be easily implemented in a tomographic inversion scheme.

The CS method is designed to calculate an effective $Q$ for a given path, where the site term is mapped into the path attenuation. Also, since it measures the path directly from the event to station, there is a trade-off between geometrical spreading and effective $Q$. If the uncertainties in the type of geometrical spreading are large, then it may be best to test several forms of spreading, or to fold the spreading term into the entire path effect if this is appropriate for the application.

The TS and RTS methods are theoretically more stable due to the extraction of the source term. The RTS method produces the least error due to its additional extraction of the site terms, though it is more restrictive in its data requirements. Xie (2002) calculates the bias due to the site term assumption in the TS method and finds that it is small. In order to test this assumption and gain more insight to the differences present in Figure 5.7, we compare the power-law parameters calculated with the TS method for interstation paths with station BKS and those from a nearly co-located

Table 5.4. Method summary

| Method | Assumptions | Advantages | Disadvantages |
|---|---|---|---|
| CN | 1. Amplitude is measured at a point where coda scattering is homogeneous in space<br>2. Direct wave geometrical spreading is assumed | 1. Independent of source and site<br>2. Can use all event station paths | 1.Coda may not be homogeneous, or sensitive to source and site<br>2. Won't work when SNR too low to see coda |
| TS | 1. Source cancels when event to two stations azimuth is within 15°<br>2. Direct wave geometrical spreading is assumed | 1. Independent of source | 1. Paths are limited by the event station layout<br>2. Site effect differences between two stations can map into *Q* |
| RTS | 1. Path is identical when event to two stations azimuth is within 15°<br>2. Direct wave geometrical spreading is assumed | 1. Independent of source and site | 1. Paths are very limited by necessary event station layout |
| SPRP | 1. Path is identical when event to two stations azimuth is within a function that depends on distance.<br>2. Source radiation is isotropic | 1. Independent of source and site | 1. Least limiting of two station methods, but paths are limited to interstation |
| CS | 1. Direct wave geometrical spreading is assumed<br>2. Requires an independent method (e.g. coda) to obtain source spectrum | 1. Can use all event-station paths | 1. Short path attenuation very dependent on geometrical spreading assumptions |

BRK. Malagnini et al. (2007) find a significant difference in the site term between BKS and BRK and this difference is evident in Figure 5.13, where several of the paths do not fall along the *x=y* line. However, the difference in site effect between BKS and BRK is likely to be an extreme case for the BDSN, since BKS is located in highly fractured rock near the Hayward Fault.

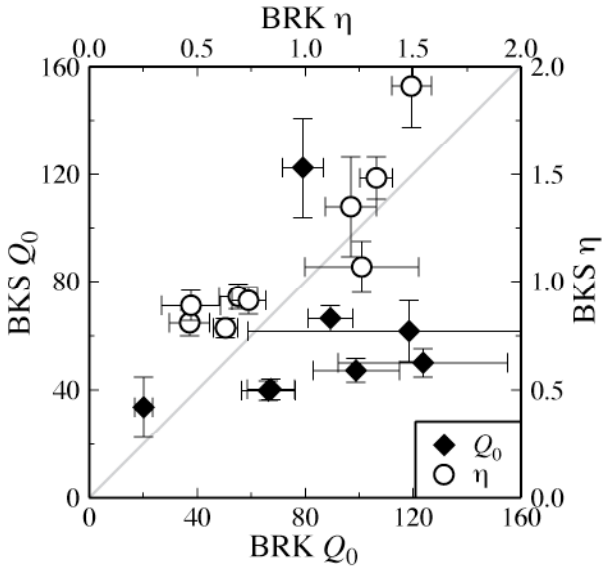


Figure 5.13. Comparison of power-law parameters for each interstation path that involves either station BRK (abscissa) or BKS (ordinate) measured with the TS method. Standard error bars are given for all parameters. If parameter values are similar they would fall along the grey line ($x = y$).

The SPRP method is the RTS method with a relaxation of the data requirements and is therefore only appropriate for very laterally homogeneous $Q$. The SPRP method is implemented in the frequency domain by Fan and Lay (2003b) and in the time domain by Shih et al. (1994) and Chung et al. (2005) where they find clusters in small regions that are very different from the overall 1-D $Q$ model. The SPRP method in the time domain is much better suited for a large homogeneous region, where several interstation regions can be grouped together. When interstation regions are not combined, a small amount of data near the true interstation distance can greatly affect the linear regression and produce large error in the model parameters. Such an effect can be seen in the example in Figure 5.6. However, this effect could be lessened by the use of a moving-average filter, though this could result in over-weighting some

points. The SPRP method requires the use of several interstation paths within a homogenous region, so a tectonically stable area is needed.

Much of the variation in 1-D power-law model parameters shown in Figure 5.7 may be due to structural heterogeneity in the region. In fact, a similar range in *Q* can be seen in the same Northern California subregion in Figure 5.2 of Mayeda et al. (2005). However, there are differences in the model parameter populations in Figure 5.7, and in order to fully understand epistemic uncertainty of a regional model we encourage the use of several methods to estimate parameters.

The parameterization choices can greatly affect the calculated power-law *Q* model. Therefore, knowledge of appropriate distributions of these parameters can help reduce the variance in the model and produce more realistic *Q* models. The geometrical spreading considered for a given method trades off with *Q* (Atkinson and Mereu, 1992; Bowman and Kennett, 1991). Nuttli (1973) and Campillo et al. (1985) model the geometrical spreading exponent ($\gamma$, in this study) in the time domain to be 5/6 (~0.83). However, Yang (2002) shows that a more appropriate time domain assumption when measuring the *Lg* rms amplitude is $\gamma = 1$. Spreading in the frequency domain is more stable and a value of 0.5 is a robust estimate, as suggested by Street et al. (1975) for distances greater than a given critical distance. Future work should use an appropriate range of spreading in the time domain and some distribution of $\gamma$ in the frequency domain.

The appropriate group velocity window can also affect the 1-D *Q* model. Campillo (1990) uses synthetic tests to show that earlier energy in a given *Lg* window samples the shallow crust, whereas later arriving *Lg* energy has s

ampled a larger portion of the crust. Producing power-law $Q$ from a range of windows within the observed *Lg* energy window could illuminate this effect and aid in the derived model interpretation.

## 5.6 Conclusions

We apply the coda normalization (CN), two-station (TS), reverse two-station (RTS), source-pair/receiver-pair (SPRP), and the new coda-source normalization (CS) methods to measure $Q_{Lg}$ and its frequency dependence ($Q_0 f^{\eta}$) in northern California in order to understand the variability due to parameterization choice and method used. We investigate the reliability of the methods by comparing them with each other for an approximately homogeneous region in the Franciscan block near the San Francisco Bay Area. All methods return similar ranges in power-law parameters when considering the 95% confidence regions. The joint distribution using all methods gives $Q_0 = 85 \pm 40$ and $\eta = 0.65 \pm 0.35$ (both ~95% CI). However, the centers of the RTS and TS method distributions differ from each other, though the mean $Q_0$ of the RTS method is similar to those of the other three methods. This may be due to the removal of the site terms for the RTS method, which suggests that in cases where the site effects are not uniform within a region several 1-D methods should be employed to assess the full range of models.

We test the sensitivity of each method to changes in geometrical spreading, *Lg* frequency bandwidth, the distance range of data, and the *Lg* measurement window. For a given method, there are significant differences in the power-law parameters, $Q_0$

and $\eta$, due to perturbations in the parameterization when evaluated using a conservative pairwise comparison. The CN method is affected most by changes in the distance range, which is likely due to its fixed coda measurement window or the fact that at larger distances the coda is not homogeneously distributed. Since the CS method is best used to calculate the total path attenuation, it is very sensitive to the geometrical spreading assumption. The TS method is most sensitive to the frequency bandwidth, which may be due to its incomplete extraction of the site term. The RTS method is insensitive to parameterization choice, whereas the SPRP method as implemented here in the time-domain for a single path has great error in the power-law model parameters and $\eta$ is greatly affected by changes in the method parameterization. When presenting results for a given method it is best to calculate $Q_0 f^n$ for multiple parameterizations using an *a priori* distribution.

# Chapter 6

# Local Magnitude Tomography in California

## 6.1 Introduction

An understanding of regional attenuation can help when interpreting of tectonic features, especially their thermal structure and water content. These features have a greater influence on attenuation than velocity, which is more commonly measured. The calculation of laterally varying (two-dimensional, 2D) attenuation can also help to constrain earthquake parameters that depend on amplitude like event magnitude. Previous studies of attenuation in California have been made for one-dimensional (e.g., Erickson et al. (2004); Ford et al. (2008)) and 2D (e.g., Mayeda et al. (2005); Phillips and Stead (2008)) cases.

Inspired by the work of Pei et al. (2006), we perform an $M_L$ tomographic study of California and invert the amplitudes for source, site and path effects. We make use of recent work to recalibrate the CISN local magnitude ($M_L$) scale (Hellweg et al. (2007)). The project required the calculation of Wood-Anderson amplitudes measured at stations of the CISN for a good distribution of earthquakes, which resulted in over 30,000 amplitude measurements. $M_L$ tomography provides a unique data set and perspective for examining the crust and attenuation in the frequency band that affects

ordinary structures. We discuss the resultant terms and assess their significance in relation to California tectonics and the measurement of $M_L$.

## 6.2 Data and Method

The $M_L$ recalibration study for the CISN (Hellweg et al. (2007)) used events with catalog $M_L \geq 3.0$ that occurred between 2000 and 2006, and in order to get an even distribution, the largest event in a 50 km grid was selected. In an attempt to obtain more recent measurements, a second pass along this grid was made for events that occurred in 2006. This resulted in more than 200 events. Data at distances between 1 and 500 km from these events measured on the horizontal components was obtained from over 300 strong-motion and broadband stations of the northern and southern California networks, as well as some data from temporary deployments of the USArray. The Wood-Anderson seismograph response of these data were calculated (Uhrhammer et al. 1996) and the maximum amplitude on the trace was measured.

For this study, in order to obtain a more even magnitude distribution, data for events with M>5.5 were discarded. All events were recorded at more than one station. Also, if there was more than one east or north component, they were averaged so that each station had exactly two horizontal measurements, so as not to inadvertently weight the data when there are more observations at a station. These criteria resulted in 185 events recorded at 335 stations (670 components) for 25330 amplitude measurements, which produced a very dense sampling of California (Figure 6.1a).

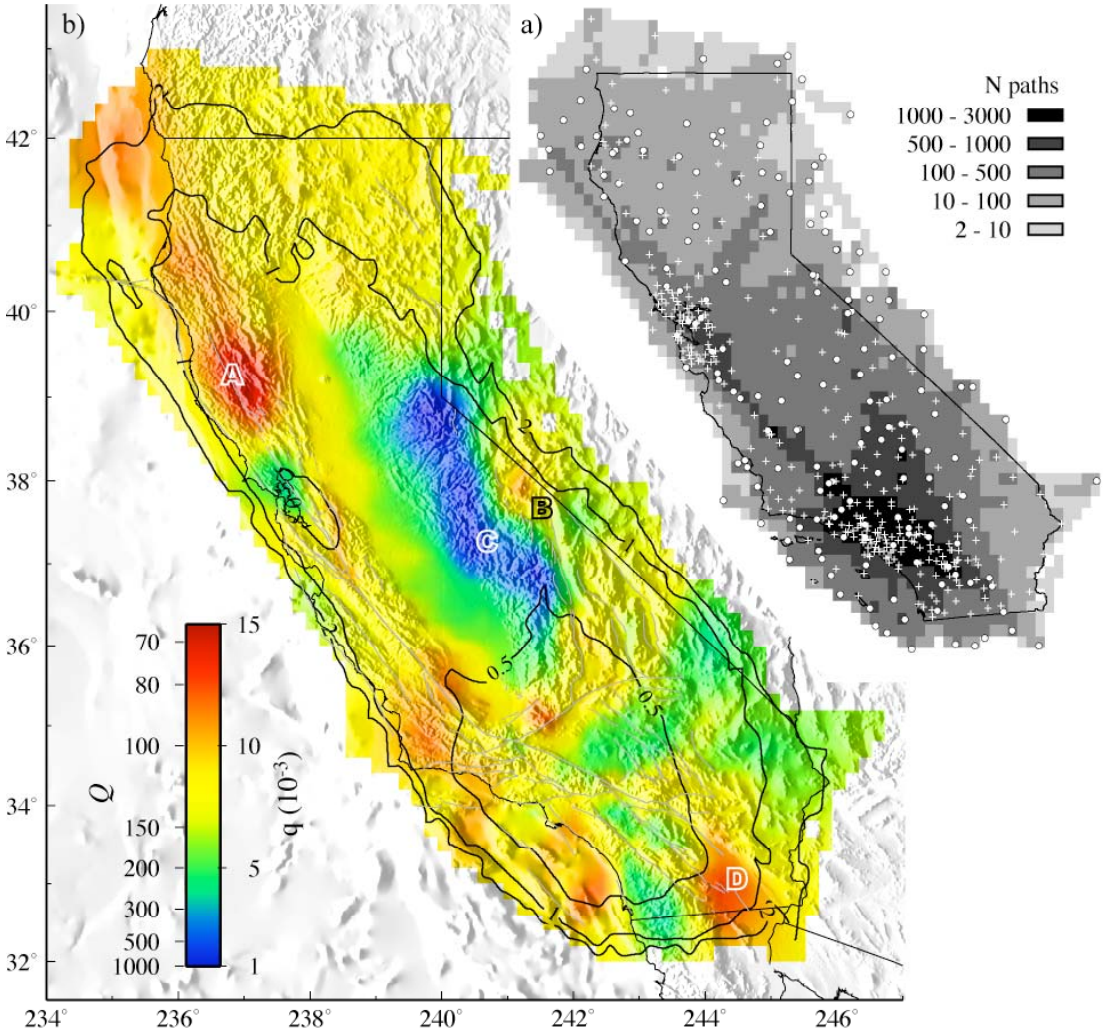


Figure 6.1. a) Inset, data coverage map of California, where grid nodes (0.2$^{o}$) are shaded according to number of paths crossing them. Events (circles, N=185) and stations (inverted triangles, N=335) used in the analysis are also shown. b) Local magnitude tomography of California. The scale is given in Q, and q (1/Q), where hot colors (red) are high attenuation and cool colors (blue) are low attenuation. Regions discussed in text are annotated: A) Geysers, B) Long Valley, C) Sierra Nevadas, D) Salton Trough.

We employ the tomography method of Phillips and Stead (2008) where the Wood-Anderson amplitude $A_{WA}$ at a given distance $r$ and frequency $f$ can be estimated by

$$A_{WA}(f,r) = S(f)R(\theta)P(f)G(r)\exp\left(\frac{-r\pi f}{QU}\right), \quad (6.1)$$

where $S(f)$ is the source spectrum and $R(\theta)$ is the source radiation in the source-receiver direction $\theta$. $P(f)$ is the site term, and $G(r)$ is the geometrical spreading term. The final term is an apparent attenuation (parameterized by $Q$), where $U$ is the group velocity of the phase that produces the amplitude measurement. This phase is often *Sg* at short distances and *Lg* at greater distances, therefore we assume $U$ is approximately 3.5 km/s.

The log transform of eq (1) is

$$\log[A_{WA}(f,r)] = \log[S(f)] + \log[R(\theta)] + \log[P(f)] + \log[G(r)] - \frac{r\pi f}{QU} \quad (6.2)$$

We adopt a geometrical spreading term from Street et al. (1975) of the following form

$$G(r) = \begin{cases} \frac{1}{r} & r < r_0 \\ \frac{1}{r_0}\left(\frac{r_0}{r}\right)^{0.5} & r \geq r_0 \end{cases}. \quad (6.3)$$

The distance $r_0$ as well as a starting 1D $Q$ model for California, were found by fitting the amplitude decay function ($\log A_0$) used in southern California (Kanamori et al., 1999),

$$\log A_0(r) = 1.11 \cdot \log(r) + (0.00189r) + 0.591, \quad (6.4)$$

which is very similar to the CISN $\log A_0$ calculated by Hellweg et al. (2007), which will be used for all of California. The best fit was given by $r_0$=200 and $Q$=150 (Figure 6.2), so that the spreading transitions from body-wave ($r^{-1}$) to surface-wave ($\sqrt{r}$) at approximately 200 km. We validate the assumption of an approximately isotropic radiation pattern (Figure 6.3) so that $R(\theta)$ can be approximated by a constant and the

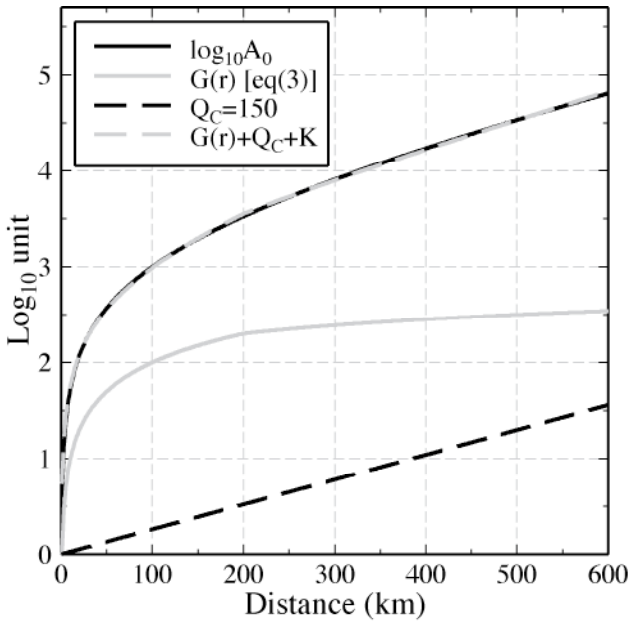


Figure 6.2. Amplitude decay and attenuation functions. Dark solid line is the log$A_0$ used in southern California (Kanamori, 1999), which is very similar to one derived for all of California (Hellweg et al, 2007). Dashed line is the geometrical spreading function given in eq (3). Light solid line is a constant $Q$ of 150 and dashed light line is the combination of the geometrical term and the constant $Q$ plus K=0.73.

amplitudes can be corrected using eq (3) and an initial $Q$ model, then eq (2) can take the form

$$\log[A_{WA}(f_{WA})] = \log[S(f_{WA})] + \log[P(f_{WA})] - \frac{\pi f_{WA}}{U}\int_s Q^{-1} ds \qquad (6.5)$$

where $f_{WA}$ is the frequency band of the synthetic Wood-Anderson amplitudes, which can be approximated as a two-pole highpass Butterworth filter with a corner at 1.25 Hz (Uhrhammer and Collins, 1990), and is assumed to be approximately 1 Hz in the analysis. The form is put into a damped first-difference least-squares inversion (LSQR, Paige & Saunders, 1982) to calculate the source, site, and path terms in the Wood-Anderson band along the incremental ray length, $s$. We chose a damping

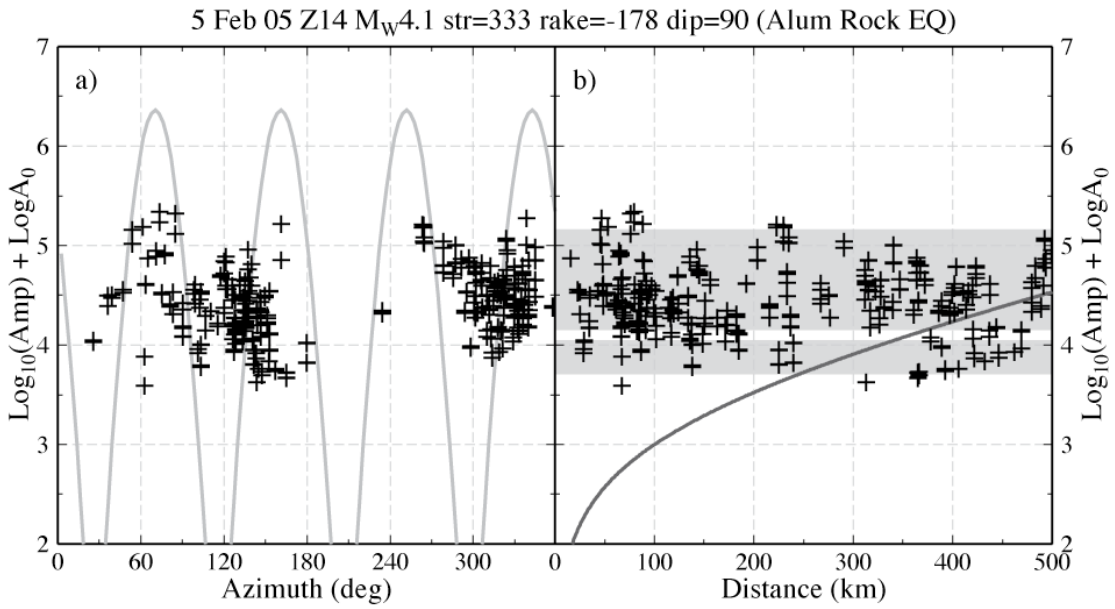


Figure 6.3. Corrected amplitude variation with a) azimuth and b) distance for the 5 Feb 05 Alum Rock ($M_W$4.1) earthquake. The SH radiation pattern of the event is plotted in a) and the Kanamori et al. (1999) log$A_0$ is plotted in b) (for which the amplitudes have been corrected). The gray region in b) is the mean magnitude (4.43) ± 2$\sigma$ ($\sigma$=0.36), where the white line is the calculated $M_W$. The catalog $M_L$ for this event is 4.42.

coefficient of 150 and a grid-spacing of 0.2$^o$ based on an L-curve analysis, where these 2 choices minimized the model length and residual variance satisfactorily (Figure 6.4).

## 6.3 Results and Discussion

The event terms agree well with catalog magnitudes (Figure 6.5). The difference between the event terms and catalog magnitudes (event bias) are centered on zero with a standard deviation of 0.25. Site terms agree very well with station corrections, or station-network-component-location (SNCL) d$M_L$s (Figure 6.6). These SNCL d$M_L$s are obtained from a separate L-1 norm inversion (Hellweg et al., 2007),

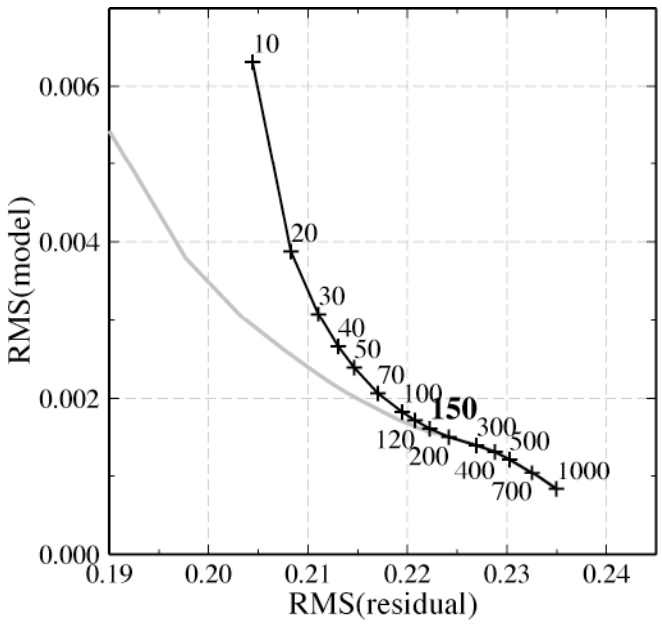


Figure 6.4. L-curve analysis, where the damping coefficient used in the inversion that produced the model and residuals is given for grid spacing of 0.2°. The gray line is for a grid spacing of 0.1o. A damping coefficient of 150 was selected (bold type) because it minimizes the root-mean-square (RMS) of the model and residual.

which required historical corrections to be maintained in the current algorithm. The constraint is evident in the SNCL $dM_L$ histogram, which is shifted off a mean of zero. There are several outliers in this comparison. Two positive term outliers are the Transportable Array (TA) stations, P05C and R05C on the north and east components, respectively. This may be due to the small number of observations made during this temporary installation (ten and five, respectively). The negative term outliers (gray ellipse, Figure 6.5) each have more than sixty observations, but they are all located near the Long Valley region (Region B, Figure 6.1b). If the SNCL $dM_L$s are correct, then the path term in this region is under-predicted, which would result in a greater q (higher attenuation) in this area.

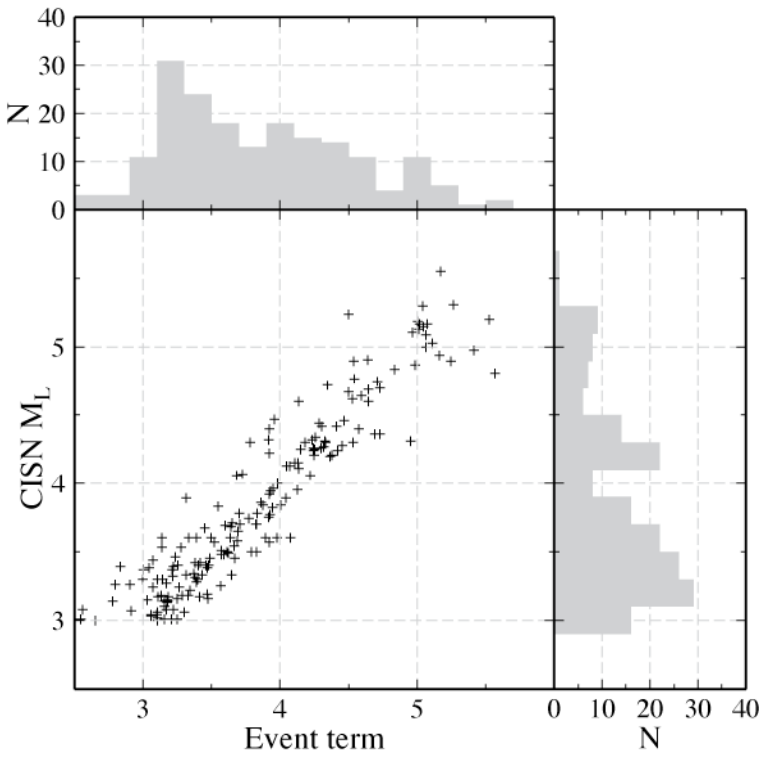


Figure 6.5. Event term compared to catalog magnitude (CISN ML). Histograms along the axes show the distributions of the event terms (top) and catalog magnitudes (right). The event terms from the inversion agree well with the catalog magnitudes.

Resolution of the path term is calculated via direct solution of the normal equations using Cholesky decomposition and the resolution length is estimated by taking the square root of the ratio of grid area to diagonal resolution element (Phillips and Stead, 2008). This length is contoured in Figure 6.1a and is highest in southern California at $0.5^o$, but resolution of $1^o$ is found for most of California.

*Q* is derived from the path term and ranges from 66 to a little more than 1000 in California. Its inverse, q, is directly related to attenuation and correlates well with geological and topographical regions (Figure 6.1b). Attenuation is high in the geothermal regions of The Geysers, Long Valley, and the Salton Trough (A, B, and D,

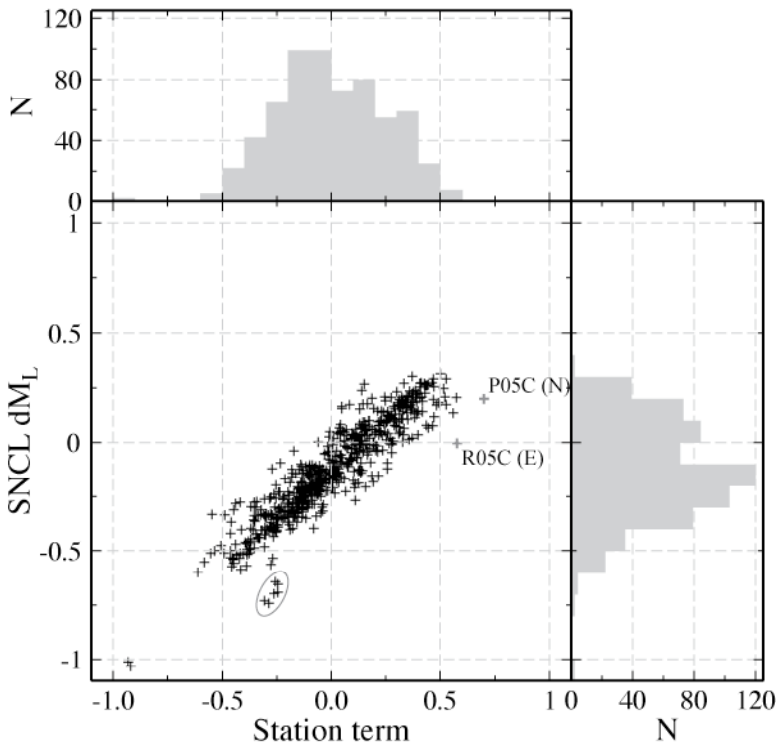


Figure 6.6. Station term compared to regression result for station-network-component-location (SNCL) dML. Histograms along the axes show the distributions of the station terms (top) and the SNCL dMLs (right). The station terms agree well with the regression result, but the mean is shifted toward zero (as prescribed by the inversion). Two outliers (gray crosses) with a small number of observations are annotated and another cluster of outliers is shown by the gray ellipse.

respectively, Figure 6.1a) and low in the Sierra Nevada batholith (C, Figure 6.1a). As discussed earlier, we may expect q in the Long Valley region to be even greater. There is a slight suggestion that faulting is associated with high q regions. This is most evident along the Garlock Fault (latitude=35$^o$) and possibly the Hayward Fault system (latitude=37.5$^o$, longitude=-121.8$^o$). One of the most unexpected features of the tomogram is the relatively low q region in the San Francisco Bay Area, and several validation tests prove it to be a robust feature. Though absolute *Q* in this region (*Q*~200) agrees with Mayeda et al. (2005) and the 1-D model for the Bay Area of

Malagnini et al. (2007), it differs from previous work by Ford et al., (2008) ($Q$~100). The reason for the discrepancy may be associated with the tectonics of the region. Ford et al. (2008) were careful only to measure attenuation in the Franciscan block (west of the San Andreas Fault), however this study uses paths that traverse both the Franciscan and Salinian blocks (east of the San Andreas Fault). In fact, Phillips et al. (1988) found a distinct difference in coda $Q$ for the two regions, and though the absolute values are different between this study and their results, the ratios of the regions are similar. Furthermore, there is a suggestion in the results of Phillips and Stead (2008) that attenuation in this region may be lower relative to its surroundings.

The path term could act as a third correction for $M_L$ in addition to the $\log A_0$ and SNCL dML corrections that are already applied when calculating $M_L$ in California. However, the path correction is an order of magnitude smaller than the $\log A_0$ and SNCL $dM_L$s (0.01 versus 0.1, respectively). Though, the effect of extreme Q structure in regions like the Sierra Nevadas, The Geysers, and the Salton Trough may be large enough to warrant a path correction for sources affected by those regions.

Random error will not greatly affect the results presented here due to the excellent ray coverage and the damping used in the inversion. However, the assumptions employed here, namely isotropic radiation, and straight-line wave propagation that samples the crust will introduce systematic error into the interpretation. The isotropic radiation assumption may affect the data at short (<100 km) distances where the normalizing effects of scattering and dispersion do not play a large role, whereas the wave propagation assumption may affect the data at long (>300

km) distances where the measured amplitude may belong to a diving wave that has sampled the upper mantle. Finally, it is difficult to comment on intrinsic attenuation of crustal material in California because this method measures a path q that is a combination of both intrinsic and scattering attenuation.

### 6.4 Conclusion

We use of over 25,000 amplitude measurements made to recalibrate $M_L$ in California to derive *Q* from the path term of an amplitude tomography method, which also solves for perturbations to the site and source terms. Source terms agree well with initial CISN $M_L$s and site terms agree well with a prior regression analysis. *Q* ranges from 66 to 1000 with an average of 143. The average *Q* is consistent with an amplitude decay function ($\log A_0$) for California when combined with a simple geometrical spreading rate. Attenuation in California is consistent with the tectonic structure of California, with high *Q* in the Sierra batholith and low *Q* at The Geysers, Long Valley, and Salton Trough possibly due to geothermal effects. There is also increased attenuation along shear zones with active faulting. Our results in the San Francisco Bay Area agree with the 1-D analysis of Malagnini et al. (2007) and 2-D study of Mayeda et al. (2005). A more complete *Q* model may aid in ground motion estimates for California. Finally, path terms are an order of magnitude smaller than site and source terms, suggesting that they are not as important in correcting for $M_L$

# Chapter 7

# Attenuation tomography of the Yellow Sea / Korean Peninsula from coda-source normalized and direct Lg amplitudes

## 7.1 Introduction

Understanding of regional attenuation (1/*Q*) can help with structure and tectonic interpretation (e.g., Frankel, 1990), and correcting for the effects of attenuation will improve source parameter studies, which will aid in discrimination of small nuclear tests (e.g., Baker et al., 2004; Mayeda et al., 2003; Taylor et al., 2002). Current event identification schemes rely on *Q* models that are derived differently, and the models can vary greatly for the same region. In previous work (Ford et al., 2008), we compared 1-D methods to measure $Q_{Lg}$ and attempted to assess the error associated with the results. The assessment showed the possible influence of lateral variations in attenuation, and in order to understand its importance, we perform inversions for 2-D attenuation in the Yellow Sea/Korean Peninsula (YSKP). In the same spirit as the comparison of 1-D methods, we compare three 2-D methods using the identical data. The comparison is made for the source, site, and path parameters. Comparison of solutions obtained with different methods can give insight to the model error, which is often much more important and larger in magnitude than any type of random error that is often calculated for inverse studies. In the section that follows we will outline the

amplitude tomography method of Phillips and Stead (2008) and the source-interpreted amplitude tomography method of Pasyanos et al. (2009). We will also introduce the coda-source corrected amplitude tomography method, which is a 2-D implementation of the 1-D analysis presented in Walter et al. (2007). Finally, the attenuation structure of the YSKP will be interpreted in terms of tectonics of the region.

## 7.2 Data and Method

The YSKP dataset consists of 145 earthquakes recorded at 6 broadband (20 sps) three-component stations of the global seismographic network (GSN) and OHP-Japan (station TJN) networks (Figure 7.1). We omitted data with paths that traverse the Sea of Japan / East Sea, since this region is an efficient Lg blockage zone (Knopoff et al., 1979). Using this data, we implement the amplitude tomography method of Phillips and Stead (2008), which assumes the spreading-corrected Lg spectrum ($A_{\mathrm{Lg}}$) at a finite frequency $f$ can be represented as,

$$\ln(A_{\mathrm{Lg}}) - \ln(G(r)) = \ln(S(f)) + \ln(P(f)) - \frac{\pi f}{U}\int_s Q^{-1} ds \ , \qquad (7.1)$$

where $U$ is the phase velocity, and is assumed to be 3.4 km/s. The inversion solves for $S(f)$ and $P(f)$, the source and site terms, respectively, as well as $Q^{-1}$ along the path, $s$, in a damped least-squares sense with first-difference regularization using the LSQR algorithm (Paige and Saunders, 1983). The mean of the log site terms is damped to zero and the spreading correction is done using the Street et al. (1975) function

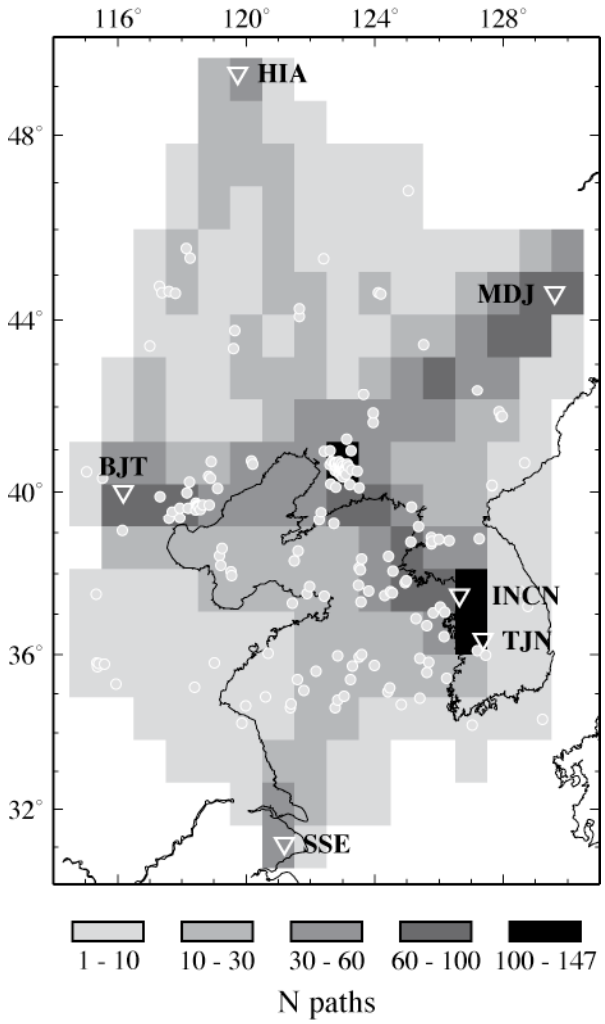


Figure 7.1. YSKP region with events (circles), stations (inverted triangles), and path density (grayscale) for the data used in this study.

$$G(r) = \begin{cases} r^{-1} & \text{for } r < r_0 \\ \frac{1}{r_0}\left(\frac{r_0}{r}\right)^{\gamma} & \text{for } r \geq r_0 \end{cases}, \tag{7.2}$$

where $\gamma$ is 0.5 and $r_0$ is 100 km. Therefore, spreading transitions from a body-wave to a surface wave type at approximately 100 km. Ford et al. (2008) found that results differed only slightly when $r_0$ is between 60 and 120 km. This method will be called AMP as in amplitude. We also employ a new method, which alters the previously

described method so that the amplitude is directly corrected for the source using stable, coda-derived source spectra (Walter et al., 2007). In this implementation the site term is completely free and source spectra derived from the coda are calculated via the methodology of Mayeda et al. (2003). This method will be referred to as CS for coda source. Damping was chosen on the basis of L-curve analysis, where the final damping parameter minimized both the model length and error. We also implement the method of Pasyanos et al. (2009), which is similar in form to the AMP method, but uses a starting source term based on seismic moment as defined in the Magnitude Distance Amplitude Correction (MDAC) formalism (Walter and Taylor, 2001). This source term is a modified corner-frequency model with frequency-squared falloff incorporating seismic moment, apparent stress, and source-region geophysical parameters. Also, this method also uses second-difference regularization, as opposed to the first difference regularization used by AMP and CS. In this way, the output source terms are perturbations to the original source, and the source term has a better physical interpretation. This method will be referred to as SI for source interpretation. A grid spacing of 1° was used for all methods due to the relatively small dataset and to facilitate comparison.

Data collection starts with analyst reviews each seismogram. The beginning of the Lg window is defined by the analyst pick, or when a pick is not available, the group velocity 3.45 km/s. The end of the window is defined by the group velocity 2.8 km/s, and the minimum window length is 1 sec. These windows are used to measure time-domain RMS amplitudes, which are converted to pseudo-spectral amplitudes in the passband of 1-2 Hz via the method of Taylor et al. (2002). Amplitudes are kept if

the pre-event signal-to-noise ratio (SNR) exceeds two. A pre-phase SNR test resulted in only a few less amplitude measurements and was not used, unlike Pasyanos et al. (2009).

### 7.3 Results and Discussion

In the remaining sections attenuation will be discussed in terms of $q$ which is defined as $Q^{-1} \times 10^{-3}$, and is linearly related to attenuation so that high q means high attenuation and low q means low attenuation. $q$ values will also be translated to $Q$ to facilitate comparison with other studies. $q$ from the path term of the new CS method is shown in Figure 7.2. Attenuation derived with all methods is a total path attenuation, which will have components of both scattering and intrinsic attenuation, and we make no attempt to separate the two. Figure 7.2 shows attenuation that is correlated with topography (low $q$ in the Da-xin-an-ling and Changbai Mts.) and sediment thickness (high $q$ in the Bohai Bay and Songliao Basin), where there is a transitional region along the Yellow Sea / West Sea from high $q$ in the west, a region of thick sediments, to low $q$ in the east along the Korean coast. $q$ in the entire YSKP ranges from 0.95 ($Q$ = 1048) to 3.63 ($Q$ = 275). Resolution of the path term is calculated via direct solution of the normal equations using Cholesky decomposition and the resolution length is estimated by taking the square root of the ratio of grid area to diagonal resolution element (Phillips and Stead, 2008). This length is contoured in Figure 7.2 and is approximately 3° in most of the YSKP, and where there are no crossing rays, no $q$ is plotted.

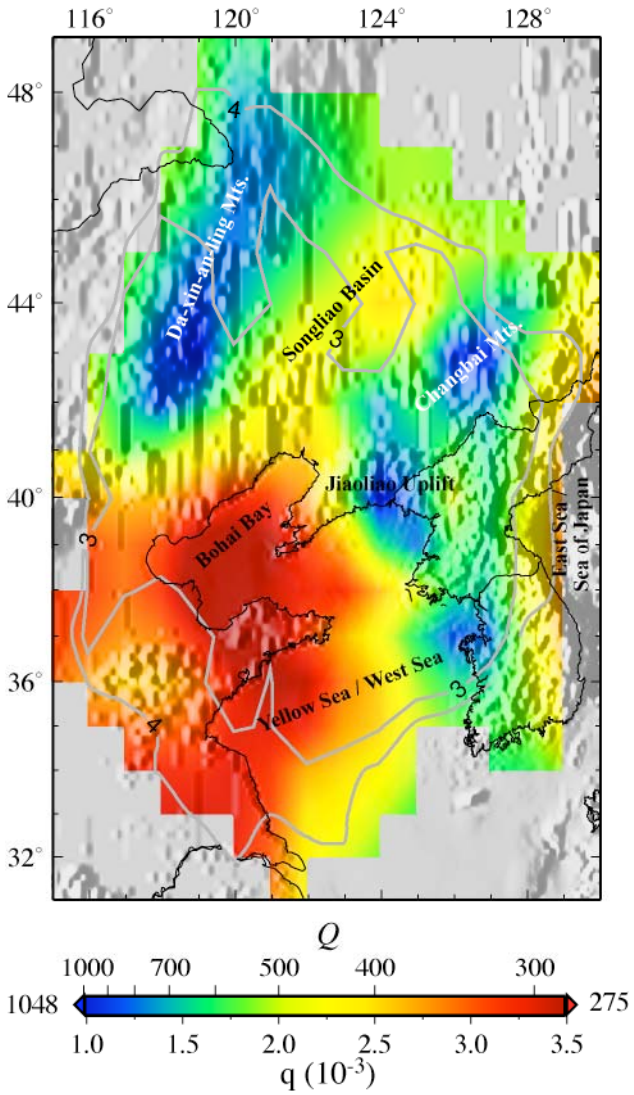


Figure 7.2. Coda-source corrected amplitude tomography of the YSKP region plotted on grayscale topography. The color scale is linear in q (1/*Q*) with the minimum (275) and maximum (1048) *Q* shown. Resolution contours of 3° and 4° are also plotted and only regions with crossing raypaths are imaged. Regional features are annotated and discussed in the text.

The source terms are compared amongst each other and with $M_W$ in Figure 7.3 (panels northeast of dashed diagonal line), where $M_W$ is either a coda-based magnitude or has been derived from a source inversion. All methods correlate well with $M_W$ (top row, Figure 7.3). The CS method does not invert for the source, so the values given in

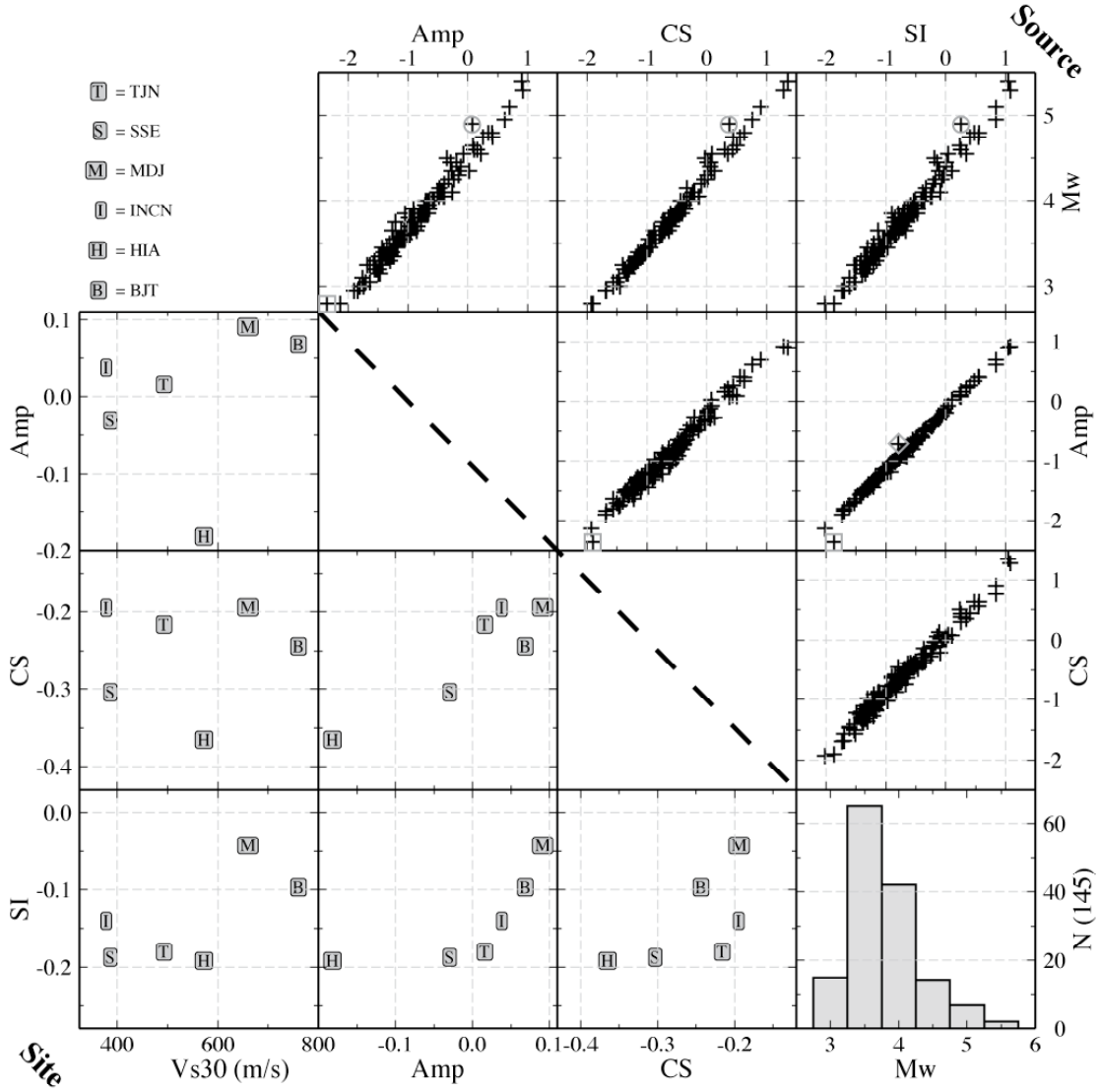


Figure 7.3. Source and site term comparison of the amplitude tomography method (Amp), and coda-source corrected (CS) and source-interpreted (SI) versions of that method (see text for descriptions of the methods). Source comparison is shown the upper triangle (plots northeast of the thick dashed black diagonal line) where Mw is from either a coda-source measurement or source mechanism inversion and a histogram of their values is in the southeast corner. Outliers are marked and discussed in text. All panels share the same range. Site comparison is the lower triangle (plots southwest of the thick dashed black diagonal line) where Vs30 are values from Wald and Allen (2008) and points are given by station names (legend in northwest corner). The absolute range of the panels is the same, though the minimum and maximum may vary slightly to facilitate comparison. Values are in log units (unless otherwise noted), though the SI and CS event terms in log amplitude of the source spectra.

Figure 7.3 are the source terms used to correct the data for this method, so as expected, these source terms agree best with catalog $M_W$. There is an outlier common to all methods that is circled in Figure 7.3. This event has a catalog magnitude of 4.9, but a recent source inversion of this event calculated an $M_W$ of 4.7. Therefore, this outlier may be due to an incorrect catalog magnitude, which shows that the SI method is able to correct for small errors in the initial source term. Also, as expected, the source terms of the AMP and SI method are very similar (2nd row, 4th column, Figure 7.3) except for two outliers that are marked with a diamond and square. These two events are very near one another and located just south of station TJN (Figure 7.1), which is a region of very low attenuation (Figure 7.2). The outlier marked with a square is an outlier for all AMP comparisons, and is the smallest event in the dataset.

The site terms are compared amongst each other and with Vs30 in Figure 7.3 (panels southwest of dashed diagonal line), where Vs30 for each station is taken from the topography-derived database of Wald and Allen (2008). There is very little correlation between the site term from the different methods and Vs30 (first column, Figure 7.3), though there is a slight positive correlation with the SI method. The site terms of the CS and Amp method correlate fairly well (3rd row, 2nd column, Figure 7.3), except for an absolute shift that is probably due to the constraint of the Amp method that requires the mean of the site terms to be zero. The site terms of the SI method agree well with the other methods (bottom row, Figure 7.3), except for the site terms due to INCN and TJN. These stations are relatively close to one another and in a region of very low attenuation (Figure 7.2).

The path terms are compared amongst each other and with sediment thickness (Laske and Masters, 1997) in Figure 7.4. The panels along the diagonal of Figure 7.4 are the 2-D path terms for each method, and sediment thickness is plotted in the upper-left panel. The image produced with the CS method (panel K, Figure 7.4) is the same as in Figure 7.2 without bilinear interpolation of the values. Panels to the northeast of the diagonal are a grid point by grid point comparison of q values from each method as well as sediment thickness. There is a slight positive correlation with sediment thickness that is mostly due to regions of thickest sediment, which can be seen by looking at the panels to the southwest of the diagonal. These panels are 2-D plots of normalized percent difference *NPD* between two path terms, *A* and *B*. To make these plots we first normalize the *q* (or sediment) maps to unity and then find

$$NPD_{ij} = \frac{2\left|A_{ij} - B_{ij}\right|}{A_{ij} + B_{ij}} \cdot 100, \tag{7.3}$$

which is the absolute difference between two points divided by their average. For example, the *NPD* between all methods and sediment thickness (panels E, I, M) is lowest in the Bohai Bay region, which means that this is where they are most similar. The grid point by grid point *q* of all the methods (panels G, H, L) correlates well, especially between the CS and AMP method (panel G). However, there is high *NPD* along the Da-xin-an-ling Mts. (panel J), which is a region with few crossing paths (Figure 7.1), so the CS method may be better at resolving structure that is poorly sampled. This performance difference may be due to a reduction of the null space gained in the elimination of the source term as a model parameter (Menke et al., 2006). The comparison with the SI method has more scatter (panels H, L) and this

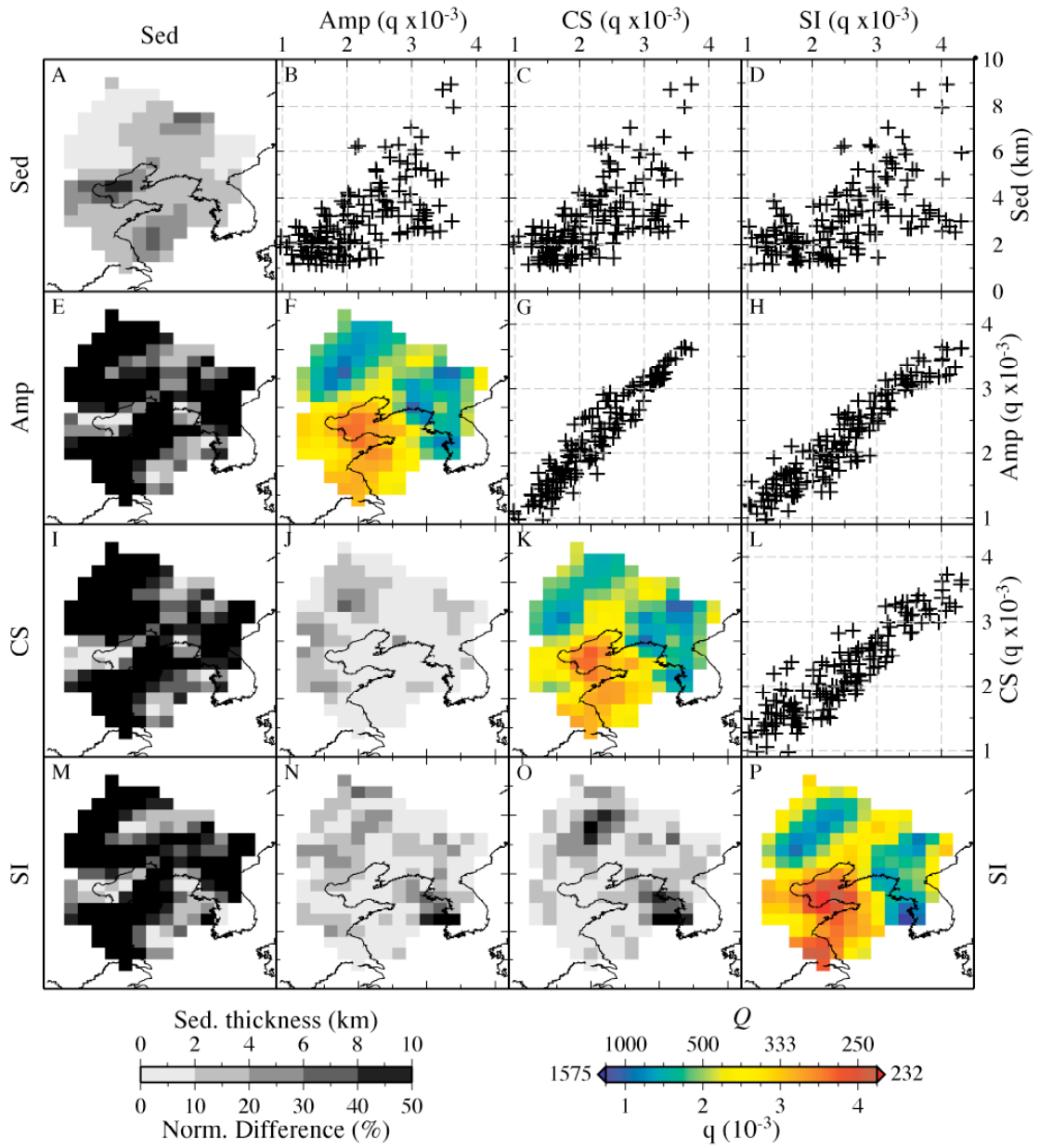


Figure 7.4. Path term comparison of the amplitude tomography method (Amp), and coda-source corrected (CS) and source-interpreted (SI) versions of that method (see text for descriptions of the methods). Plots along the diagonal (panels A, F, K, P) show spatial attenuation for the YSKP region (q color scale in the lower right) for each method, where Sed is the 1° sediment thickness (grayscale in lower left) from Laske and Masters (1997). Comparison at each 1° grid node is shown in the upper triangle (panels B, C, D, G, H, L) where values are given in q (1/*Q*) and Sed (sediment thickness) is in km. Spatial comparison in normalized percent difference is shown in the lower triangle (panels E, I, J, M, N, O).

difference occurs in the region near stations INCN and TJN (highest *NPD* in panels N, O), where the SI method produces the smallest q (panel P). This difference is certainly related to the source and site outliers discussed previously, and demonstrates the trade-off between source, site, and path inherent to the underlying formalism used by all methods. This is especially interesting when comparing the Amp and SI methods (panel N), which only really differ in the regularization schemes employed.

There are three previous lateral attenuation studies where the YSKP region is imaged. Phillips et al. (2005) produced maps of Lg *Q* at 1 Hz in Asia and where there is overlap there is good agreement in spatial variation as well as absolute *q*. Pei et al. (2006) used a local magnitude tomography technique to approximate *Q* near 1 Hz in southern China. The Bohai Bay is one of the most attenuating regions in their study, and this feature along with the low attenuation near Jiaoliao is similar to the results here. *q* near the Da-xin-an-ling and Changbai Mts. is not as low, though these features are at the edges of their model. Finally, Chung et al. (2007) spatially smoothed the results from a reverse two-station analysis of Lg *Q* to produce an image of *Q* at 1 Hz for the YSKP. Their results are anti-correlated with the results of this study, where *q* is lowest in the Songliao Basin (<1.0) and Bohai Bay (<1.3) and highest along the Changbai Mts. (>2.5).

### 7.4 Conclusion

We introduce coda-source corrected amplitude tomography (CS) and compare it with two other similar methods to measure path attenuation. The CS method is a 2-D

implementation of the 1-D method of Walter et al. (2007) and it compares favorably with the amplitude tomography method (AMP) of Phillips and Stead (2008) and a new source-interpreted amplitude tomography method (SI) developed by Pasyanos et al. (2009). The CS method is the Amp method, but where the data are corrected for the source using independent stable coda-source spectra. The SI method is the AMP method (with a slightly different regularization scheme) where a starting source term is provided and the output source term is now straight-forwardly interpreted in terms of a source model.

Due to its reduction of the null space from the elimination of the source parameter in the inversion, the CS method may be more accurate in regions with poor coverage. The source correction potentially improves coverage by adding events measured at only one station. Also, all methods are insensitive to small errors in the starting model. This is especially encouraging in the context of the SI method, where amplitudes from new events can now be better predicted. The greatest difference in the model parameters produced by each of the methods is due to the region between stations INCN and TJN. The source, site, and path terms from this area have a slight variance among the methods. A higher resolution, more regional study is needed to find appropriate parameters for this area. Attenuation in the Yellow Sea / Korean Peninsula is correlated with topography (low attenuation) and sediment thickness (high attenuation). $q$ in the entire YSKP ranges from 0.95 ($Q$ = 1048) to 3.63 ($Q$ = 275).

## Chapter 8

## Bibliography


Aki, K. (1980), Attenuation of shear-waves in the lithosphere for frequencies from 0.05 to 25 Hz, *Phys. Earth Planet. Inter.*, 21, 50-60.

Aki, K. and Y.-B. Tsai (1972), Mechanism of love-wave excitation by explosive sources, *J. Geophys. Res.*, 77(8), 1452-1475.

Aki, K., and P. G. Richards (2002), Quantitative seismology, Sausalito: University Science Books.

Aleqabi, G. I., and M. E. Wysession (2006), Q(Lg) distribution in the basin and range province of the western United States, *Bull. Seis. Soc. Amer.*, 96, 348-354.

Anderson, J. G., Y. Lee, Y. Zeng, and S. Day (1996), Control of strong motion by the upper 30 meters, *Bull. Seis. Soc. Amer.*, 86, 1749-1759.

Aster, R., B. Borchers, and C. H. Thurber (2004), Parameter estimation and inverse problems, Academic Press.

Atkinson, G. M., and R. F. Mereu (1992), The shape of ground motion attenuation curves in Southeastern Canada, *Bull. Seis. Soc. Amer.*, 82, 2014-2031.

Baker, G. E., J. Stevens, and H. M. Xu (2004), Lg group velocity: A depth discriminant revisited, *Bull. Seis. Soc. Amer.*, 94, 722-739.

Bates, D. M., and D. Watts (1988), Nonlinear regression analysis and its applications, New York : Wiley.

Benz, H. M., A. Frankel, and D. M. Boore (1997), Regional Lg attenuation for the continental United States, *Bull. Seis. Soc. Amer.*, 87, 606-619.

Bonner, J., R. B. Herrmann, D. Harkrider, and M. Pasyanos (2008), The Surface Wave Magnitude for the 9 October 2006 North Korean Nuclear Explosion, *Bull. Seis. Soc. Amer.*, 98, 2498-2506.

Boore, D. M., and J. Boatwright (1984), Average body-wave radiation coefficients, *Bull. Seis. Soc. Amer.*, 74, 1615-1621.

Bowers, D and W. R. Walter, (2002), Discriminating between large mine collapses and explosions using teleseismic P waves, *Pure Appl. Geophys.*, 159, 803-830.

Bowers, D. and J.A. Hudson (1999), Defining the scalar moment of a seismic source with a general moment tensor, *Bull. Seis. Soc. Amer.*, 89, 1390-1394.

Bowman, J. R., and B. L. N. Kennett (1991), Propagation of Lg waves in the North Australian Craton; influence of crustal velocity gradients, *Bull. Seis. Soc. Amer.*, 81, 592-610.

Brune, J. N. and P. Pomeroy (1963), Surface wave radiation for underground nuclear explosions and small magnitude earthquakes, *J. Geophys. Res.*, 68, 5005-5028.

Campillo, M. (1990), Propagation and attenuation characteristics of the crustal phase Lg, *Pure Appl. Geophys.* 132, 1-19.

Campillo, M., J. Plantet, and M. Bouchon (1985), Frequency-dependent attenuation in the crust beneath central France from Lg waves; data analysis and numerical modeling, *Bull. Seis. Soc. Amer.* 75, 1395-1411.

Chun, K.-Y., G. F. West, R. J. Kokoski, and C. Samson (1987), A novel technique for measuring Lg attenuation; results from Eastern Canada between 1 to 10 Hz, *Bull. Seis. Soc. Amer.*, 77, 398-419.

Chung, T. W., M. H. Noh, J. K. Kim, Y. K. Park, H. J. Yoo, and J. M. Lees (2007). A study of the regional variation of low-frequency $Q_{Lg}^{-1}$ around the Korean Peninsula, *Bull. Seism. Soc. Amer.* 97: 2190–2197.

Chung, T. W., Y. K. Park, I. B. Kang, and K. Lee (2005), Crustal QLg-1 in South Korea using the source pair/receiver pair method, *Bull. Seis. Soc. Amer.*, 95, 512-520.

Chung, T., and K. Lee (2003), A study of high-frequency $Q_{Lg}^{-1}$ in the crust of South Korea, *Bull. Seis. Soc. Amer.*, 93, 1401-1406.

Day, S. M. and K. L. McLauglin (1991), Seismic source representations for spall, *Bull. Seism. Soc. Amer.*, 81, 191-201.

Dreger, D. and B. Woods (2002), Regional distance seismic moment tensors of nuclear explosions; seismic source mechanism through moment tensors, *Tectonophysics*, 356, 139-156.

Dreger, D. S. and D. V. Helmberger (1990), Broadband modeling of local earthquakes, *Bull. Seism. Soc. Amer.*, 80, 1162-1179.

Dufumier, H. and L. Rivera (1997), On the resolution of the isotropic component in moment tensor inversion, *Geophys. J. Int.*, 131, 595-606.

Ekstrom, G. and P.G. Richards (1994), Empirical measurements of tectonic moment release in nuclear-explosions from teleseismic surface-waves and body waves, *Geophys. J. Int.*, 117, 120-140.

Erickson, D., D. E. McNamara, and H. M. Benz (2004), Frequency-dependent Lg Q within the continental United States, *Bull. Seis. Soc. Amer.*, 94, 1630-1643.

Fan, G. W., and T. Lay (2003a), Strong Lg attenuation in the Tibetan Plateau, *Bull. Seis. Soc. Amer.*, 93, 2264-2272.

Fan, G., and T. Lay (2003b), Strong Lg wave attenuation in the northern and eastern Tibetan Plateau measured by a two-station/two-event stacking method, *Geophys. Res. Lett.*, 30, 4.

Faraway, J. J. (2004), Linear Models with R, Chapman & Hall/CRC.

Fletcher, J.B. and A. McGarr (2005), Moment Tensor Inversion of Ground Motion from Mining-Induced Earthquakes, Trail Mountain, Utah, *Bull. Seis. Soc. Amer.*, 95, 48-57.

Ford, S. R., D. S. Dreger, K. Mayeda, W. R. Walter, L. Malagnini, and W. S. Phillips (2008), Regional attenuation in Northern California: A comparison of five 1D *Q* methods, *Bull. Seis. Soc. Amer.*, 98, 2033-2046.

Ford, S.R., Douglas S. Dreger, and William R. Walter (2007) Identifying isotropic events using an improved regional moment tensor inversion technique, *29th Monitoring Research Review*, Denver, USA.

Foulger, G. R., B. R. Julian, D. P. Hill, A. M. Pitt, P. E. Malin, and E. Shalev (2004), Non-double-couple microearthquakes at Long Valley caldera, California, provide evidence for hydraulic fracturing, *J. Volcanol. Geotherm. Res.*, 132, 45-71.

Frankel, A. (1990). Attenuation of high-frequency shear waves in the crust: Measurements from New York State, South Africa, and Southern California, *J. Geophys. Res.* 95: 17441–17457.

Frankel, A. A. McGarr, J. Bicknell, J. Mori, L. Seeber, and E. Cranswick (1990), Attenuation of high-frequency shear waves in the crust: measurements from New York State, South Africa, and Southern California, *J. Geophys. Res.*, 95, 17441-17457.

Gilbert, F. (1971), Excitation of the normal modes of the earth by earthquake sources, *Geophys. J. R. Soc.*, 22, 223-226.

Given, J. W. and G.R. Mellman (1986), Estimating explosion and tectonic release source parameters of underground nuclear explosions from Rayleigh and Love wave observations, Tech. rep., Sierra Geophysics Report No. SGI-R-86-126, Kirkland, WA.

Goldstein, P., D. Dodge, and M. Firpo (1999), SAC2000: Signal processing and analysis tools for seismologists and engineers, in International Handbook of Earthquake and Engineering Seismology, edited by W. Lee et al., pp. 1613-1614, New York: Elsevier.

Graves, R. W., and S. M. Day (2003), Stability and accuracy analysis of coarse-grain viscoelastic simulations, *Bull. Seis. Soc. Amer.* 93, 283-300.

Hanks, T. C., and A. C. Johnston (1992), Common features of the excitation and propagation of strong ground motion for North American earthquakes, *Bull. Seis. Soc. Amer.* 82,, 1-23.

Hellweg, M., R. A. Uhrhammer, K. Hutton, A. Walter, P. Lombard and E. Hauksson (2007), Recalibrating ML for CISN, Eos Trans. AGU, 88 (52), Fall Meet. Suppl., Abstract S41B-0565.

Herrmann, R. B. and K. Hutchensen (1993), Quantification of $M_{Lg}$ for small explosion, Tech. rep., Phillips Laboratory Report PL-TR-93-2070.

Hong, T.-K. and J. Rhie (2008), Investigation of regional source properties of the underground nuclear explosion in North Korea, *30th Monitoring Research Review*, Portsmouth, USA.

Hudson, J. A., R. G. Pearce, R. G., and R. M. Rogers (1989), Source type plot for inversion of the moment tensor, *J. Geophys. Res.*, 9, 765-774.

Ichinose, G. A., J. G. Anderson, K. D. Smith and Y. Zeng (2003), Source parameters of Eastern California and Western Nevada earthquakes from regional moment tensor inversion, *Bull. Seis. Soc. Amer.*, 93, 61-84.

Jechumtalova, Z. and J. Sileny (2001), Point-source parameters from noisy waveforms: Error estimate by Monte-Carlo simulation, *Pure Appl. Geophys.*, 158, 1639-1654.

Jechumtalova, Z. and J. Sileny (2005), Amplitude ratios for complete moment tensor retrieval, *Geophys. Res. Lett.*, 32, 4.

Julian, B. R., A. D. Miller and G. R. Foulger (1998), Non-double-couple earthquakes; 1. Theory, *Rev. Geophys.*, 36, 525- 549.

Kanamori, H., P. Maechling, and E. Hauksson (1999), Continous monitoring of ground-motion parameters, *Bull. Seis. Soc. Amer.*, 89, 311-316.

Kawakatsu, H. (1991), Insignificant isotropic component in the moment tensor of deep earthquakes, *Nature*, 351, 50-53.

Knopoff, L. and M. J. Randall (1970), The compensated linear-vector dipole; a possible mechanism for deep earthquakes, *J. Geophys. Res.*, 75(26), 4957-4963.

Kuge, K. and T. Lay (1994), Systematic non-double-couple components of earthquake mechanisms; the role of fault zone irregularity, *J. Geophys. Res.*, 99, 15,457-15,467.

Langston, C. A. (1981), Source inversion of seismic waveforms; the Koyna, India, earthquakes of 13 September 1967, *Bull. Seis. Soc. Amer.*, 71, 1-24.

Laske, G., and G. Masters, A Global Digital Map of Sediment Thickness (1997), EOS Trans. AGU, 78, F483.

Malagnini, L., K. Mayeda, R. Uhrhammer, A. Akinci, and R. B. Herrmann (2007), A regional ground-motion excitation/attenuation model for the San Francisco region, *Bull. Seis. Soc. Amer.*, 97, 843-862.

Mayeda, K., A. Hofstetter, J. L. O'Boyle, and W. R. Walter (2003). Stable and transportable regional magnitudes based on coda-derived moment-rate spectra, *Bull. Seis. Soc. Amer.* 93: 224–239.

Mayeda, K., A. Hofstetter, J. L. O'Boyle, and W. R. Walter (2003), Stable and transportable regional magnitudes based on coda-derived moment-rate spectra, *Bull. Seis. Soc. Amer.*, 93, 224-239.

Mayeda, K., L. Malagnini, W. S. Phillips, W. R. Walter, and D. Dreger (2005), 2-D or not 2-D, that is the question: A northern California test, *Geophys. Res. Lett.*, 32, L12301.

McNamara, D. E., T. J. Owens, and W. R. Walter (1996), Propagation characteristics of Lg across the Tibetan Plateau, *Bull. Seis. Soc. Amer.*, 86, 457-469.

Menke, W., R. C. Holmes, and J. Xie (2006). On the nonuniqueness of the coupled origin time - velocity tomography problem, *Bull. Seis. Soc. Amer.* **96** (3): 1131-1139, doi:10.1785/0120050192.

Minson, S. and D. Dreger (2007), Improved seismic moment tensor inversion, *Geophys. J. Int.*, 32, 254.

Moore, D. S., and G. P. McCabe (2002), Introduction to the Practice of Statistics, W. H. Freeman.

Muller, G. (1973), Seismic moment and long-period radiation of underground nuclear explosions, *Bull. Seis. Soc. Amer.*, 63, 847-857.

Nuttli, O. W. (1973), Seismic Wave Attenuation and Magnitude Relations for Eastern North America, *J. Geophys. Res.*, 78, 876-885.

Olson, A. H., and J. G. Anderson (1988), Implications of frequency-domain inversion of earthquake ground motions for resolving the space-time dependence of slip on an extended fault, *Geophys. J. R. Soc.*, 94, 443-455.

Paige, C. C., and M. A. Saunders (1982), Algorithm 583, LSQR: Sparse linear equations and least-squares problems, *Trans. Math Software*, 8, 195-209.

Panning, M., D. Dreger and H. Tkalcic (2001), Near-source velocity structure and isotropic moment tensors; a case study of the Long Valley Caldera, *Geophys. Res. Lett.*, 28, 1815-1818.

Pasyanos, M. E., E. M. Matzel, W. R. Walter, and A. J. Rodgers (2008). Broadband Lg attenuation modeling in the Middle East, Geophys. J. Int., submitted

Pasyanos, M. E., G. A. Franz and A. L. Ramirez (2006), Reconciling a geophysical model to data using a Markov Chain Monte Carlo algorithm: An application to the Yellow Sea-Korean Peninsula region, *J. Geophys. Res.*, 111, B03313.

Patton, H. J. (1988), Source models of the Harzer explosion from regional observations of fundamental-mode and higher mode surface waves, *Bull. Seis. Soc. Amer.*, 78, 1133-1157.

Patton, H. J. (1991), Seismic moment estimation and the scaling of the long-period explosion source spectrum, in Explosion Source Phenomenology, *AGU Monograph*, 65, edited by Taylor, Patton and Richards.

Pechmann, J. C., W. R. Walter, S. J. Nava, and W. J. Arabasz (1995), The February 3, 1995 ML 5.1 seismic event in the trona mining district of southwestern Wyoming, *Seism. Res. Lett.*, 66, 25-34.

Pei, S., J. Zhao, C. A. Rowe, S. Wang, T. M. Hearn, Z. Xu, H. Liu, and Y. Sun (2006). $M_L$ amplitude tomography in North China, *Bull. Seism. Soc. Amer.* 96: 1560–1566.

Phillips, W. S. and R. J. Stead (2008), Attenuation of Lg in the western US using the USArray, *Geophys. Res. Lett.*, 35, L07307.

Phillips, W. S., H. E. Hartse, and J. T. Rutledge (2005). Amplitude ratio tomography for regional phase *Q*, *Geophys. Res. Lett.* 32: L21301.

Phillips, W. S., W. H. K. Lee, and J. T. Newberry (1988) Spatial variation of crustal coda Q in California, *Pure Appl. Geophys.*, 128, 251-261.

Press, F. and C. Archambeau (1962), Release of tectonic strain by underground nuclear explosions, *J. Geophys. Res.*, 67, 337-343.

R Development Core Team. (2006), R: A Language and Environment for Statistical Computing, R Foundation for Statistical Computing, Vienna, Austria.

Riedesel, M. and T. H. Jordan (1989), Display and assessment of seismic moment tensors, *Bull. Seism. Soc. Amer.*, 79, 85-100.

Roessler, D., F. Krueger, and G. Ruempker (2007), Retrieval of moment tensors due to dislocation point sources in anisotropic media using standard techniques, *Geophys. J. Int.*, 169, 136-148.

Saikia, C. K. (1994), Modified frequency-wavenumber algorithm for regional seismograms using Filon's quadrature; modelling of Lg waves in Eastern North America, *Geophys. J. Int.*, 118, 142-158.

Shih, X. R., K. Y. Chun, and T. Zhu (1994), Attenuation of 1-6 s Lg waves in Eurasia, *J. Geophys. Res.*, 99, 23869-23875.

Sileny, J. (1998), Earthquake source parameters and their confidence regions by a genetic algorithm with a 'memory', *Geophys. J. Int.*, 134, 228-242.

Sileny, J. (2004), Regional moment tensor uncertainty due to mismodeling of the crust, *Tectonophysics*, 383, 133-147.

Sileny, J. and V. Vavrycuk (2002), Can unbiased source be retrieved from anisotropic waveforms by using an isotropic model of the medium?; Seismic source mechanism through moment tensors, *Tectonophysics*, 356, 125-138.

Sileny, J., G. F. Panza, and P. Campus (1992), Waveform inversion for point source moment tensor retrieval with variable hypocentral depth and structural model, *Geophys. J. Int.*, 109, 259-274.

Sileny, J., P. Campus, and G. F. Panza (1996), Seismic moment tensor resolution by waveform inversion of a few local noisy records; I, Synthetic tests, *Geophys. J. Int.*, 126, 605-619.

Song, X. J., D. V. Helmberger and L. Zhao (1996), Broad-band modelling of regional seismograms; the basin and range crustal structure, *Geophys. J. Int.*, 125, 15-29.

Springer, D. L., G. A. Pawloski, J. L. Ricca, R. F. Rohrer and D. K. Smith (2002), Seismic source summary for all U.S. below-surface nuclear explosions, *Bull. Seis. Soc. Amer.*, 92, 1806-1840.

Street, R. L., R. B. Herrmann, and O. W. Nuttli (1975), Spectral characteristics of the Lg wave generated by central United States earthquakes, *Geophys. J. R. Soc.*, 41, 51-63.

Taylor, S. R., (1994), False alarms and mine seismicity: an example from the Gentry mountain mining region, Utah, *Bull. Seism. Soc. Amer.*, 84, 350-358.

Taylor, S. R., A. A. Velasco, H. E. Hartse, W. S. Phillips, W. R. Walter, and A. J. Rodgers (2002), Amplitude corrections for regional seismic discriminants; Monitoring the Comprehensive Nuclear-Test-Ban Treaty; seismic event discrimination and identification, *Pure Appl. Geophys.*, 159, 623-650.

Taylor, S. R., J. T. Rambo, and R. P. Swift (1991), Near-source effects on regional seismograms: An analysis of the NTS explosions PERA and QUESO, *Bull. Seis. Soc. Amer.*, 81 (6), 2371-2394.

Templeton, D. C. and D. S. Dreger (2006), Non-double-couple earthquakes in the Long Valley volcanic region, *Bull. Seism. Soc. Amer.*, 96, 69-79.

Toksoz, M. N. and H. H. Kehrer (1972), Tectonic strain release by underground nuclear explosions and its effect on seismic discrimination, *Geophys. J. R. Soc.*, 31, 141-161.

Uhrhammer, R. A., and E. R. Collins (1990), Synthesis of Wood-Anderson seismograms from broadband digital records, *Bull. Seis. Soc. Amer.*, 80, 702 - 716.

Uhrhammer, R. A., S. J. Loper, and B. Romanowicz (1996), Determination of local magnitude using BDSN broadband records, *Bull. Seis. Soc. Amer.*, 86, 1314-30.

Vasco, D. W. (1990), Moment-tensor invariants: searching for non-double-couple earthquakes, *Bull. Seis. Soc. Amer.*, 80, 354-371.

Venables, W. N., and B. D. Ripley (2002), Modern Applied Statistics with S, Springer, New York.

Wald, D. J. and T. I. Allen (2008). Topographic slope as a proxy for seismic site conditions and amplification, *Bull. Seism. Soc. Am.*, in press, http://earthquake.usgs.gov/research/hazmaps/interactive/vs30/

Walter, W. R. (1993), Source parameters of the June 29, 1992 Little Skull Mountain earthquake from complete regional waveforms at a single station, *Geophys. Res. Lett.*, 20, 403-406.

Walter, W. R. and H. J. Patton (1990), Tectonic release from the soviet joint verification experiment, *Geophys. Res. Lett.*, 17, 1517-1520.

Walter, W. R. and S. R. Taylor (2001). A revised magnitude and distance amplitude correction (MDAC2) procedure for regional seismic discriminants, Lawrence Livermore National Laboratory report UCRL-ID-146882.

Walter, W. R., and A. J. Rodgers (1999), Regional waveform modeling in Southwestern Asia; tectonic release from the May 11, 1998 Indian nuclear tests; SSA-99 94th annual meeting; Meeting abstracts, *Seis. Res. Lett.*, 70, 228.

Walter, W. R., K. D. Smith, J. L. O'Boyle, T. F. Hauk, F. Ryall, S. D. Ruppert, S. C. Myers, R. Abbot and D. A. Dodge (2004), An assembled western United States Dataset for regional seismic analysis, LLNL, UCRL-TR-206630.

Walter, W. R., K. Mayeda, L. Malagnini, and L. Scognamiglio (2007), Regional body-wave attenuation using a coda source normalization method: Application to MEDNET records of earthquakes in Italy, *Geophys. Res. Lett.*, 34, L10308.

Weber, Z. (2006), Probabilistic local waveform inversion for moment tensor and hypocentral location, *Geophys. J. Int.*, 165, 607-621.

Wessel, P., and W. H. F. Smith (1998), New, improved version of generic mapping tools released, in American Geophysical Union, San Francisco, Vol. 79, 579.

Woods, B. B., S. Kedar, and D. V. Helmberger (1993), $M_L$:$M_0$ as a regional seismic discriminant, *Bull. Seism. Soc. Amer.*, 83, 1167-1183.

Xie, J. (1998), Spectral inversion of Lg from earthquakes; a modified method with applications to the 1995, western Texas earthquake sequence, *Bull. Seis. Soc. Amer.* 88, 1525-1537.

Xie, J. (2002), Lg Q in the eastern Tibetan Plateau, *Bull. Seis. Soc. Amer.*, 92, 871-876.

Xie, J., and B. J. Mitchell (1990), Attenuation of multiphase surface waves in the Basin and Range Province: Part I, Lg and Lg coda, *Geophys.J. Int.*, 102, 121-137.

Xie, J., R. Gok, J. Ni, and Y. Aoki (2004), Lateral variations of crustal seismic attenuation along the INDEPTH profiles in Tibet from Lg Q inversion, *J. Geophys. Res.*, 109, B10308.

Yang, X. N. (2002), A numerical investigation of Lg geometrical spreading, *Bull. Seis. Soc. Amer.* 92, 3067-3079.

Yoshimoto, K., H. Sato, and M. Ohtake (1993), Frequency-dependent attenuation of P and S waves in the Kanto area, Japan, based on the coda-normalization method, *Geophys. J. Int.*, 114, 165-174.